BACKSCATTERING OF 5-15 keV

LIGHT IONS FROM SILICON

By

SAID A. AGAMY, M.Eng.

A Thesis

Submitted to the School of Graduate Studies

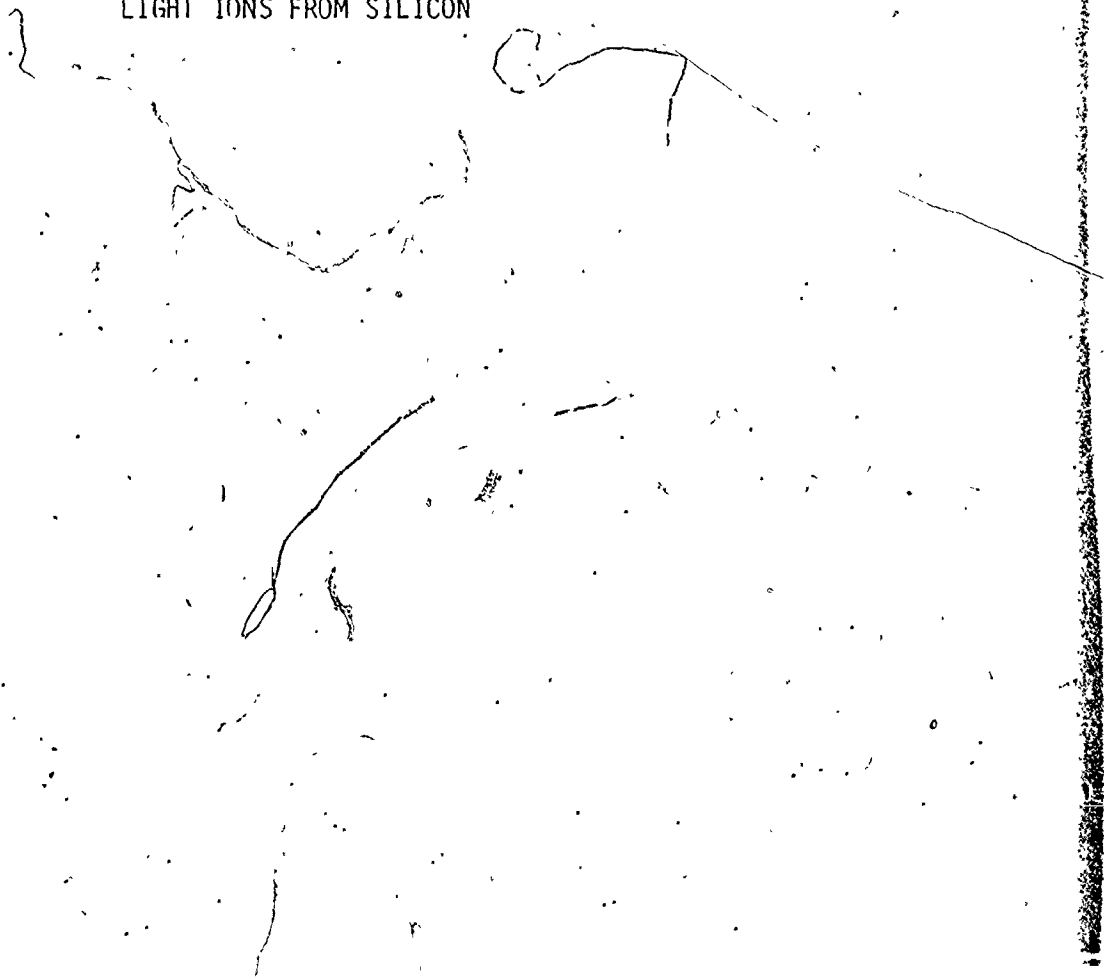in Partial Fulfilment of the Requirements

for the Degree

Doctor of Philosophy

McMaster University

April 1978

BACKSCATTERING OF 5-15 keV

LIGHT IONS FROM SILICON

DOCTOR OF PHILOSOPHY (1978)   McMASTER UNIVERSITY
(Materials Science)   Hamilton, Ontario

TITLE: Backscattering of 5-15 keV Light Ions from Silicon

AUTHOR: Said A. Agamy, M.Eng. (McMaster University)

SUPERVISOR: Dr. J.E. Robinson

NUMBER OF PAGES: xi, 128

ABSTRACT

In this thesis the scattering of hydrogen and helium ions, in the incident particle energy range 5-15 keV, from silicon targets is studied both theoretically and experimentally. In the theoretical treatment, electronic and nuclear energy losses are included in a computer simulation model. The computer simulation technique has been developed to study the interaction of the incident ions and target atoms for an incident reduced energy range $0.05 < \varepsilon_0 < 20$ of interest in fusion research. The theoretical model is based on a Thomas-Fermi interatomic potential and experimetnal values for the electronic energy loss coefficient. The backscattered energy and angular distributions are calculated by following the histories of 5,000 to 10,000 particles. An experimental system using the time-of-flight technique has been developed to measure the energy spectra of light ions and neutrals backscattered from solid surfaces thus permitting a comparison of the theory with experimental data for a well characterised target. To test the time-of-flight technique, ions and neutrals were scattered from thin silver films (20-40 Å) evaporated on silicon substrates. From the measurements it was found that the sensitivity of the technique is better than 1/20 of a monolayer for silver on silicon. The energy resolution for helium scattered from these targets was found to be 10-15% which is consistent with the time-of-flight resolution and the electronic-loss energy broadening. To measure the energy spectra of the backscattered particles,

time-of-flight spectra for hydrogen and helium scattered from silicon were recorded. These spectra were then transformed to energy spectra. The comparison between the experimental and theoretical results showed good agreement down to a backscattered energy of 500 eV (cut-off energy due to detector calibration limits). A number of experiments were done to measure the charge fractions of the backscattered H and He particles from a silicon target. For hydrogen scattering no surface peaks were observed and also there was no penetration effect on the charge fractions. This is an indication that hydrogen neutralization occurs at the surface. On the other hand, in the helium case peaks were observed in the charge fractions corresponding to surface scattering. This indicates that helium bound states occur inside the target. Finally, the effect of surface cleaning was studied. The results showed that a factor of 2 increase in ion yield was observed after cleaning the surface by 5 keV neon bombardment. The reduction in the charge fraction for the practical surface was mainly due to carbon and oxygen impurities on the surface.

ACKNOWLEDGEMENTS

TABLE OF CONTENTS

LIST OF ILLUSTRATIONS

CHAPTER 1

INTRODUCTION

An energetic ion incident on a solid target will undergo
collisions with atomic nuclei and the electrons of the solid.
This incident ion can lose energy through collisions until it comes
to rest inside the target or experiences multiple deflections leading
to backscattering from the surface. In the study of low and medium
energy (5-15 keV) ion scattering from solids, two major problems are
encountered; first, the interatomic potential between the colliding
particles is not precisely known, and second is the neutralization of
the backscattered particles which creates difficulties in measuring
the actual scattered particles.

The objective of this study is to determine the energy distri-
bution and charge states of light ions (H^+, He^+) backscattered from
silicon for incident ion energies below 20 keV. Silicon was chosen
because it is a well characterized material and many scattering
studies in the other energy ranges were performed on silicon targets.

Knowledge of the energy, angular and charge distributions of
light atoms backscattered from solid surfaces is of importance for
the evaluation of the interaction of a hot plasma with the surrounding
walls (1,2). The energy range up to 20 keV is of special interest since
this corresponds to the temperature in a D-T fusion reactor. Also, low
energy ion scattering is a very successful technique for surface

1

analysis. Using this technique, it is possible to analyze the outermost atomic layers of the surface. Analogous to Rutherford backscattering, the energy loss of an ion scattered at low energies depends on the mass of the target atom. Therefore, energy spectra of the backscattered particles can be used to analyze solid surfaces.

At high and medium energies ($\gtrsim 100$ keV) the interatomic potential is that of two unscreened nuclear charges, i.e. Coulomb potential. Therefore, the Rutherford formula for the scattering cross section is used. In this energy range the scattering cross section is small, because of the $1/E^2$ dependence, and therefore only single collision events are encountered. Solid state detectors are used to detect the backscattered particles; therefore both charged and neutral particles are recorded. This is why Rutherford backscattering technique gives quantitative results (3).

At low energies the nuclear charges are screened by the electronic clouds and screening functions are used to modify the Coulomb potential. Smith (4) used low energy ion scattering to analyze adsorbed gases on nickel surface. Since only charged particles were detected using an electrostatic energy analyzer (ESA), the technique will give only qualitative results. Most of the backscattered particles are neutrals and consequently will not be detected.

To overcome this neutralization problem, a time-of-flight technique was first applied to low and medium energy ion scattering by Buck et. al. (5). This helps in correcting the ESA spectra, i.e. in calibrating the ESA, and also provides a technique for charge fraction

measurements.

One of the major requirements of low energy ion scattering is the necessity of using an UHV target chamber (10^{-9} Torr) since the technique is very sensitive to surface conditions. The time-of-flight technique is compatible with the UHV system. This is an advantage over the stripping technique, originally proposed by Chicherov (6), which uses high pressure gas (10^{-3} Torr) to reionize the neutral particles. This latter technique requires complicated differential pumping of the detector.

In chapter 2, the collision phenomena are discussed. The different mechanisms of energy loss and different theories for ion-solid interactions, namely, LSS and WSS theories, are reviewed.

In this thesis, a computer simulation model was developed to study the backscattered energy and angular distributions. The model assumes a random or amorphous target and Thomas-Fermi interatomic potential. The cross sections used are those developed originally by Lindhard et. al. (7). The details of the model and results obtained are given in Chapter 3.

The major part of the experimental work was the design and construction of low energy light ion scattering facility. The apparatus developed is described in Chapter 4. Also in this chapter, the time-of-flight technique (TOF) is described and the TOF resolution is also discussed. At the end of this chapter the advantages and disadvantages of the technique are listed.

To test the TOF technique, a controlled surface analysis experiment was undertaken. It is described in Chapter 5. Silver films (20-40 Å thick) were deposited on silicon substrates; the targets were characterized using the Rutherford backscattering technique. TOF and energy spectra for hydrogen and helium backscattered from these targets are presented in this chapter. The sensitivity and resolution of the technique are discussed. Also in this chapter, a general summary of the use of ion scattering for surface analysis (techniques and limitations) is given.

The TOF technique was then used to measure the energy spectra of hydrogen and helium backscattered from silicon. TOF spectra for 5-15 KeV hydrogen and helium were recorded and then transformed to energy spectra. These spectra, together with the limitation of the technique are presented in Chapter 6.

In Chapter 7, the charged fractions measurements are presented. Also the effect of surface cleanliness is discussed with experimental results. Finally, in Chapter 8, a general summary of the thesis is given.

CHAPTER 2

A REVIEW OF SCATTERING THEORY

2.1 Introduction

An energetic ion impinging on a solid interacts with the atoms and electrons. The relative magnitude of these interactions depends on the incident energy. At high energies, the ion interacts predominantly with the electrons of the solid. These electronic interactions will not cause any deflections in the ion's trajectory because of the small momentum transferred in the process, but will cause an overall energy loss. Atomic scattering, on the other hand, is more important in the low energy range. Because of the larger momentum transfer in these collisions, the ion will experience angular deflections as well as discrete energy losses determined by the conservation of energy and momentum.

Generally, an ion will undergo both nuclear (elastic) and electronic (inelastic) collisions inside the solid (8). This ion will either come to rest inside the target material or scatter back with a certain fraction of the incident energy. The collision cross sections are governed by the interatomic potentials between the interacting species. The choice of the interatomic potential is of prime importance in determining the trajectory of the incident particle. In this chapter a general review of the scattering theory is presented.

2.2 Energy Loss Mechanisms

Nuclear energy loss, or nuclear stopping, $\left(\frac{dE}{dx}\right)_n$, is due to elastic interactions between the incident projectile and the screened nuclear charges of the target nuclei. For an incident projectile energy E_0 and a scattering angle θ in the center of mass coordinates, the energy transferred to a target atom in a nuclear collision is given by (9):

$$T = \frac{4M_1 M_2}{(M_1 + M_2)^2} E_0 \sin^2 \left(\frac{\theta}{2}\right) \tag{2.1a}$$

$$= \gamma E_0 \sin^2 \left(\frac{\theta}{2}\right) \tag{2.1b}$$

where M_1 and M_2 are the projectile and the target atom masses respectively.

The maximum energy transferred for a head-on collision ($\theta = 180°$) is:

$$T_m = \gamma E_0 \tag{2.2}$$

Therefore,

$$T = T_m \sin^2 \left(\frac{\theta}{2}\right) \tag{2.3}$$

The nuclear stopping loss can be expressed as

$$\left(\frac{dE}{dx}\right)_n = -N \, S_n(E) \tag{2.4}$$

where N is the atomic density of the target material and $S_n(E)$ is the stopping cross section for energy loss in a nuclear collision. $S_n(E)$ is given by

$$S_n(E) = \int_0^{\gamma E_0} T d\sigma \qquad (2.5)$$

where $d\sigma$ is the differential scattering cross section for energy transfer. An expression for $d\sigma$ will be shown in section 2.4.

The scattering angle in the center of mass coordinates depends on the interatomic potential between the incoming projectile and the stationary atom. The expression for the scattering angle θ is (10):

$$\theta = \pi - 2p \int_0^{u_0} \frac{du}{[1 - \frac{V(u)}{E_{rel.}} - p^2 u^2]^{1/2}} \qquad (2.6)$$

where p is the impact parameter, $u \equiv \frac{1}{r}$, and $E_{rel.}$ is the primary energy measured with respect to the center of mass, i.e.

$$E_{rel.} = \frac{A}{1 + A} E_0, \qquad A = M_2/M_1 \qquad (2.7)$$

u_0 is the value of u for which the denominator of the integrand in equation (2.7) vanishes.

The scattering angle in the laboratory coordinates, ψ, is given by (9):

$$\cos \psi = \frac{A \cos \theta + 1}{(A^2 + 2A\cos\theta + 1)^{1/2}} \qquad (2.8)$$

The energy of the projectile of initial energy E_0 after scatter-

ing through an angle ψ in the laboratory coordinates is also given by (11):

$$E_2 = E_0 \cdot \frac{M_1^2}{(M_1+M_2)^2} \{\cos \psi + [\left(\frac{M_2}{M_1}\right)^2 - \sin^2 \psi]^{1/2}\}^2 \qquad (2.9)$$

Electronic energy loss, or electronic stopping, $\left(\frac{dE}{dx}\right)_e$, is due to inelastic interations between the projectile and target electrons. This electronic excitation becomes increasingly important at higher projectile energies. The rate of energy loss to electrons has been calculated by Lindhard and Scharff (12):

$$\left(\frac{dE}{dx}\right)_e = -KE^{1/2} \qquad (2.10)$$

where K is a constant given by (13):

$$K = Z_1^{1/6} \frac{Z_1 Z_2}{(Z_1^{2/3}+Z_2^{2/3})^{3/2}} 8\pi Ne^2 a_0 \left(\frac{1}{E'}\right)^{1/2} \qquad (2.11)$$

where a_0 is the Bohr radius and E' is the energy at which the ion velocity equals the velocity of an electron in the first Bohr orbit. This equals 25 keV for hydrogen.

The total energy loss per unit path length of a moving projectile can be approximated by adding the two parts of energy loss, namely:

$$\frac{dE}{dx} = \left(\frac{dE}{dx}\right)_n + \left(\frac{dE}{dx}\right)_e \qquad (2.12a)$$

$$= -N[S_n(E) + S_e(E)] \qquad (2.12b)$$

where $S_e(E)$ is the stopping cross section for energy loss in electronic

collisions.

2.3 Interatomic Potentials

As two atoms come together from an infinite separation, they
will experience an increasing attractive force. As the approach
distance becomes smaller, the force becomes increasingly repulsive.
The minimum of the total potential energy versus distance occurs at
the equilibrium lattice spacing, d, as shown in figure 2.1.
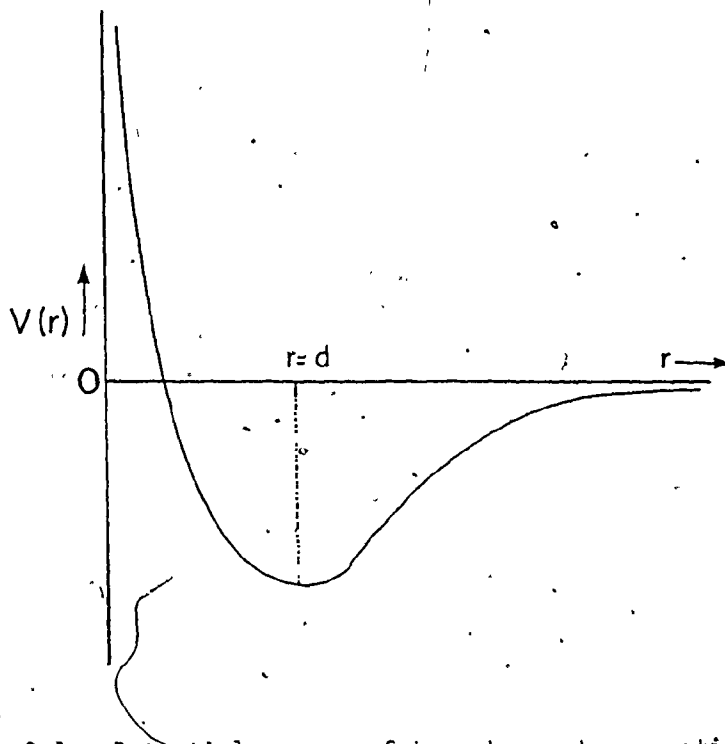
Fig. 2.1: Potential energy of two atoms at separation r.

The main obstacle to the studying of the interaction of incident
projectile and the target atoms is the interatomic potential. Once
the appropriate interatomic potential is chosen, the scattering angle in

the center of mass coordinates can be determined, using equation (2.6),
and consequently all the interaction parameters are determined.

At high energies when the projectile can come close to the
target nucleus, the potential is simply that of two unscreened nuclear
charges at a distance r. This is the Coulomb potential and it takes
the form,

$$V(r) = \frac{Z_1 Z_2 e^2}{4\pi\epsilon_0 r} = (14.4) \frac{Z_1 Z_2}{r} \text{ ev} \qquad (2.13)$$

As the interatomic distance increases, the full potential due
to the nucleus is expected to be reduced by the screening effect of
the orbital electrons. Different analytical forms of this screening
effect have been evaluated by several authors and are obtained by
integration over the contribution due to each individual electron. In
general form, however, the potential may be expressed as,

$$V(r) = \frac{Z_1 Z_2 e^2}{4\pi\epsilon_0 r} f(r/a) \qquad (2.14)$$

where $f(r/a)$ is the screening function and a is a screening length,
for example, as Bohr (8) has suggested for an isolated atom,
may be expressed by $a = a_0 Z_1^{-1/3}$, where a_0 is the first Bohr orbit
(0.529 Å) for the electron in the hydrogen atom and $Z_1 e$ is the nuclear
charge.

Thus the exact specification of the potential depends critically
upon the form chosen for the screening function.

Bohr (8) has also shown that an expression for the screening function is

$$f(r/a) = \exp(-r/a) \tag{2.15a}$$

and therefore, the Bohr potential takes the form,

$$V(r) = \frac{Z_1 Z_2 e^2}{4\pi\varepsilon_0 r} \exp(-r/a)$$

$$= \frac{Z_1 Z_2}{r} (14.4) \exp(-r/a) \tag{2.15b}$$

Other potentials have been proposed. These include

$$V(r) = \frac{Z_1 Z_2}{r} (14.4) \cdot [\frac{r}{a_1} \exp(-cr/a_1)] \tag{2.16}$$

which is the Born-Mayer (14) potential,

and the Thomas-Fermi potential, given by:

$$V(r) = \frac{Z_1 Z_2}{r} (14.4) \, \phi_{TF} (r/a_F) \tag{2.17a}$$

$\phi_{TF} (r/a_F)$ is the Thomas-Fermi screening function and it is tabulated for different values of (r/a_F) (15). a_F is the Thomas-Fermi screening length derived by Firsov (16) as:

$$a_F = 0.8853 \, a_0 \, (Z_1^{1/2} + Z_2^{1/2})^{-2/3} \tag{2.17b}$$

The Thomas-Fermi potential is valid between $r = o$ to $r \simeq 1 \overset{o}{A}$ and is universal for all atoms; this makes it the most useful of all interatomic potentials.

A comparison of the various interatomic potentials is shown in Figure 2.2 (9).
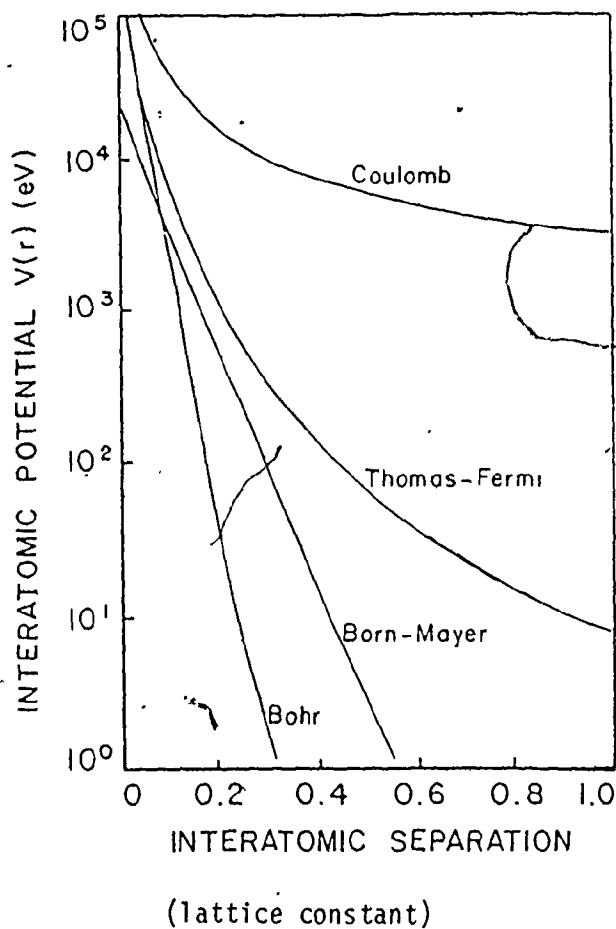
Fig. 2.2: Interatomic potentials for copper.

2.4 LSS Theory

The problem of ion scattering by screened Coulomb fields was studied comprehensively by Lindhard, Scharff, and Schiott (17) and Schiott (18). The treatment was based on a universal nuclear stopping cross section, S_n, calculated from a Thomas-Fermi model for the inter-

action between ions, and an electronic stopping cross section, S_e, proportional to the velocity of the incoming particle.

When the energy and range are measured in the dimensionless parameters ε and ρ, where

$$\varepsilon = E \frac{a\,M_2}{Z_1 Z_2 e^2 (M_1 + M_2)}, \tag{2.18}$$

$$\rho = RNM_2\,4\pi a^2\,\frac{M_1}{(M_1 + M_2)^2}. \tag{2.19}$$

where a is the screening parameter in the Thomas-Fermi potential and is given by

$$a = a_0\,0.8853\,(Z_1^{2/3} + Z_2^{2/3})^{-1/2}$$

the nuclear stopping power, i.e. $(d\varepsilon/d\rho)_n$ is a function of ε only, independent of the incoming particle and the stopping substance, Figure 2.3. In the same units the electronic stopping power is represented by,

$$\left(\frac{d\varepsilon}{d\rho}\right)_e = -k\varepsilon^{1/2} \tag{2.20}$$

where

$$k = \xi_e \frac{0.0793 . Z_1^{1/2} Z_2^{1/2} . (A_1 + A_2)^{3/2}}{(Z_1^{2/3} + Z_2^{2/3})^{3/4}\,A_1^{3/2}\,A_2^{1/2}} \tag{2.21}$$

and ξ_e is given the value $Z_1^{1/6}$. Therefore, the total stopping power, in reduced units, is given by
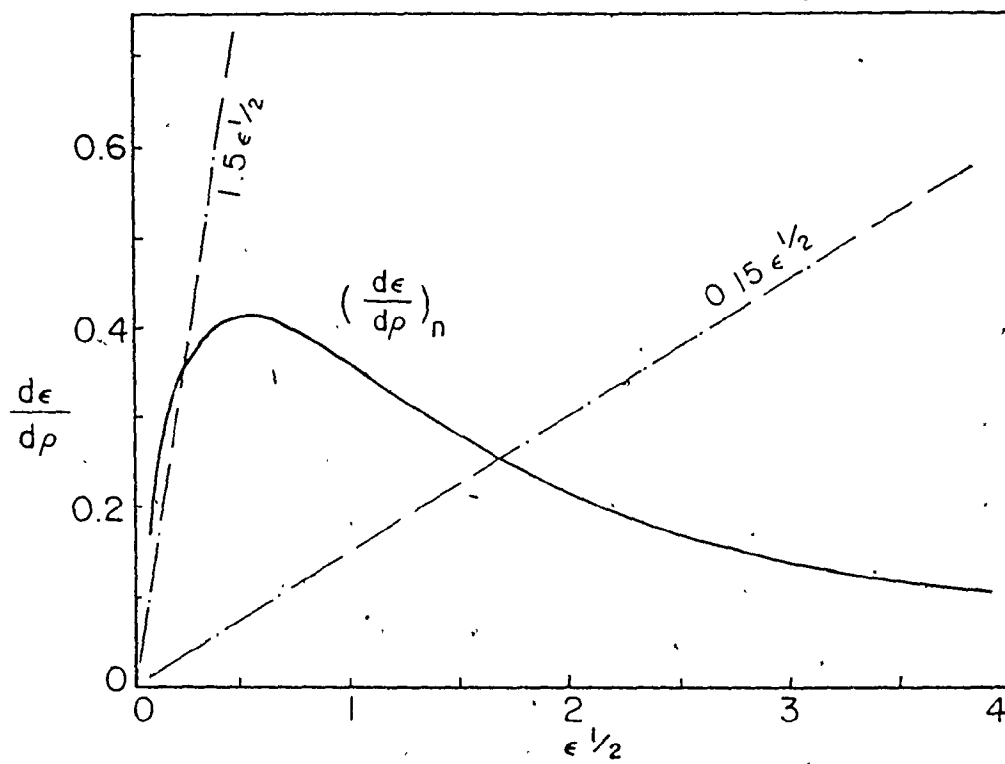
Fig. 2.3: Nuclear and electronic stopping power curves (Based on LSS theory).

$$\left(\frac{d\varepsilon}{d\rho}\right)_{total} = \left(\frac{d\varepsilon}{d\rho}\right)_n + \left(\frac{d\varepsilon}{d\rho}\right)_e \qquad (2.22)$$

and, the mean total reduced range, $<\rho>$, is given by

$$<\rho> = \int_0^\varepsilon \frac{d\varepsilon}{[\left(\frac{d\varepsilon}{d\rho}\right)_n + \left(\frac{d\varepsilon}{d\rho}\right)_e]} \qquad (2.23)$$

The differential cross section derived by Lindhard et. al. (7) is given by the following expression:

$$d\sigma = \pi a^2 \frac{dt}{2t^{3/2}} f(t^{1/2}) \qquad (2.24a)$$

where

$$t = \varepsilon^2 T/Tm \qquad (2.24b)$$

$f(t^{1/2})$ is a function that depends on the assumed form of the screening function. Winterbon, Sigmund and Sanders (19) used the following expression for the function $f(t^{1/2})$ which is very close to Lindhard's numerical curve,

$$f(t^{1/2}) = \lambda' \, t^{1/6}[1+(2\lambda' t^{2/3})^{2/3}]^{-3/2} \qquad (2.25)$$

where

$$\lambda' = 1.309$$

In their treatment, WSS used a power potential of the form,

$$V(r) = \frac{A}{r^{1/m}}; \quad \frac{1}{3} \leq m \leq 1 \qquad (2.26)$$

and the differential cross section is given by

$$d\sigma(E,T) = \frac{C \, dT}{E^m T^{1+m}} \qquad (2.27a)$$

where $m = 1/3$, $1/2$ or 1

$$C = \frac{\pi}{2} \lambda_m a^2 \left(\frac{M_1}{M_2}\right)^m \left(\frac{2Z_1 Z_2 e^2}{a}\right)^{2m}$$

where $\lambda_{1/3} = 1.309;$ \qquad (2.27b)

$$\lambda_{1/2} = 0.327; \quad \lambda_1 = 0.5$$

In general,

$m = \frac{1}{3}$ is valid for moderately low energies ($\varepsilon \lesssim 0.2$);

$m = \frac{1}{2}$ is valid for almost the whole range of keV energies ($0.08 \lesssim \varepsilon \lesssim 2$)

$m = 1$ is valid for high energies ($\varepsilon \gtrsim 10$)

2.5 Total Scattering Cross Section

From equation (2.25)

$$f(t^{1/2}) = 1.309t^{1/6}[1 + (2.618t^{2/3})^{2/3}]^{-3/2}$$

while from equation (2.24b)

$$t = \varepsilon^2 \, T/T_m = \varepsilon^2 \, x$$

Substituting back in equation (2.24a) gives

$$d\sigma = \pi a^2 \frac{\varepsilon^2 dx}{2\varepsilon^3 x^{3/2}} f(x,\varepsilon)$$

where

$$f(x,\varepsilon) = 1.309 \frac{(\varepsilon^2 x)^{1/6}}{[1 + (2.618 \, \varepsilon^{4/3} x^{2/3})^{2/3}]^{3/2}}$$

Therefore

$$d\sigma = 0.6545 \, \pi a^2 \frac{dx}{\varepsilon^{2/3} x^{4/3}[1 + (2.618 \, \varepsilon^{4/3} x^{2/3})^{2/3}]^{3/2}} \qquad (2.28)$$

Integrating over all possible values of x, i.e. all possible values of transferred energy, gives the total cross section, therefore

$$\sigma = 0.6545 \, \pi a^2 \int_{x_{min}=0}^{x_{max}=1} \frac{dx}{\varepsilon^{2/3} x^{4/3}[1+(2.618 \, \varepsilon^{4/3} x^{2/3})^{2/3}]^{3/2}} \qquad (2.29)$$

The integral on the R.H.S. of equation (2.29) does not depend on the specific collision partners. Therefore it is a universal value and is evaluated numerically. The lower limit of the integral is taken as 0.0001 instead of zero to avoid the singularity. Therefore;

$$Y = \int_{0.0001}^{1} \frac{dx}{\varepsilon^{2/3} x^{4/3}[1 + (2.618\varepsilon^{4/3} x^{2/3})^{2/3}]^{3/2}} \qquad (2.30)$$

The results of the total scattering cross section as a function of ε are shown in Appendix A.

2.6 Single-Collision Model

The single-collision model was proposed first by McCracken and Freeman (13) where they studied the backscattering of keV hydrogen. The interatomic potential used is the Coulomb potential and therefore the scattering cross section is given by the Rutherford formula. Because the single-collision model is often used in backscattering calculations, a brief description will be given here.

In this model, the ion trajectories before and after the nuclear collision are straight lines. Figure 2.4 shows the geometry of a single-scattering event. The ion starts at point A with incident energy E_0
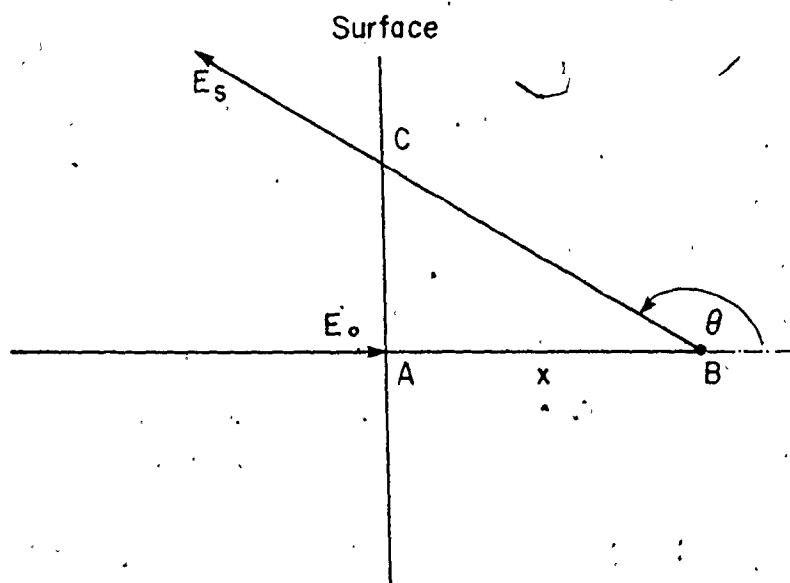
Fig. 2.4: Geometry of a single-scattering event.

and collides with a target atom at B after traversing a distance x inside the solid. During travelling from A to B, the ion loses energy

to the target electrons (through excitation and ionization or generally, inelastic collisions). The electronic energy loss is given by LLS formula

$$\frac{dE}{dx} = - K E^{1/2}$$

K is defined in equation (2.11) as:

$$Z_1^{1/6} \frac{Z_1 Z_2}{(Z_1^{2/3} + Z_2^{2/3})^{3/2}} 8\pi n e^2 a_0 \left(\frac{1}{E}\right)^{1/2}$$

Therefore, the energy of the incident particle before collision at B is given by,

$$E(x) = (\sqrt{E_0} - \frac{1}{2} Kx)^2 \qquad (2.32)$$

and hence the probability of a scattering event in any element of length dx is given by

$$dq = n\sigma \left[(\sqrt{E_0} - \frac{1}{2} Kx)^2, \theta\right] d\omega dx \qquad (2.33)$$

In the nuclear collision event, the particle will lose a discrete amount of energy determined by the conservation of energy and momentum. Using the relations in the previous sections,

$$E_2 = E(x)[1 - \gamma \sin^2(\frac{\theta}{2})] \qquad (2.34a)$$

where E_2 is the energy after nuclear collision at B. Substituting R^2 for $[1 - \gamma \sin^2(\frac{\theta}{2})]$, equation (2.34a) can be written as

$$E_2 = R^2 E(x) \qquad (2.34b)$$

If the measured scattered energy when the ion returns to the surface (point C) is E_s, then it can be readily shown that the depth at which the scattering event took place is given by

$$x = \frac{2(R\sqrt{E_0}-\sqrt{E_s})}{K(R-\sec\theta)}$$ (2.35)

Hence, using equation (2.33) and (2.35) the probability of an ion being scattered and emerging from the solid with an energy E_s is:

$$N(E_s)\,d\omega dE_s = \sigma\left[\left(\frac{\sqrt{E_s}-\sqrt{E_0}\,\sec\theta}{R-\sec\theta}\right)^2, \theta\right]\frac{n\,d\omega dE_s}{KE_s^{1/2}(R-\sec\theta)}$$ (2.36)

Assuming that Rutherford scattering applies in this case

$$\sigma(E,\theta)d\omega = \frac{1}{16}\left(\frac{Z_1^2 Z_2^2 e^4}{E^2}\right)\csc^4\left(\frac{\theta}{2}\right)d\omega$$

Therefore

$$N(E_s)d\omega dE_s = \frac{f(z)e^2\sqrt{E}\,\csc^4\left(\frac{\theta}{2}\right)(R-\sec\theta)^3 d\omega dE_s}{128\,\pi a_0\sqrt{E_s}(\sqrt{E_s}-\sqrt{E_0}\,\sec\theta)^4}$$ (2.37)

where

$$f(z) = Z_1^{5/6}Z_2(Z_1^{2/3}+Z_2^{2/3})^{3/2}$$

To obtain the total number of backscattered particles, equation (2.37) is integrated for all possible energies and scattering angles.

In their conclusion, McCracken and Freeman [13] indicated that one of the reasons that the absolute number of scattered ions measured experimentally is greater than the calculated values is that the

contribution of multiple scattering was ignored. This multiple scattering contribution becomes increasingly large for lower ion energies or heavier targets.

Vukanic and Sigmund (20) used the same single-scattering model with a screened Coulomb potential. They used a simple power cross section to avoid the complexities of using the Thomas-Fermi cross section at the expense of accuracy. Good agreement with experiments was obtained for $\varepsilon > 3$. For smaller values of ε, as they have also indicated, multiple collisions have an appreciable contribution to the backscattered spectra.

2.7 Application of the Transport Theory

Weissmann and Sigmund (21) used the integro-differential equation technique (transport equation) to study the backscattering of keV light ions. They assumed a random infinite target and used the Thomas-Fermi cross section.

The range distribution of an ion beam is given by $F_R(x,E,\eta)$, where x is the penetration depth, E the initial energy, and $\eta = \cos\theta$, θ being the initial angle between the beam and the x-direction. F_R is determined by the following equation (17,22):

$$-\eta \frac{\partial F_R}{\partial x} = NS_e \frac{\partial F_R}{\partial E} + N \int d\sigma_n (F_R - F_R')$$

(2.38)

and the distribution is normalized

$$\int_{-\infty}^{\infty} dx F_R(x,E,\eta) = 1$$

(2.39)

The reflection coefficient $R = R(E,\eta)$ is given by,

$$R = \int_{-\infty}^{0} dx F_R(x,E,\eta) \quad . \tag{2.40}$$

This means that the number of reflected particles is given by the tail of the distribution F_R, i.e. the profile intersection with the target surface.

From equation (2.38), the moment equations can be found (19):

$$n\ell F_{R_{\ell-1}}^{n-1} + n(\ell+1)F_{R_{\ell+1}}^{n-1} = (2\ell+1)NS_e \frac{dF_{R\ell}^{n}}{dE}$$

$$+ (2\ell+1)N \int d\sigma_n [F_{R\ell}^{n}(E) - P_\ell(\cos\phi')F_{R\ell}^{n}(E-T)] \tag{2.41}$$

where $F_{R\ell}^{n} = F_{R\ell}^{n}(E)$ are the coefficients in the Legendre-polynomial expansion,

$$\int_{-\infty}^{\infty} dx\, x^n F(x,E,\eta) = \sum_{\ell=0}^{n} (2\ell+1)F_{R\ell}^{n}(E)P_\ell(\eta) \tag{2.42}$$

and ϕ' is the laboratory scattering angle.

Using dimensionless quantities, ε and ρ, we get

$$F_{R\ell}^{n}(\varepsilon) = \left(\frac{\rho}{x}\right)^n F_{R\ell}^{n}(E) \tag{2.43}$$

Equation (2.41) is numerically integrated to determine the Legendre coefficients. With these coefficients, the moments can be determined and the range distributions constructed from the Edgeworth series

expansion (19,23,24):

$$f_R(\rho,\varepsilon,\eta) = \frac{1}{<\Delta\rho^2>^{1/2}} [\phi_0(\xi) - \frac{\Gamma_1}{6} \phi_3(\xi) + ...] \qquad (2.44a)$$

where

$$\xi = \frac{\rho - <\rho>}{<\Delta\rho^2>^{1/2}} \qquad (2.44b)$$

$$\Gamma_1 = \frac{<\Delta\rho^3>}{<\Delta\rho^2>^{3/2}} \qquad (2.44c)$$

and $\phi_0(\xi)$ and $\phi_3(\xi)$ are the gaussian* and its third derivative.

The total reflection coefficient $R(\varepsilon,\eta)$ is found to a first approximation by integrating $f_R(\rho,\varepsilon,\eta)$ (21):

$$R(\varepsilon,\eta) = \int_{-\infty}^{0} d\rho f_R(\rho,\varepsilon,\eta) \qquad (2.45)$$

The problem with the transport theory is that the energy distribution cannot be determined and a "surface correction" must be applied to the solution to account for the multiple crossing of the free surface (25).

Figure 2.5 shows the calculated projected range distribution for protons in heavy targets in dimensionless units (21).

* The gaussian approximation is defined by

$$\phi_0(\xi)d\xi = \frac{d\xi}{\sqrt{2\pi}} e^{-\xi^2/2}$$
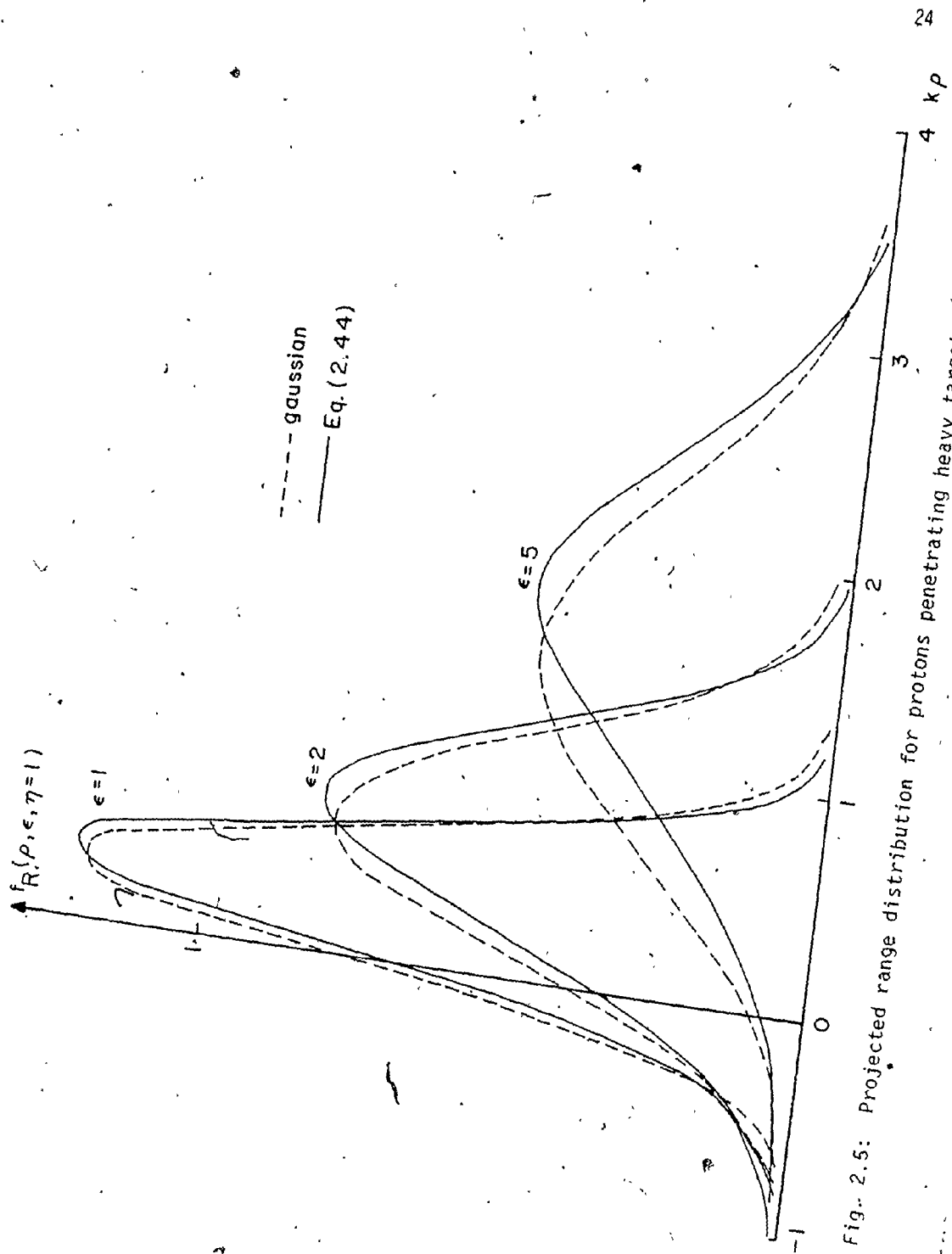
Fig. 2.5: Projected range distribution for protons penetrating heavy targets (from ref. 18)

CHAPTER 3

COMPUTER SIMULATION OF ION SCATTERING

3.1 Introduction to Computer Simulation

To avoid the problems encountered in the transport theory, namely, the surface correction and the inability to calculate the back-scattered energy distribution, also to include the multiple scattering effect which was avoided in the single-collision model, computer simulation or a Monte-Carlo technique was used to study the incident particle-target atoms interactions.

In the Monte-Carlo technique, the histories of a large number of particles (same initial conditions) are determined by following successive scattering events as each particle travels through the solid until it slows down or backscatters out of the surface. The larger the number of particles followed, the closer are the results to the average behavior but this will be at the expense of additional computer time. Figure 3.1 shows the paths of two primary projectiles as they penetrate the target.

25
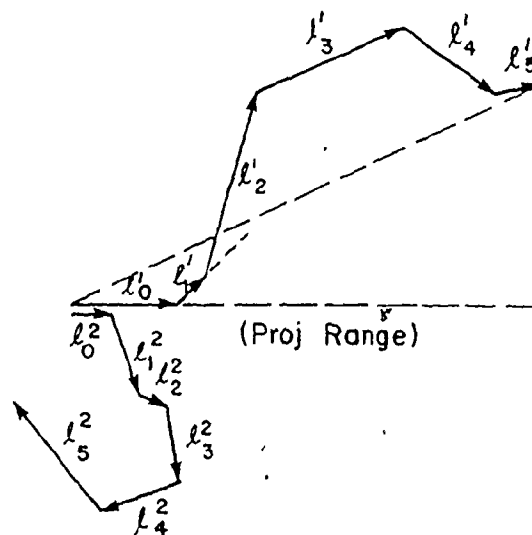
Fig. 3.1: The paths of two primary projectiles broken up into linear
segments

. At each scattering point the appropriate interaction probabilities
could be determined by the use of random numbers.

Robinson, Oen and Holmes (10,26,27) and Beeler and Besco (28)
have successfully applied this technique to various models of nuclear
scattering, but without consideration of electronic energy loss. For
this reason their models are valid only for heavy ion beams. Ishitani
et. al. (29) applied the Monte-Carlo technique to study the behavior
of light ion beams in amorphous targets considering both nuclear and
electronic stopping. But they used the mean free path concept which
will be discussed in the next section.

3.2 Computer Model

In this thesis the Monte-Carlo technique was applied to the scattering of light ions from different substrates (30,31). The cases studied here are for hydrogen and helium ions (5-15 keV) incident normally on a silicon target. Both nuclear and electronic collisions are considered together with multiple collisions inside the solid.

The following assumptions were made: (1) the solid has a random or amorphous-like structure, (2) the electronic stopping is assumed to be proportional to the speed of the incident particles, (3) the Thomas-Fermi interaction potential is used to describe binary incident particle-target atom collisions, and (4) the motion of the target atoms upon receiving collision energy can be assumed negligible. The last assumption is valid only for the case of an infinite medium and is not valid near the free surface.

The usual way to find the location of a nuclear collision is the use of the mean free path concept. The mean free path, which is the average distance between collisions, is the reciprocal of the macroscopic scattering cross section, which is energy dependent, and so will be continuously varying in this case due to electronic energy loss. An alternative scheme, which was used in these calculations was developed as follows:

From the continuous energy loss due to electronic collision, the reduced energy as a function of the reduced range is deduced from equation (2.20):

$$\varepsilon(\rho) = (\varepsilon_0^{\frac{1}{2}} - \frac{1}{2} k\rho)^2 \tag{3.1}$$

An ion will move in the solid until its energy reaches a minimum value. This value will be taken 25 eV, similar to the threshold energy for atomic displacement, and at this energy the ion is assumed to be absorbed. Assume the total distance at which the ion is stopped is ρ_{max}, which corresponds to an ion energy $E_{min} = 25$ eV. The probability that at least one nuclear scattering event occurs is p_n and it is given by

$$p_n = 1 - \exp[-\int_0^{\rho_{max}} (\frac{x}{\rho}) N\sigma(\varepsilon) d\rho'] \tag{3.2}$$

where $\sigma(\varepsilon)$ is the scattering cross section as a function of energy (and consequently a function of position). This probability p_n varies from 0 to 1. If a random number q is chosen at a particular ρ, and if $q \geq p_n$, no nuclear scattering will occur. If $q < p_n$, at least one nuclear scattering event will occur before the particle energy is reduced to 25 eV by electronic energy losses. Hence, the probability that a nuclear scattering event occurs at distance $\rho(<\rho_{max})$ is given by the expression:

$$q = 1 - \exp[-\int_0^0 (\frac{x}{\rho})N\sigma(\varepsilon) d\rho'] \tag{3.3}$$

This equation could be written in the form: -

$$q = 1 - \exp[-\int_0^{\rho_{max}} (\tfrac{x}{\rho})N\sigma(\varepsilon)d\rho'] \exp[\int_\rho^{\rho_{max}} (\tfrac{x}{\rho})N\sigma(\varepsilon)d\rho'] \qquad (3.4)$$
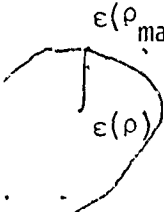
Substituting equation (3.2) into equation (3.4), the following form for q can be found,

$$q = 1 - (1-p_n) \exp[\int_\rho^{\rho_{max}} (\tfrac{x}{\rho})N\sigma(\varepsilon)d\rho'] \qquad (3.5)$$

Therefore

$$\int_\rho^{\rho_{max}} (\tfrac{x}{\rho})N\sigma(\varepsilon)d\rho' = \ln\left(\frac{1-q}{1-p_n}\right) \qquad (3.6)$$

By changing variables in equation (3.6) using the relation of equation (2.20), equation (3.6) can be written as:

$$\int_{\varepsilon(\rho)}^{\varepsilon(\rho_{max})} - (\tfrac{x}{\rho}) \frac{N\sigma(\varepsilon')d\varepsilon'}{k(\varepsilon')^{1/2}} = \ln\left(\frac{1-q}{1-p_n}\right)$$

i.e.

$$\int_{\varepsilon_{min}}^{\varepsilon(\rho)} (\tfrac{x}{\rho}) \frac{N\sigma(\varepsilon')d\varepsilon'}{k(\varepsilon')^{1/2}} = \ln\left(\frac{1-q}{1-p_n}\right) \qquad (3.7)$$

If the integral in the L.H.S. of equation (3.7) is substituted by the expression $R(\varepsilon)$, therefore

$$R(\varepsilon) = \int_{\varepsilon_{min}}^{\varepsilon} (\tfrac{x}{\rho}) \frac{N\sigma(\varepsilon')d\varepsilon'}{k(\varepsilon')^{1/2}} \qquad (3.8)$$

Now, equation (3.2) can be rewritten as

$$P_n = 1 - \exp\left[-\int_{\epsilon_{min}}^{\epsilon_0} \left(\frac{x}{\rho}\right)\frac{N\sigma(\epsilon')d\epsilon'}{k(\epsilon')^{1/2}}\right] = 1 - \exp[-R(\epsilon_0)] \qquad (3.9)$$

Substituting (3.8) into (3.5) gives

$$q = 1 - (1-P_n) \exp[R(\epsilon)]$$

$$= 1 - \exp[-R(\epsilon_0)] \exp[R(\epsilon)]$$

$$= 1 - \exp[R(\epsilon) - R(\epsilon_0)]$$

Therefore

$$R(\epsilon) - R(\epsilon_0) = \ell n \ (1-q) \qquad \qquad (3.10)$$

To summarize the equations that will be used in the calculations, it could be found that the following four equations will be used,

$$\epsilon(\rho) = (\epsilon_0^{\frac{1}{2}} - \frac{1}{2} k\rho)^2 \qquad (3.1)$$

$$R(\epsilon) = \int_{\epsilon_{min}}^{\epsilon} \left(\frac{x}{\rho}\right)\frac{N\sigma(\epsilon')d\epsilon'}{k(\epsilon')^{1/2}} \qquad (3.8)$$

$$P_n = 1 - \exp[-R(\epsilon_0)] \qquad (3.9)$$

and

$$R(\epsilon) - R(\epsilon_0) = \ell n \ (1-q) \qquad (3.10)$$

Now the following steps should be followed to determine the location of a nuclear collision:

1. tabulate values of $R(\varepsilon)$ for different incident energies down to
   25 eV using equation (3.8),

2. determine p_n from $R(\varepsilon_0)$ using equation (3.9),

3. choose a random number q and check if $q < p_n$,

4. determine $R(\varepsilon)$ from equation (3.10) and consequently $\varepsilon(\rho)$ from
   the first step, and

5. use equation (3.1) to determine the position of nuclear scattering,
   ρ, after knowing $\varepsilon(x)$ from the fourth step.

For the tabulation of $R(\varepsilon)$ for different values of energies,
the following integral has to be evaluated,

$$R(\varepsilon) = \int_{\varepsilon_{min}}^{\varepsilon} \left(\frac{x}{\rho}\right) \frac{N\sigma(\varepsilon')d\varepsilon'}{k(\varepsilon')^{1/2}}$$

From section 2.5, the scattering cross section is given by,

$$\sigma(\varepsilon) = 0.6545 \, \pi a^2 \, Y(\varepsilon) \qquad\qquad (3.11)$$

where $Y(\varepsilon)$ is given by equation (2.30), therefore

$$R(\varepsilon) = \frac{0.6545 \, \pi a^2 N}{k} \left(\frac{x}{\rho}\right) \int_{\varepsilon_{min}}^{\varepsilon} \frac{Y(\varepsilon')d\varepsilon'}{(\varepsilon')^{1/2}} \qquad\qquad (3.12a)$$

substitute $[Y(\varepsilon')/(\varepsilon')^{1/2}]$ by $F(\varepsilon')$, therefore

$$R(\varepsilon) = \frac{0.6545}{\gamma k} \int_{\varepsilon_{min}}^{\varepsilon} F(\varepsilon')d\varepsilon' \qquad\qquad (3.12b)$$

where

$$\gamma = \frac{4M_1 M_2}{(M_1 + M_2)^2}$$

The nuclear differential cross section for energy transfer between T and T + dT, normalized to a total probability of unity is given by (29):

$$p(T)dT = d\sigma(T) / \int_{T_{min}}^{T_{max}} \frac{d\sigma(T)}{dT} dT \qquad (3.13)$$

Integrating equation (3.13) gives:

$$p = \int_{T_{min}}^{T} \frac{d\sigma(T)}{dT} dT / \int_{T_{min}}^{T_{max}} \frac{d\sigma(T)}{dT} dT \qquad (3.14)$$

In equation (3.14), p will be a fraction between 0 and 1. In the present calculation p will be chosen as a random number q′. Therefore equation (3.14) becomes;

$$q' = \int_{T_{min}}^{T} d\sigma(T) / \int_{T_{min}}^{T_{max}} d\sigma(T) \qquad (3.15)$$

The denominator in the R.H.S. of equation (3.15) is the total nuclear scattering cross section evaluated in section 2.5. Equation (3.15) can be rewritten in the form,

$$q' Y(\varepsilon) = \int_{0.0001}^{x} \frac{dx}{\varepsilon^{2/3} x^{4/3} [1 + (2.618 \; \varepsilon^{4/3} x^{2/3})^{2/3}]^{3/2}} \qquad (3.16)$$

using the expression for $d\sigma$ derived in equation (2.28). The integral in the R.H.S. of equation (3.16) is evaluated for different values of x (from x = 0.0001 to x = 1). Therefore, for any random number q', it is possible to find the value of x that satisfies equation (3.15). Since $x = T/T_m$, therefore using equation (2.3) gives,

$$\sin^2(\theta/2) = x \qquad (3.17)$$

From equation (3.17) the scattering angle θ, in the center of mass coordinates, is determined.

In addition to the collision angle ψ, the azimuthal angle ϕ should be determined. The value of the angle ϕ varies from 0 to 2π. Therefore, choosing a third random number q'', the azimuthal angle is determined by,

$$\phi = q''.2\pi \qquad (3.18)$$

3.3 Description of the Complete Computation Work

This section is a summary of the computational steps discussed before, and in addition the calculated parameters and method of calculation are described.

First for the given initial energy E_0, the first nuclear collision location is determined, and the energies before and after collision are evaluated. In the same way, the calculation proceeds to the second and third collisions, ... etc. At each location, the projected range is calculated. A check is undertaken to determine

whether the projected range is negative or positive. In the former
case, the particle is backscattered and in this case the energy
and angle, that the outgoing particle makes with the original direction,
are determined. To calculate the backscattered energy, the distance
from the last scattering to the surface, DS, is determined and the
energy will be given using equation (3.1) by substituting x by DS.
If, on the other hand, the projected range is positive, check that the
particle energy is higher than a minimum value, taken here as 250 eV
(to reduce computation time). In a somewhat more exact case, all
interactions down to $\sim$ 25 eV should be considered.

After finishing the history of the first particle, backscattered
or absorbed, the same procedure is repeated for the remaining particles
with the same initial conditions. Therefore, it is possible to find
the number of backscattered particles, and their energy and angular
distributions.

The same calculation procedure is repeated for different
incident energies for hydrogen and helium ions incident on a silicon
target to examine the effect of the incident particle and energy on
the backscattered energy and angular distributions.

3.4 Results and Discussions

The model developed in section 3.2 was applied to hydrogen and helium ions incident normally on a random silicon target. The incident energies considered were 5, 10, and 15 keV. Both energy and angular distributions were calculated. The number of incident particles ranged from 5,000 to 10,000 depending on the incident ion and energy i.e. depending on the scattering cross section. The limiting factor was the computation time.

As was mentioned before, the electronic energy loss is given by LSS formula

$$\frac{d\varepsilon}{d\rho} = -k\varepsilon^{\frac{1}{2}}$$

where k is given by equation (2.21). It was found by Ormrod and Duckworth (32) that the electronic energy loss exhibits oscillations which are functions of Z_1 (incident particle). Recently, Thompson et. al. (33) found by comparing measured and calculated damage profiles that higher values for k should be used, depending on the incident particle, instead of these given by LSS. For hydrogen and helium k should be replaced by 1.55 k. This new value of k was used in the present calculations.

Figures 3.2(a) and (b) show the energy and angular distributions for 5 keV hydrogen ions incident on a random silicon target. The following table gives a summary of the computer simulation results.
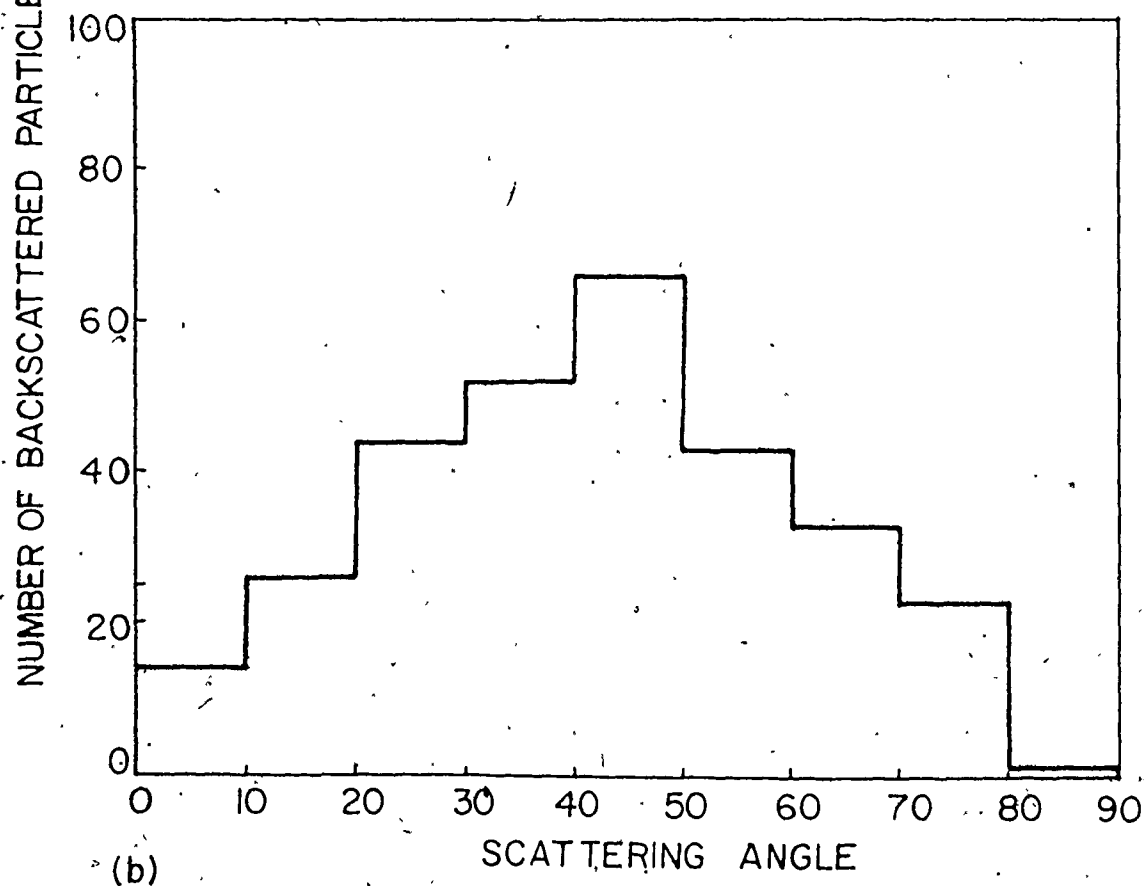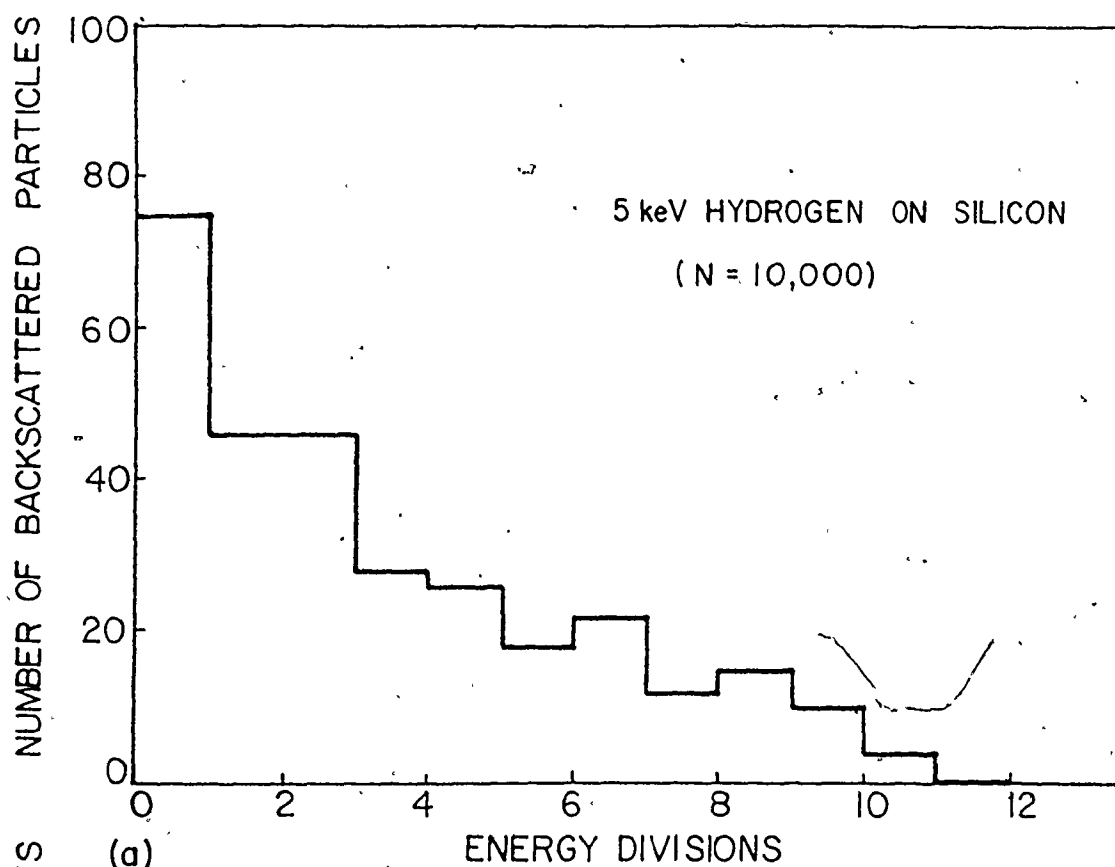
Fig. 3.2: Monte-Carlo calculation for 5 keV H/Si (N = 10,000)
(a) energy distribution, (b) angular distribution.

Reflection Coefficients and Scattered Energy Fractions for H and He Ions
Incident on Amorphous Silicon Targets (Normal Incidence, E_{cut} = 250 eV)

Scattering	E_0(keV)	ε_0	k/k_L	R	γ^*
(H,Si)	5.0	4.30	1.55	0.030	0.010
(H,Si)	10.0	8.60	1.55	0.014	0.004
(H,Si)	15.0	12.90	1.55	0.010	0.002
(He,Si)	5.0	1.87	1.55	0.080	0.022
(He,Si)	10.0	3.74	1.55	0.052	0.012
(He,Si)	15.0	5.61	1.55	0.023	0.005

$$\gamma^* = \frac{\sum_{i=1}^{N} E_i}{NE_0} \times R, \quad E_i \text{ is the energy of the ith scattered particle.}$$

From the obtained spectra, it was found that most backscattered
particles come from inside the target i.e. there is a depletion in
surface scattering. Comparing the spectra for different energies for
the same incident ion (within the statistical errors) it was found that
the lower the incident energies, the higher the backscattered energy
fractions. Also comparing hydrogen and helium spectra, the helium
cases show more scattering from the outside layers than does hydrogen.
This should be expected when one compares the values of the reduced

energies for both ions incident on silicon (ε = 0.8599/keV for hydrogen

and 0.3738/keV for helium) (34).

For both ions and for all incident energies, some particles are

backscattered with energies higher than those corresponding to single

scattering collisions from the surface atoms. This shows that multiple

scattering takes place at and near the target surface. This phenomena

was also found experimentally,as will be shown in Chapter 6.

From the angular distribution spectra, it could be roughly

assumed that the angular distribution is approximately a cosine

function. This has been observed experimentally by Verbeek (35) for

hydrogen incident on a niobium polycrystalline target.

CHAPTER 4

APPARATUS AND EXPERIMENTAL TECHNIQUE

4.1 Introduction

To study the scattering of low and medium energy ions from solid surfaces, an experimental ion scattering facility was constructed. In this energy range, as will be seen in detail in Chapter 7, most of the backscattered particles are neutrals. Therefore, the use of an electrostatic analyzer (ESA) will not be applicable for detecting the backscattered neutral particles. A time-of-flight (TOF) technique, originally proposed by Buck et. al. (5), was used to detect both neutrals and ions backscattered from the solid surfaces.

In ion bombardment experiments, the target surface is continuously cleaned by the incident ions. The target is kept clean if the number of incident ions is much larger than residual gas molecules impinging on the target. In this case there is no need for UHV (10^{-9}-10^{-10} Torr) in the target chamber. Unfortunatley, this is not the case in backscattering studies, especially those using TOF technique since the incident beam current is very low, to avoid damage of the target surface. Therefore, for efficient ion scattering experiments an UHV scattering chamber is required. The pressure has to remain in the 10^{-9} Torr range during the experiment (with ion beam impinging on the target).

To maintain low pressure in the target chamber, a system of apertures (2 mm diameter) is used. This involves an efficient beam
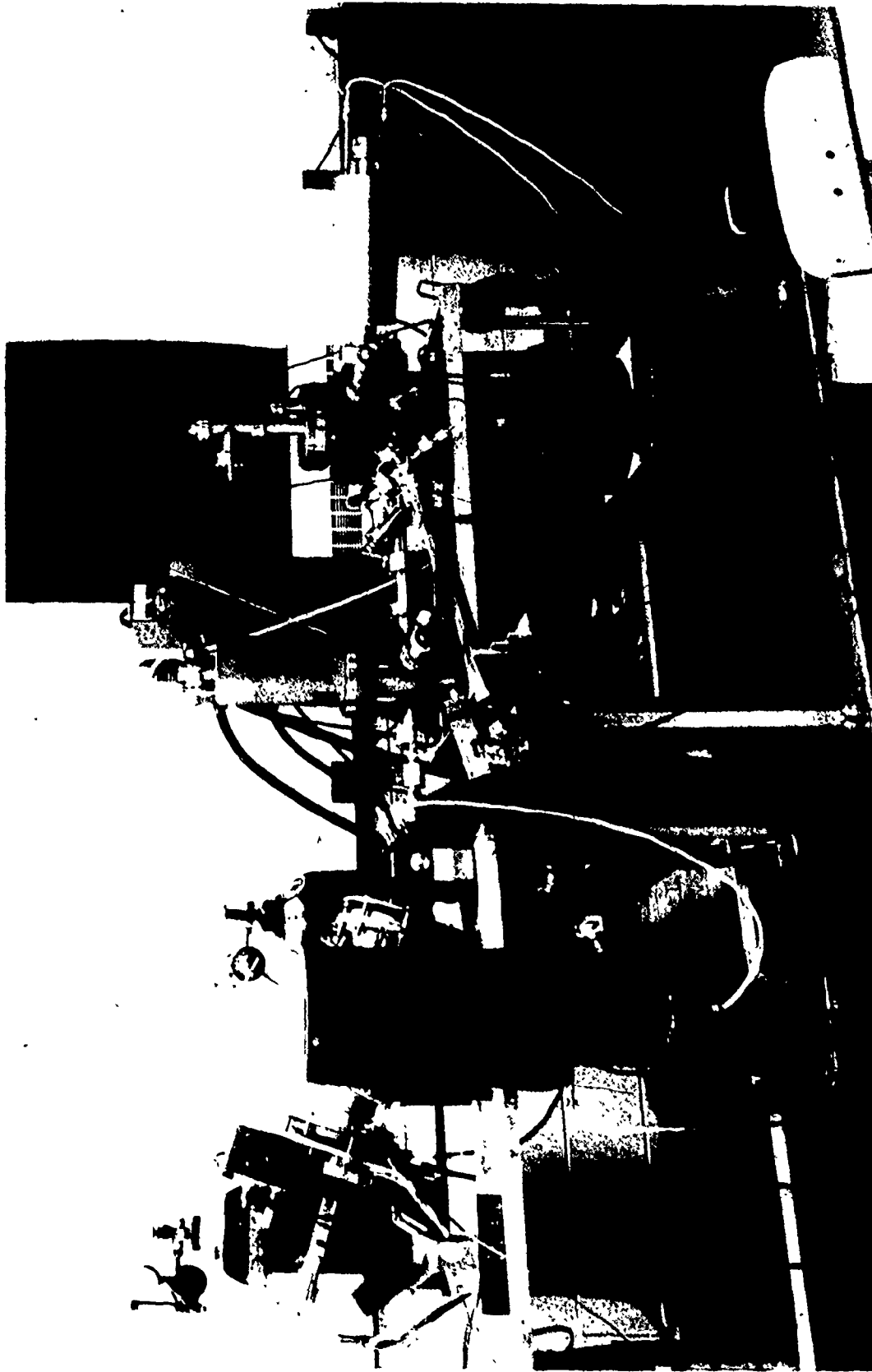
Fig. 4.1: Photograph of the experimental system.

focusing and alignment system. The ion beam has to be magnetically analyzed to get rid of all undesirable ions that might hit the target with the original ions. Also, precautions were taken to prevent any neutral particles from hitting the target. This is of extreme importance in TOF measurements to ensure good signal to noise ratio. Figure 4.1 shows a photograph for the ion scattering facility designed for this work.

4.2 Ion Generation

A radio-frequency ion source, Ortec model 501, is used to generate the ion beam. Its operation depends on the electrons gaining energy from the r-f field and ionizing gas atoms in their oscillatory paths. The ions are extracted by the voltage difference between the discharge tube head (extraction voltage and accelerating voltage) and the base plate (accelerating voltage only). Very pure gases are fed at the base plate to generate the desired ion beam.

The ion beam produced by the R-F ion source is divergent. For this model, the divergence angle is 14°. Therefore the beam is focussed before being analyzed by the deflecting magnet. To increase the beam current at the target, two einzel lenses are used instead of only one lens. The dimensions of the lenses used are shown in Figure 4.2; the details of the lens design can be found in ref. (36). The second lens focuses the beam at the aperture A (3 mm) just before the magnet section.
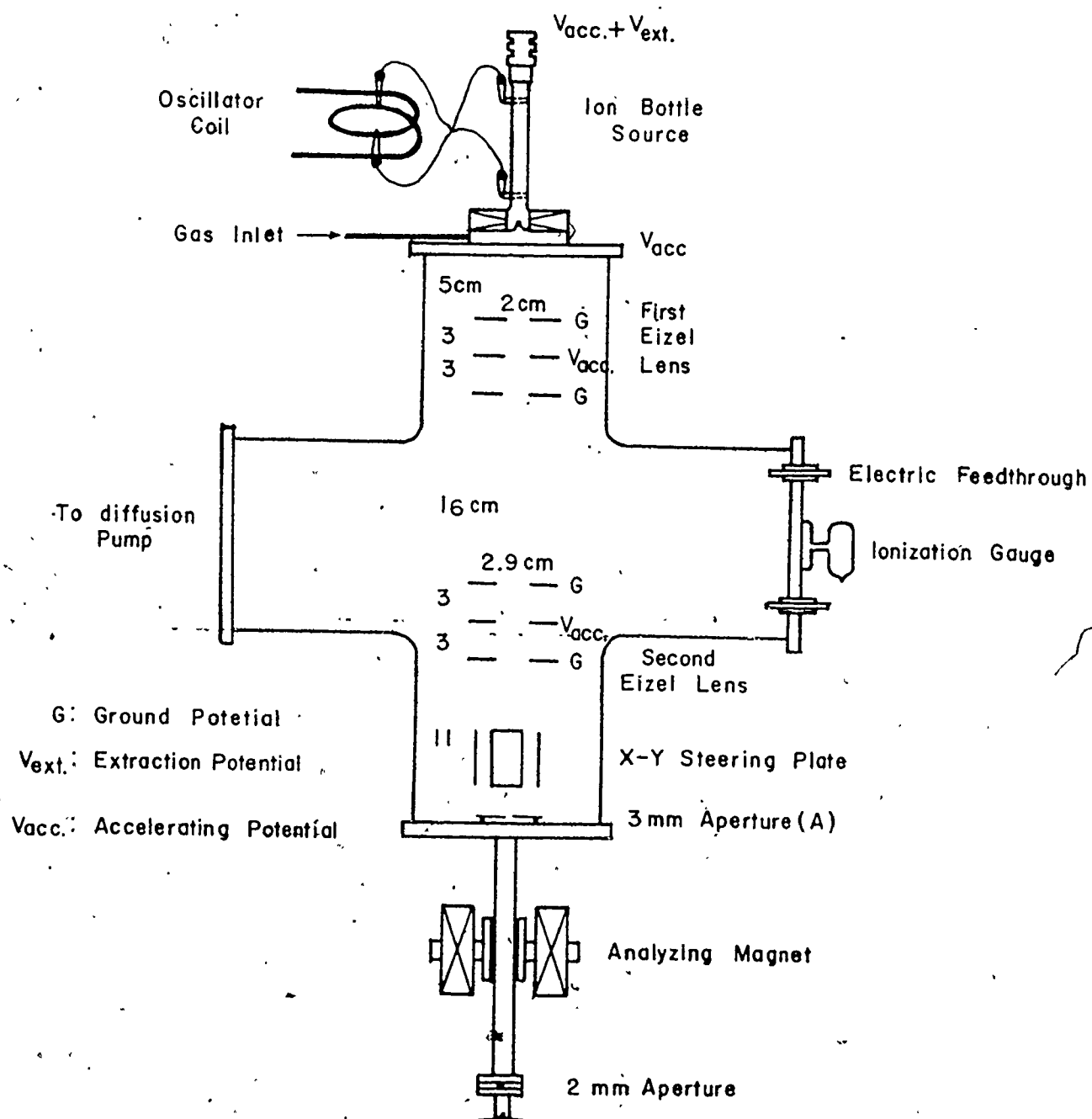
Fig. 4.2: Schematic diagram of the accelerator section.

To ensure that a single ion species will enter the target

chamber, the focussed beam is magnetically analyzed and deflected

through a 20° angle.In this work the magnet coils were connected in

parallel and the magnet was calibrated as shown in figure 4.3. To

prevent overheating of the magnet coils, cold water is circulated

through them. Typical values for the magnetic fields required, for

10 keV ion beams, are as follows: 480 Gauss for hydrogen and 960 Gauss

for helium. Two pieces of soft iron are attached to the magnet

poles to improve the focusing properties of the analyzing magnet.
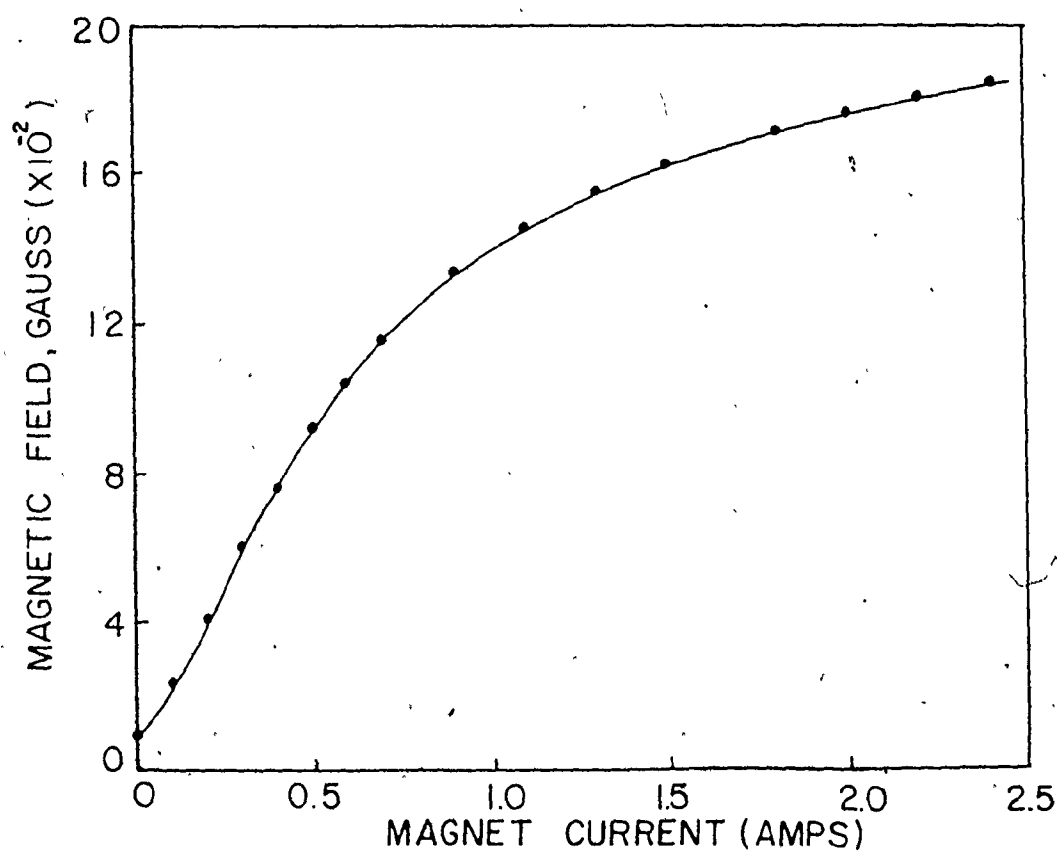
Fig. 4.3: Magnet Calibration.

Because of the use of small apertures (2 mm), mechanical alignment is not sufficient. Beam alignment is therefore achieved with two sets of deflecting plates. The first set lies directly after the second einzel lens; and the second set after the analyzing magnet in the differential pumping chamber.

An operating pressure of roughly 1×10^{-6} Torr is maintained in the accelerator section by a conventional oil diffusion pump equiped with liquid nitrogen cold trap. The exhaust of the diffusion pump goes to a rotary pump through another liquid nitrogen cold trap to prevent oil streaming to the accelerator chamber.

4.3 Differential Pumping System

To reach the UHV target chamber, the ion beam passes through a differentially pumped chamber. A 2 mm aperture, located at each end of the chamber, collimates the beam and provides the necessary pumping impedence for maintaining the differential pressure between the beam source pressure (1×10^{-6} Torr) and the UHV target chamber pressure (6×10^{-9} Torr). This is shown schematically in figure 4.4. The differential chamber is pumped by a 50 l/sec diode ion pump and 2000 l/sec titanium sublimation pump (water cooled surface); it is usually roughed by using a sorption pump. The pressure in the differential pumping section is normally 4×10^{-8} Torr while running the experiment. The differential chamber is separated from both the accelerator and the target chamber by straight-through valves.

CHANNELTRON

SECONDARY ELECTRON
SUPPRESSION SCREEN

TARGET

GAS
ANALYSER

TIME-OF-FLIGHT
TUBE

UHV TARGET CHAMBER

DIFFERENTIAL
PUMPING

MASS ANALYSED ION SOURCE
(1 - 30 keV)
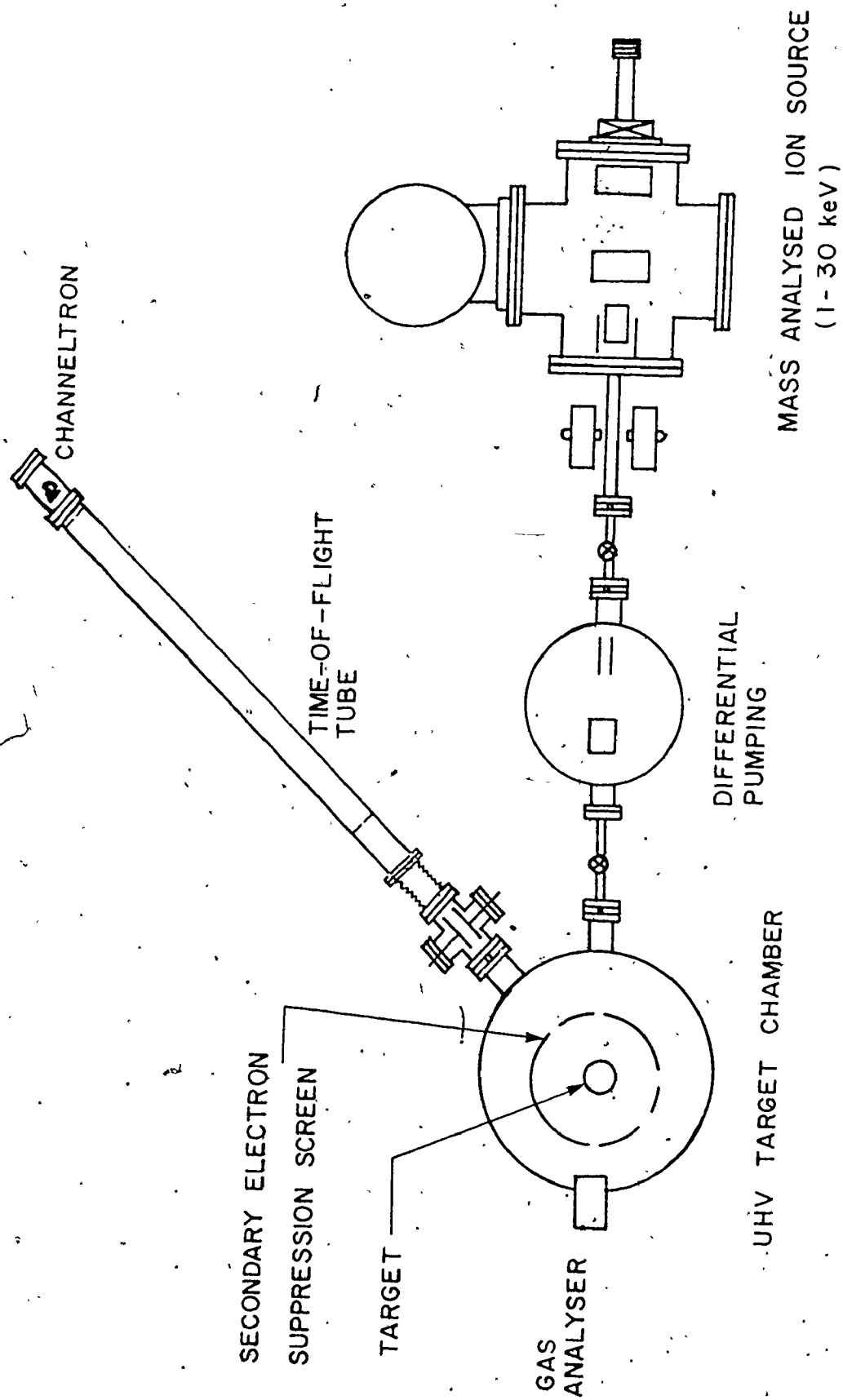
Fig. 4.4: Schematic diagram of the experimental system.

The UHV target chamber has a diameter of 25 cm and a height of 36 cm. All flanges and valves are metal sealed and bakeable to 200°C (maximum-allowed for the detector). Rough pumping of the chamber is done by a sorption pump. UHV is accomplished with 100 1/sec triode ion pump and 2000 1/sec titanium sublimation pump (water cooled surface). There is a quadrupole mass spectrometer for residual gas analysis in the target chamber. Figure 4.5 is a typical residual gas analysis for the target chamber. The total pressure after 24 hours baking (at 200°C) was 6×10^{-9} Torr and the main contaminants are hydrogen and argon. With the ion beam hitting the target, the pressure in the target chamber rises to about 8×10^{-9} Torr.
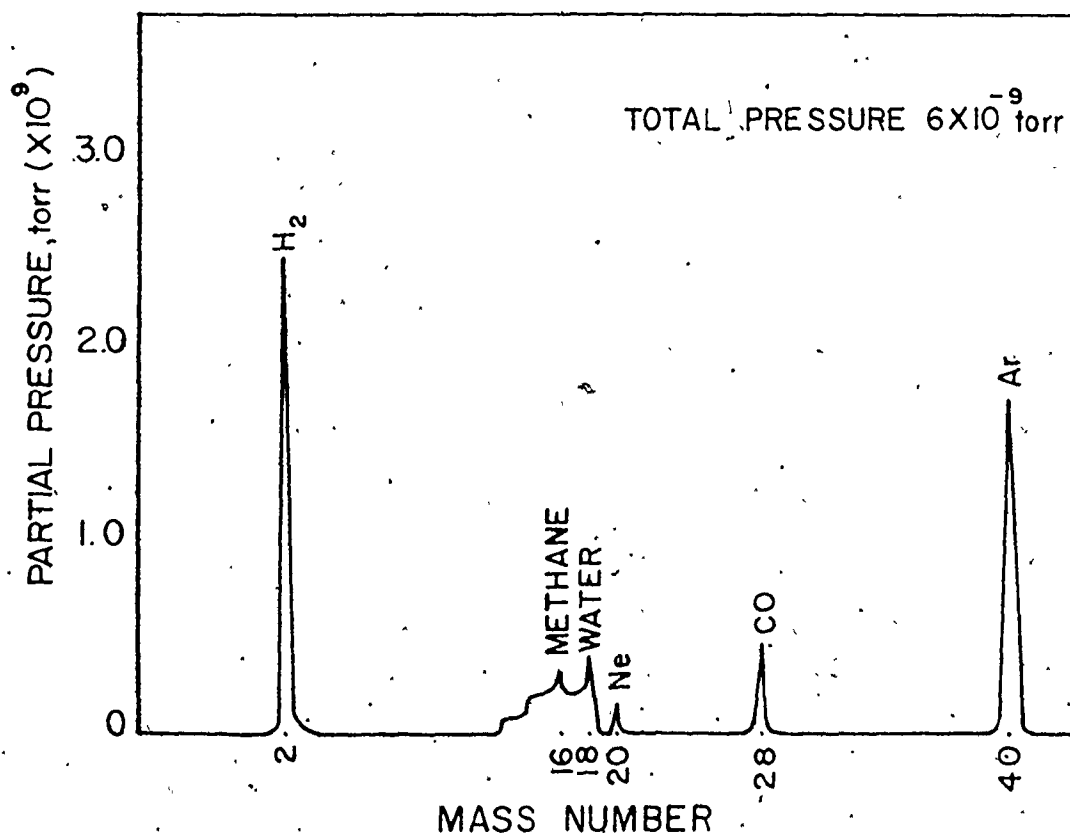
Fig. 4.5: Target chamber gas analysis.

As shown in figure 4.4, at 45° from the incident beam there is a 110 cm long tube used for time-of-flight measurements as will be seen. There is also a 5 cm diameter and 20 cm long tube, surrounding the target, acting as a seondary electron suppression screen. The target itself is mounted on a simple rotary feedthrough and is connected to a picoammeter and a current integrator.

4.4 Experimental Technique

Time-of-flight technique was used to measure both neutrals and ions scattered from the target. This was done by adding a deflection beam pulsing system between the analyzing magnet and the UHV target chamber. The backscattered particles travel along the 110 cm flight tube and are detected by a spiral channel electron multiplier (channeltron) detector located at the end of the tube. Pulses from the beam pulsing system and the channeltron are fed to the time-to-amplitude converter (TAC) which in turn supplies input pulses to a multichannel pulse height analyzer (PHA). Figure 4.6 shows a schematic drawing for the time-of-flight system used in these measurements.

4.4.1 Beam Pulsing System

The beam pulsing system consists of a set of electrostatic pulsing plates located in the differential pumping chamber. The plates are 3 cm long and are spaced 4 mm apart. The distance between the
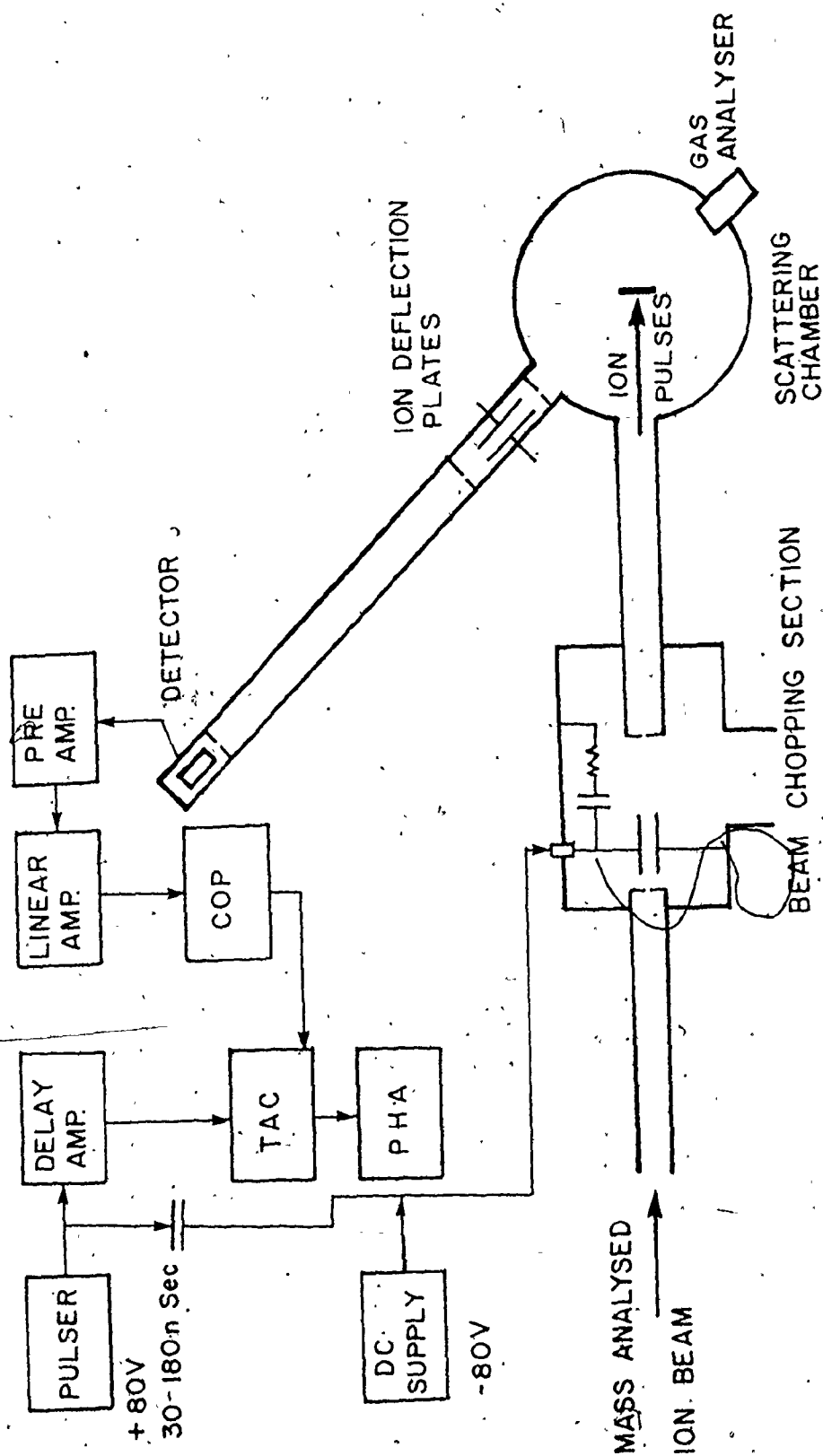
Fig. 4.6: Block diagram of the detection system.

pulsing plates and the target is 65 cm. Initially the ion beam is focussed through the different apertures on to the target with both plates at ground potential. The beam is then held off the target vertically by applying -80 volts bias, using the DC power supply, on the pulsing plates. Pulses of a duration of 30-180 nanoseconds and repetition rate of 5-80 kHz are then applied to the plates; this will intermittently ground the plates and return the beam to the target as a pulsed beam. A special pulse generator was developed. Its circuit diagram is shown in Appendix C. It is capable of generating +80 volts pulse with a 3 nanoseconds rise time. The pulse width can be changed with an adjustable length coaxial cable.

The low energy ions will take a longer time to travel through the pulsing plates. Therefore, for a given ion energy there is a minimum pulse width required in order to allow ions to pass through the plates before the deflecting field is reapplied. On the other hand, the pulse width should be as small as possible to obtain a good time-of-flight resolution as will be shown.

4.4.2 Detector and Detection System

The detector used in the present measurements is a Mullard channel electron multiplier with a circular cone located at the end of the time-of-flight tube. The voltage difference across the channeltron is 2200 volts which gives an electron gain of 10^8 (37). The channeltron efficiency for detecting positive, negative and neutral particles was measured down to 500 eV (38,39).

The detection system was shown in figure 4.6. When a pulse is applied to the pulsing plates, another pulse (-4 volts) from the same pulse generator is used as a START pulse to the TAC. The backscattered particles are detected by the channeltron and the output signal goes through a standard nuclear data system components. This consists of a preamplifier, linear amplifier and a cross-over-pickoff. The signal from the cross-over-pickoff goes to the TAC as a STOP signal. The amplitude of the output signal from the TAC is proportional to the time difference between the START and STOP signals. The TAC output signal is fed to the PHA which records the time-of-flight spectrum of the backscattered particles. The START pulse is usually delayed using a delay amplifier before going to the TAC. This delay accounts for the time which the incident particle takes from the pulsing plates to the target (65 cm) and also to the delay in the electronic components.

4.4.3 TOF Resolution and PHA Calibration

The TOF resolution is a measure of the uncertainty in the energy analysis introduced by the TOF spectrometer. From the known relation between energy and time,

$$E = \frac{1}{2}M_1\frac{L^2}{t^2} \qquad (4.1)$$

where M_1 is the projectile mass, L is the length of the flight path and t is the flight time. The uncertainty ΔE in measuring the energy E for a pulse width Δt is given by,

$$\Delta E = M_1 L^2 \frac{\Delta t}{t^3}. \tag{4.2}$$

From equations (4.1) and (4.2), the TOF resolution is given by,

$$\frac{\Delta E}{E} = \frac{2\Delta t}{t} \tag{4.3}$$

Applying equation (4.3) to highest energies to be studied, namely, 15 keV hydrogen and 15 keV helium, it can be found that:

For hydrogen $\quad \frac{\Delta E}{E} = 0.26 \, \Delta t \quad$ % $\quad$ and $\tag{4.4a}$

for helium $\quad \frac{\Delta E}{E} = 0.13 \, \Delta t \quad$ % $\tag{4.4b}$

where Δt is in nanoseconds. For lower energies, t will be larger and consequently, for the same Δt, $\frac{\Delta E}{E}$ will be smaller.

To prevent any neutrals in the incident beam from hitting the target and act as a source of noise, the target chamber is mechanically misaligned and the x-plates in the differential chamber are used to align the ions on the target. This improves the signal to noise ratio significantly.

Before recording the TOF spectra, the PHA was calibrated to calculate the exact time per channel. An electronic circuit was built to simulate the actual scattering experiment. Figure 4.7 is a schematic of the circuit used. A pulse was fed to the TAC as a START pulse and a similar pulse goes to a delay amplifer (to give the required delay times as in the backscattering experiment), linear amplifier and a cross-over-pickoff. The output from the COP is the STOP signal to the
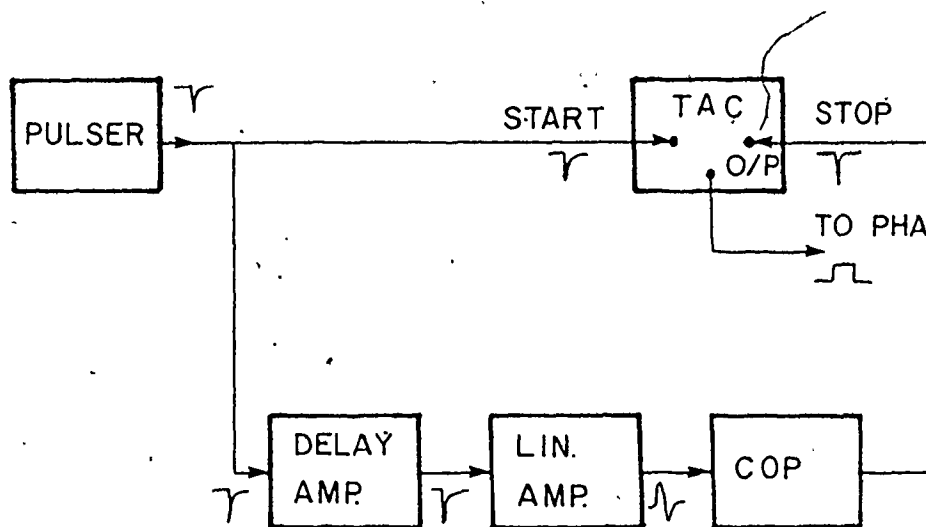
Fig. 4.7: Block diagram for PHA calibration.
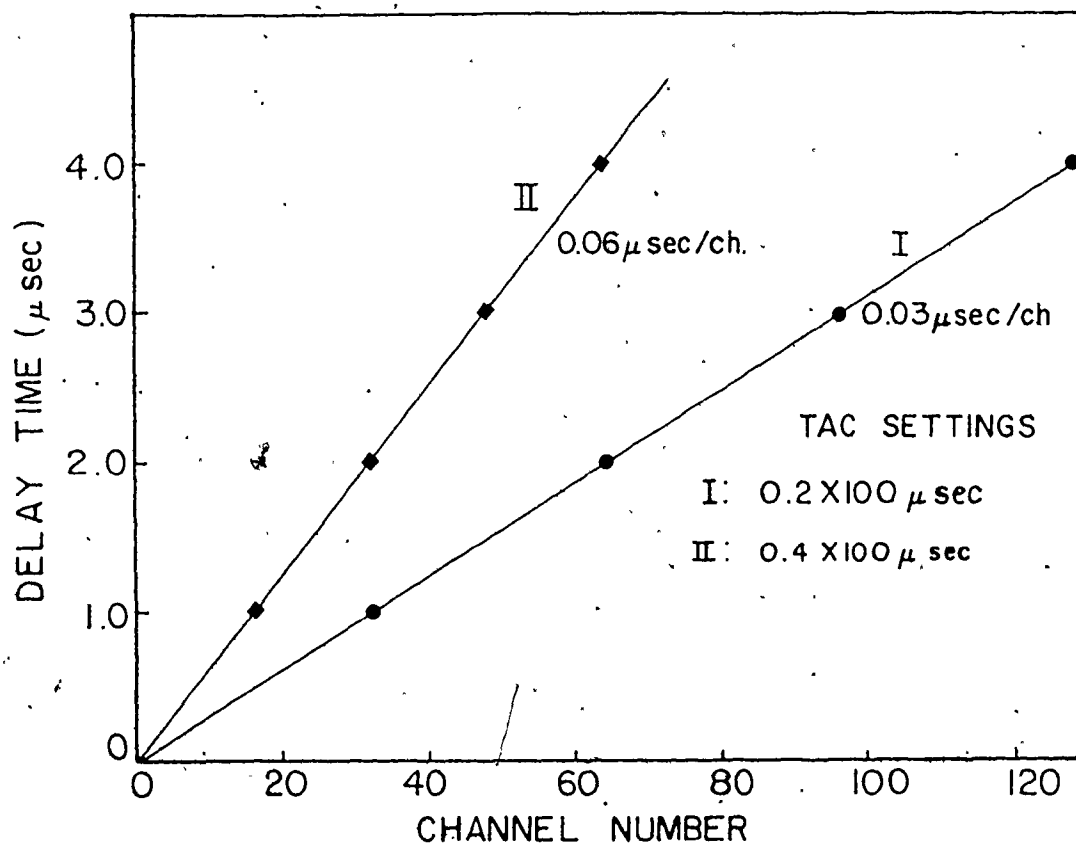
Fig. 4.8: PHA calibration curves.

TAC. The output from the TAC is fed directly as an input to the PHA. Figure 4.8 shows the calibration curves for two different TAC settings.

4.4.4 Final Remarks

The TOF technique has the following advantages over the use of the electrostatic analyzers: (1) Beam pulsing lowers the incident beam intensity, a reduction of 10^{-2} to 10^{-4} expected, and therefore lower doses will bombard the target. This will create less damage which is important in studies of composition and structure of outermost layers. (2) In this energy range, neutralization of the backscattered particles is substantial. Since both neutrals and ions are detected simultaneously, the TOF technique eliminates the special effect of neutralization on the shape of the backscattered spectra. (3) Along the time-of-flight path there is a pair of 11 cm long deflecting plates. With both plates grounded, all the backscattered particles (neutrals and ions) reach the detector and a TOF spectrum for the total particles is recorded. Applying a deflecting voltage to the plates, the ion portion of the backscattered particles is prohibited from reaching the detector and a TOF spectrum for the neutrals only is recorded. From these two spectra, the charged fractions of the backscattered particles can be calculated as will be shown in Chapter 7. Therefore, the TOF technique provides ion fraction data which is useful in understanding the neutralization mechanisms and in calibrating ESA.

On the other hand, there are some disadvantages: (1) The system is more complicated than the ESA technique, e.g. beam transport to the

target is more difficult, and (2) detection efficiency for ions and neutrals may differ at low energies (≤ 500 eV). This makes the technique useful only for energies >500 eV.

CHAPTER 5

APPLICATION OF TIME-OF-FLIGHT TECHNIQUE TO SURFACE ANALYSIS

The analysis of solid surfaces by the scattering, or generally
the interactions, of energetic ion beams is a well established technique.
To test the time-of-flight (TOF) technique, it was applied to surface
analysis. A well controlled experiment is described in this chapter;
the resolution and sensitivity of the TOF technique is deduced from
this experiment.

First a brief description of the use of ion scattering for
surface analysis will be given. For the sake of completeness, the
different energy ranges will be discussed although the main interest
in this thesis is the energy range of 5-20 keV as was mentioned in
Chapter 1.

5.1 Ion-Surface Scattering

As was mentioned in Chapter 2, an energetic ion will lose
energy upon interacting with solids in two different ways, namely,
through elastic collisions with the target atoms and inelastic
collisions through excitation and ionization of target electrons.
These processes can be used for surface analysis (40-44). The main
topic of the present work is the use of the elastically backscattered
particles (I^+, I°, I^-) for the analysis of solid surfaces.

Depending on the incident ion energy, ion scattering is capable of probing the outer surface of a solid (one or two atom layers) or a region extending 1-2 µm deep (45). Ion scattering experiments have been performed at energies which can be classified loosely as high (0.4-3 MeV), medium (4-400 keV), and low (0.1-4 keV).

5.1.1 General Principles

The ion scattering technique consists basically of bombarding a target with a monoenergetic collimated ion beam and collecting an energy spectrum of the particles backscattered through a certain scattering angle ψ, which is usually $\geq 90°$. This energy spectrum is then analyzed to give information about surface chemical composition, (45-48) surface disorder (46,49,50) and surface topography on an atomic scale (11,51,52,53,54).

In all three energy ranges, the collisions are elastic, within the energy resolution of most experimental systems. This permits simple identification of atoms at a surface by the energy spectrum of the backscattered particles through equation (2.9), which is based on conservation of kinetic energy and momentum.

$$\frac{E_1}{E_0} = \frac{M_1^2}{(M_1+M_2)^2} [\cos\psi + \left(\frac{M_2^2}{M_1^2} - \sin^2\psi\right)^{\frac{1}{2}}]^2 \qquad (2.9)$$

where E_0 and E_1 are the energies of the incident and backscattered particles, respectively. Thus, the energy scale becomes a mass scale for target atoms at the surface with higher energies indicating higher

masses.

5.1.2 High-Energy Scattering

High-energy scattering is the most quantitative ion scattering analytical technique at the present time since the physics of the scattering and energy loss mechanisms are well known. In this case the interatomic potential is the Coulomb potential and accordingly, the scattering cross section is given accurately by the Rutherford formula (55):

$$\frac{d\sigma}{d\Omega} = 1.3 \times 10^{-27} \left(\frac{Z_1 Z_2}{E}\right)^2 \left(\frac{M_1 + M_2}{M_2}\right)^2 \frac{1}{\sin^4(\theta/2)} \ cm^2/sr \qquad (5.1)$$

A typical application for high-energy scattering (known as Rutherford backscattering, RBS) will be given in section 5.2 for the characterization of the prepared target.

The RBS technique is not so satisfactory for surface analysis when the impurity is lighter than the host crystal or for thin film analysis when two of the constituents are close in mass. The use of channeling technique with RBS overcomes these problems in the case of single crystal studies; this makes RBS a very powerful tool for studying single crystals. This field is covered in detail by the book of Mayer, Erikson, and Davies (56).

High-energy ion scattering possesses the great advantage that depth profiling is obtained nondestructively without the need of sputtering or sectioning. Sputtering with MeV beams is negligible, and

there is a little evidence that helium beams produce any significant damage at the surface. This is because the energy loss is mainly electronic in the high energy range.

The detector used in high-energy scattering experiments is a solid state detector capable of detecting both neutrals and ions and therefore makes it possible to compare experimental and theoretical calculations.

5.1.3 Medium-Energy Scattering

Medium-energy ion scattering (46) has capabilities similar to those of high-energy scattering,although the maximum depth is smaller. 0.05-0.2 μm compared to $\sim$ 0.5 μm for high-energy scattering. In most scattering experiments hydrogen and helium ions are used as incident beams. In this case when the incident energy is ≥ 100 keV, the scattering yield of ions plus neutrals are given for most cases by the Rutherford formula (5.1). The scattering cross sections are larger for the medium energies than for the high energies because of the $1/E^2$ dependence, therefore the yield will be higher in this case. This advantage is offset by the pile-up problem (if two ions enter the detector within the resolving time of the electronics, then a sum pulse will result) which requires a reduction in the incident beam current when a solid state detector is used. Very good depth resolution can be obtained if an electrostatic analyzer (ESA) is used since the energy resolution is then a constant fraction, e.g. 0.01-0.02 of a rather small backscattered energy.

In this energy range, a solid state detector could be used with its ability to detect both neutrals and ions backscattered from the target. But these detectors cannot be used in the low energy regime because of the dead layer thickness. ESA with a channel electron multiplier at the end are used to overcome the problem of detecting lower energy ions with the advantage of high energy resolution. Its major disadvantage, however, is that it cannot detect neutral particles, a problem which becomes more severe as the energy becomes lower because of the larger neutralization as will be discussed later.

5.1.4 Low-Energy Scattering

Low-energy ion scattering for surface analysis was first introduced by Smith (4) . He studied scattering of noble gas ions incident at 0.5-3.0 keV on nickel and molybdenum surfaces. The surprising feature of his results was the resolution of peaks for light elements on heavy substrates without channeling; e.g. with helium beams, peaks of carbon and oxygen adsorbed on polycrystalline nickel were clearly resolved with very little of the background due to helium scattering from the nickel substrate, which would occur in high or medium-energy scattering.

This technique is a true surface technique; the energy spectra obtained with an electrostatic analyzer represent predominantly ions which have penetrated only one or two atom layers before scattering. This is comparable to the escape depth in Auger electron spectroscopy (3).

Two major problems arise in the low-energy ion scattering for surface analysis; the first is that in this energy range, the interaction is not between the bare nuclei of the target atoms but rather with the screened nuclear charge. Therefore, the Rutherford formula does not apply here. Different interatomic potentials are proposed to replace the Coulomb potential as was shown in Chapter 2. This problem prevents the quantitative analysis of collected spectra without the use of standard samples. The second problem concerns the neutralization effects which are far more pronounced here than in the medium energy range. The solid state detectors cannot be used because of the dead layer thickness. The electrostatic analyzer is only capable of analyzing backscattered ions, which is a small fraction of the total backscattered particles as will be shown in Chapter 7. Therefore, corrections for the energy spectra should be introduced to deduce the exact spectra.

On the other hand, this neutralization phenomenon makes the low energy scattering technique more interesting. The more complete neutralization of noble gas ions which penetrate beyond the first one or two atom layers, thereby reducing the background yield from deeper substrate atoms and permitting resolution of light-element peaks (4,11). The phenomenon of ion neutralization in solids will be discussed in detail in Chapter 7.

In low-energy scattering, composition depth profiles cannot be derived from a single spectrum but could be obtained only by successive sputtering and ion scattering.

In this energy range, surface damage to the substrate is more

pronounced than in the high energy range. Surface damage by 1 keV argon ion

beams on a nickel single crystal has been studied by ion scattering

and LEED (50). Both techniques detected damage after doses of $10^{15}/$

cm^2 or greater.

Finally, since low-energy ion scattering is very sensitive to

surface conditions an UHV target chamber should be used (better than

10^{-8} Torr) compared to 10^{-6} Torr in the other energy ranges.

5.2 Target Preparation and Characterization

Before recording the TOF and energy spectra of the backscattered

particles, which is the main purpose of this work, the experimental

system and the TOF technique were tested by using it for surface

analysis. A controlled surface analysis experiment was done. First

the target was prepared by evaporating a silver film on a silicon

substrate. The evaporation was made by electron beam bombardment

under high vacuum conditions (10^{-7} Torr). Before evaporation, the

silicon substrates were precleaned with acetone, hydrofluoric acid

and distilled water. To determine the thickness of the deposition

film, a digital thickness monitor (Sloan model 200) was used. This

thickness monitor uses a quartz crystal oscillator for thickness

calibration. If an alternating electric field is applied, the crystal

vibrates; the amplitude of vibration is a function of frequency and

exhibits a sharp peak (resonance) at a frequency determined by the

mechanical properties of the crystal (dimensions and elastic constants).

The frequency of operation will change if these properties are changed.

Specifically, if material (mass) is added to one of the vibrating crystal.

faces, the frequency tends to decrease. The new crystal frequency is maintained very accurately, without appreciable drift, so that it is possible to detect and measure the resultant frequency change. This change is a function of the added mass. Knowing the density of the evaporated material, the film thickness could be estimated.

Due to the difference between the bulk density and the deposited density, which is substantial for thicknesses <1000 $\overset{o}{A}$, the prepared film was calibrated again using the RBS technique. Figure 5.1 shows the energy spectrum of helium (incident energy = 1.00 MeV). To calculate the film thickness from this spectrum, the following relation is used (3),

$$\frac{C_i}{C_s} = \left(\frac{d\sigma}{d\Omega}\right)_i \left(\frac{d\Omega}{d\sigma}\right)_s \frac{N_i}{N_s}$$

(5.2)

where C_i is the number of counts in the silver peak, C_s the number of counts in one channel (i.e. a known energy interval) of the substrate spectrum, N_s number of silicon atoms corresponding to one channel and N_i is the number of silver atoms in the film.

Only a small error ($\sim 2\%$) is introduced if the ratio of the cross sections is simply taken to be Z_i^2/Z_s^2 (3). Therefore equation (5.2) becomes,

$$\frac{C_i}{C_s} = \frac{Z_i^2}{Z_s^2} \frac{N_i}{N_s}$$

(5.3)

Taking the stopping power for helium in silicon along the ingoing and

I MeV HELIUM ON (Ag/Si)

(3.73 keV/channel)

NUMBER OF BACKSCATTERED PARTICLES (XIO^{-2})

CHANNEL NUMBER
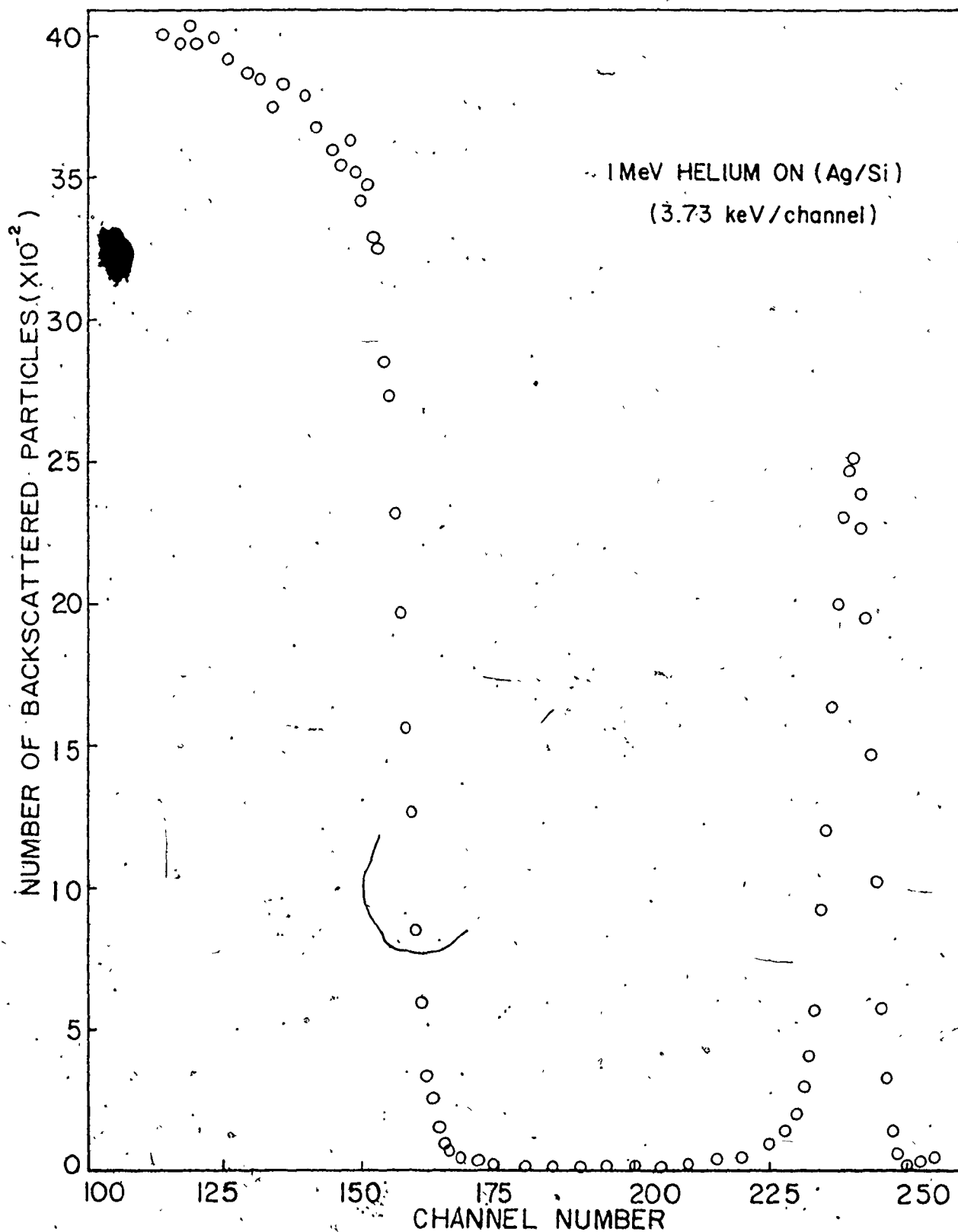
Fig. 5.1: Energy distribution of backscattered helium particles from (Ag/Si) target using RBS.

outgoing trajectories as 115.2×10^{-15} eV/atom and knowing the energy
interval per channel (from the RBS spectrum), the film thickness was
found to be about 15 monolayers (the original thickness using the
quartz oscillator was about 12 monolayers).

To check the film continuity, an Auger spectrum was taken from
an arbitrary point on the sample. Figure 5.2a shows this spectrum for
the as received target. As can be seen from this figure, the silver
signal is the main signal indicating that silver is covering the
analyzed spot (electron beam size ~25 microns at 3 keV.). Using 5 keV
argon sputter gun (dose ~10^{16}/cm^2), the silver film was sputtered and
the spectrum in figure 5.2b was obtained. Repeating these steps at
another point on the surface gave exactly the same shape for the Auger
spectra. This experiment proved that the silver film could be, fairly
accurately, considered continuous.

5.3 Surface Analysis by TOF

The time-of-flight technique (TOF) can be used in a manner
similar to Rutherford backscattering (RBS) or ion surface scattering
(ISS) to analyze the composition of solid surfaces (57). It is similar
to RBS in that all neutrals and ions are detected. Consequently,
much more data per unit dose is recorded for the same detector solid
angle than with ISS. However, it should be noted that the neutral yield
is not as sensitive to surface conditions as with ISS.

TOF was used to analyze a target similar to that described in
section 5.2. Hydrogen and helium ions were used in the analysis. The
incident energy was 10 keV and the ion beams hit the target normally.
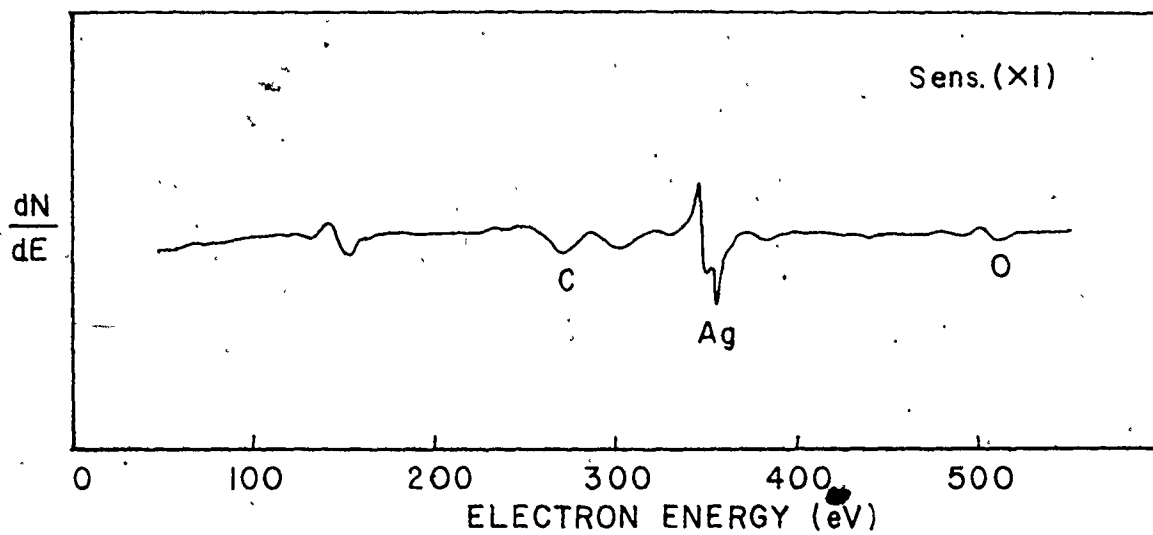
Fig. 5.2a: Auger spectrum for the (Ag/Si) target.
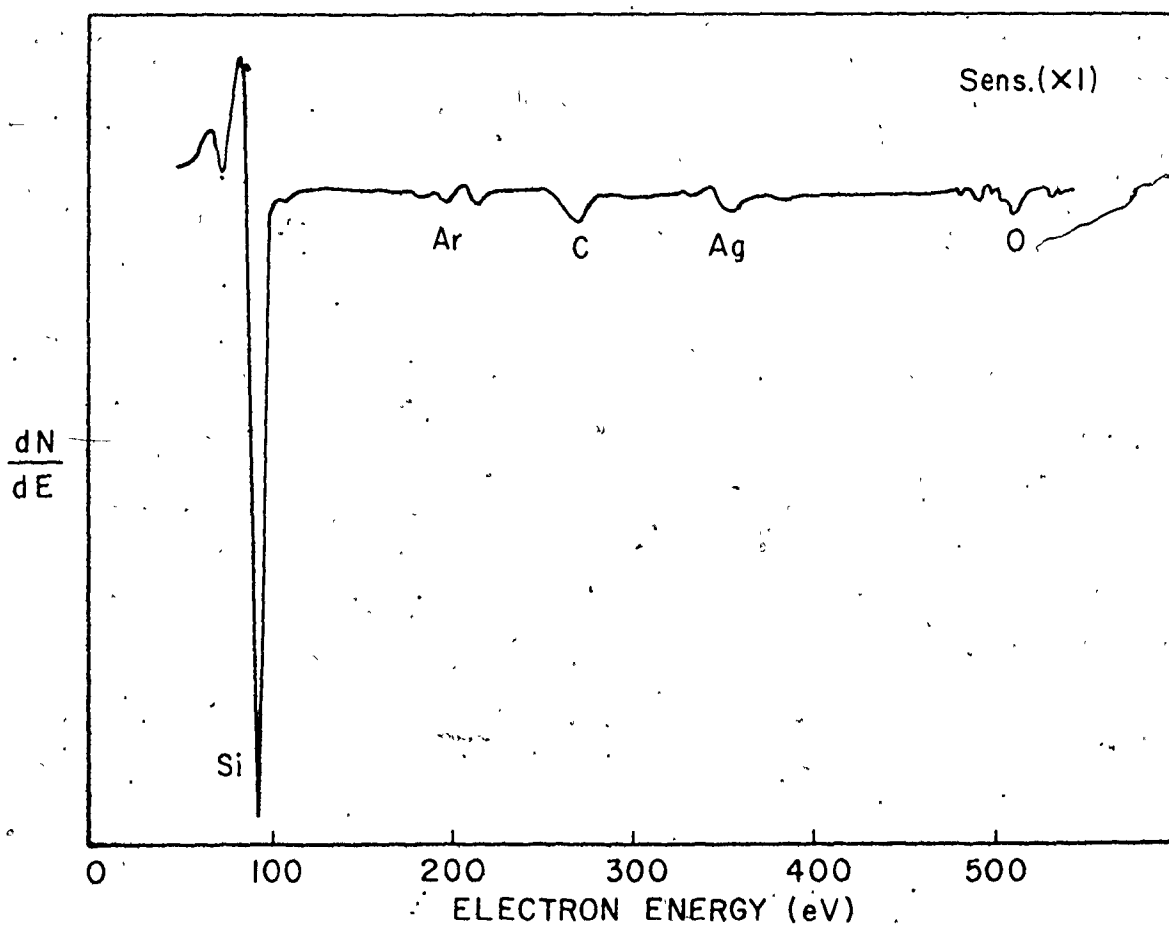
Fig. 5.2b: Auger spectrum for the same target after cleaning.

The scattering angle was fixed at 135°. In the case of hydrogen, the time per channel was ∿31 nanoseconds. The helium spectra were collected using a 62.5 nanoseconds per channel.

Figures 5.3a and 5.4a show the time-of-flight spectra for 10 keV hydrogen and helium backscattered from Ag/Si target respectively. As can be seen from these spectra, each shows a sharp peak corresponding to scattering from the silver film and background (or noise) denotes scattering from the silicon substrate.

The time-of-flight spectra were transformed to energy spectra as will be discussed in the next chapter. Figure 5.3b and 5.4b show the deduced energy spectra for hydrogen and helium respectively. In calculating the energy spectra, the peak channel was considered as a single scattering between the incident ion and a silver atom at 135°. Using equation (2.9), the energy corresponding to the peak channel was calculated and consequently the time-of-flight. This was used to determine the zero time on the multichannel analyzer which is very important in any TOF measurement.

The peak due to scattering from silver is much sharper in the case of helium than hydrogen as shown in Figure 5.5. The same figure shows that the background is suppressed in the helium case while it is higher for hydrogen scattering. This proves the better resolution of helium over hydrogen as is known in RBS.

Comparing the energy spectra in figures 5.3b and 5.4b, it is clear that the helium spectrum shows a hump corresponding to scattering from silver while the hydrogen spectrum shows no humps. This should
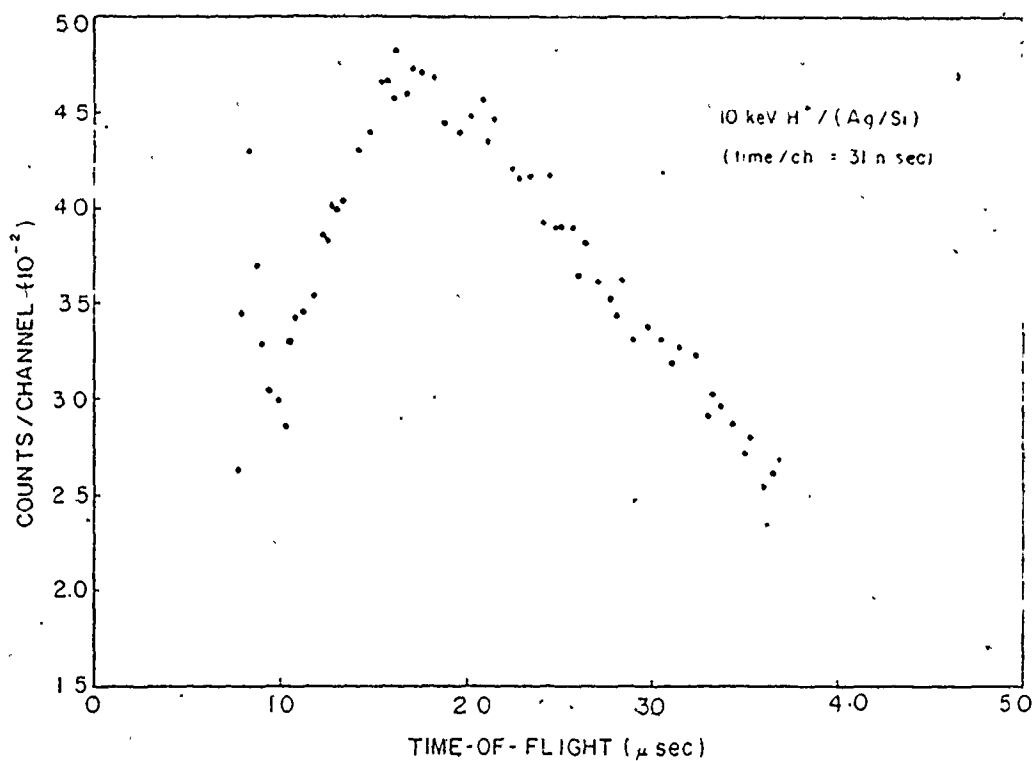
Fig. 5.3a: Time-of-flight spectrum for 10 keV H⁺/(Ag/Si).
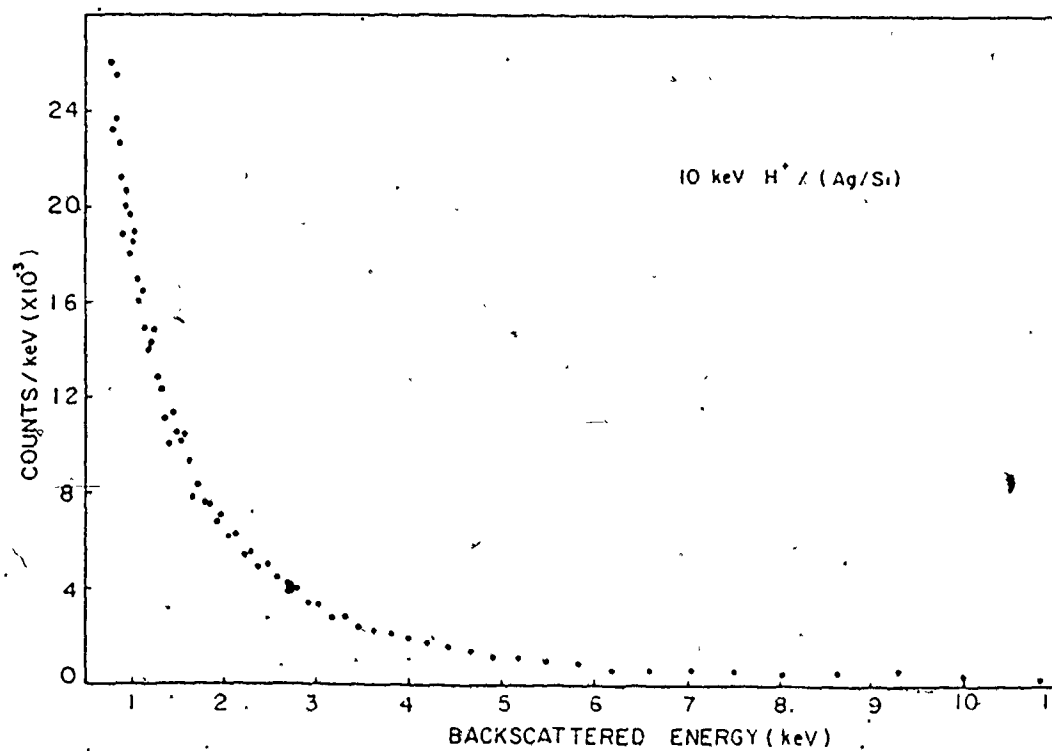
Fig. 5.3b: Energy distribution of backscattered particles.
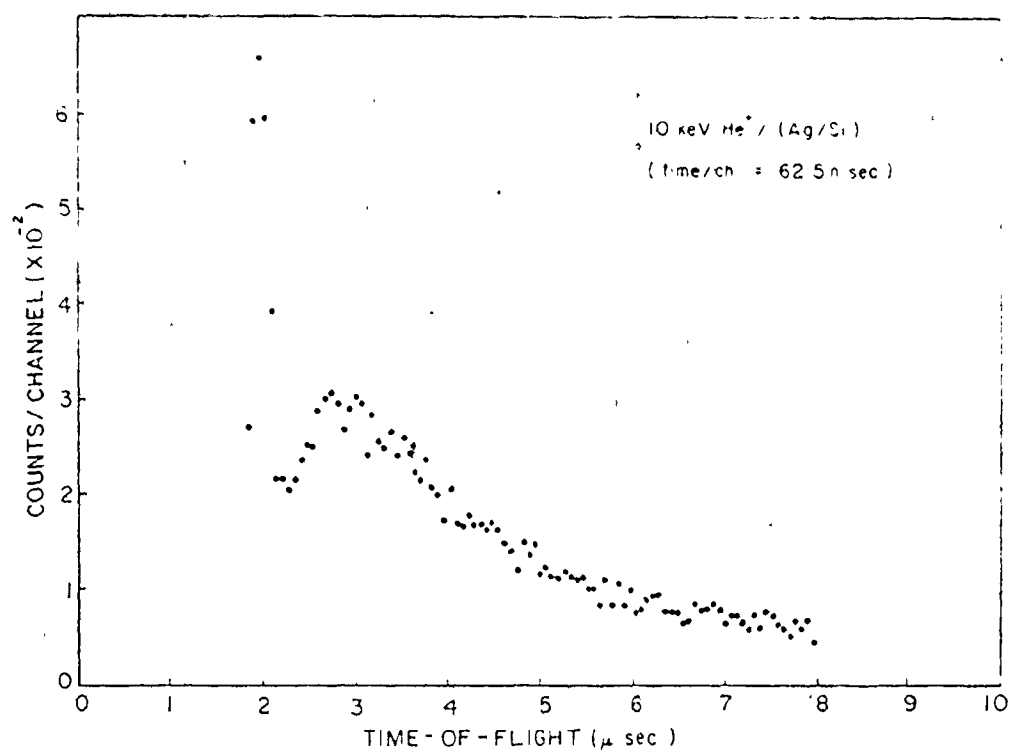
Fig. 5.4a: Time-of-flight spectrum for 10 keV He$^+$/(Ag/Si).
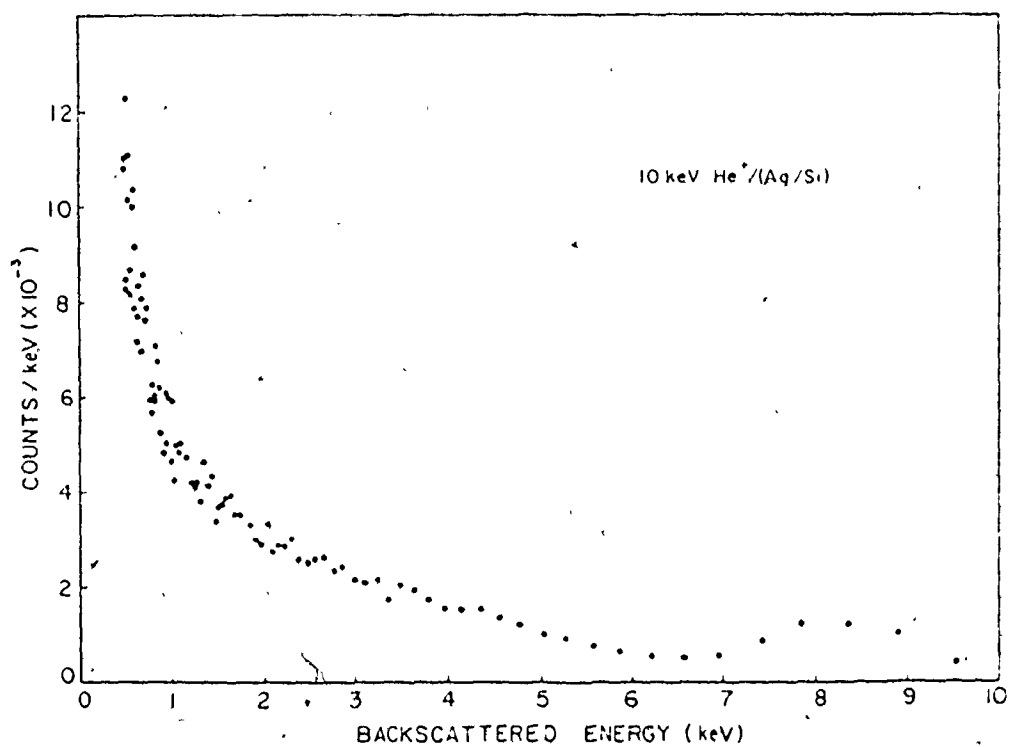
Fig. 5.4b: Energy distribution of backscattered particles.

be expected because in the helium case the energy of the backscattered
helium particle (in a single collision) from silver is 8.8 keV and
from silicon is 6.1 keV, while for hydrogen the energies are 9.7 keV
and 8.9 keV respectively. Therefore, the hump is shadowed by the
scattering from the silicon substrate due to the smaller difference in
energies. In addition, the fact that helium has a larger elastic
cross section than hydrogen increases the probability of the helium
ion being scattered from the silver film more efficiently than does
the hydrogen. This is why helium has a better resolution than hydrogen.

5.4 Resolution and Sensitivity of TOF

Important considerations for any ion scattering technique are
energy resolution and sensitivity. For the TOF technique, the energy
resolution depends on the system time resolution (Δt) and the time-of-
flight (t): $\Delta E/E \simeq 2\Delta t/t$ as was shown in Chapter 4. For a fixed Δt,
the resolution varies inversely with the time-of-flight tube length.
However, a long tube length reduces the solid angle ($\Delta\Omega$) for a detector
with a fixed diameter ($\Delta\Omega \alpha$ $1/L^2$). Thus high TOF resolution can be
attained only be reducing the data accumulation rate. This is an
important limiting factor for high energy-resolution studies (58). As
was shown in Chapter 4, for 10 keV helium ions the TOF energy reso-
lution is approximately 5%. Beside the TOF energy resolution, there
is the electronic stopping broadening of at least 5% (59). These
figures give an overall energy resolution of $\sim$10% which is consistent
with the broadening of the silver peak in Figure 5.3b.
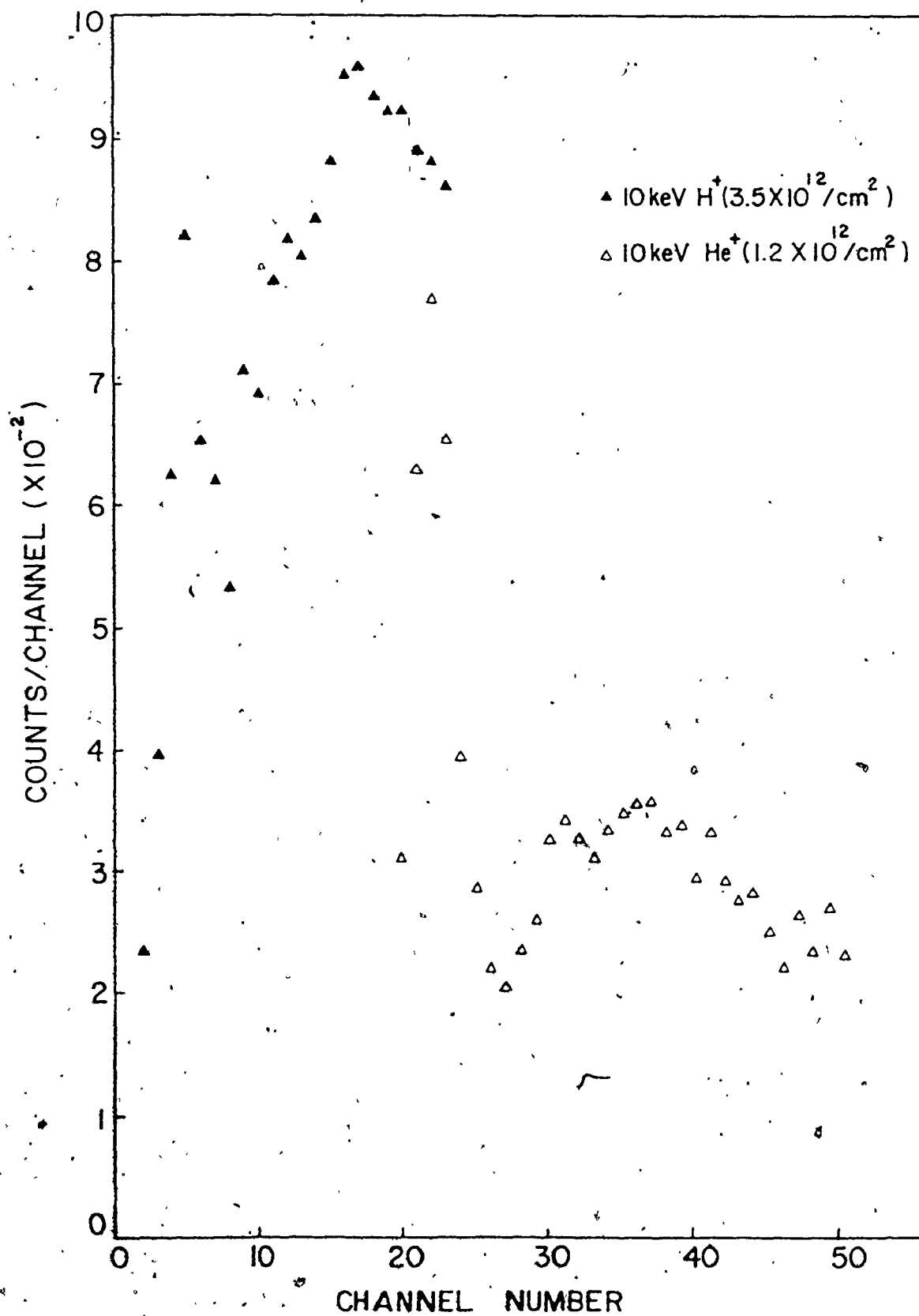
Fig. 5.5: Comparison between H⁺ and He⁺ TOF spectra.

The sensitivity of the TOF technique depends on three main effects: (1) system resolution if the peak is near the multiple collision time edge, as shown by the difference between helium and hydrogen scattering in the previous section, (2) neutrals in the incident beam, and (3) fast sputtered particles. The second noise source, the presence of neutrals in the beam, was reduced by producing a low vacuum (10^{-8} Torr) in the differential pumping section. In addition, this section is misaligned mechanically to prevent the neutrals from going directly to the scattering chamber, as was described in Chapter 4. The third noise source, the noise contribution from fast sputtered particles in the low energy (long time) part of the scattered spectrum, can be reduced by lowering the pulse repetition frequency. In this experiment, the repetition frequency was 23 kHz.

In order to estimate the sensitivity of TOF technique for surface analysis, the silver film was alternately sputtered at full beam and then a TOF spectrum was recorded with the pulser at a much reduced (10^{-3}) beam current. Figure 5.6a shows the TOF spectrum for 10 keV helium ions incident on a new (30 Å) target, while figure 5.6b shows a typical spectrum after the target has been sputtered using 1.1×10^{16} He$^+$/cm^2 (10 keV) and 2×10^{14} N$^+$/cm^2 (7 keV) successively. By further sputtering and then extrapolating the detected signal, the sensitivity is postulated to be better than 1/20 of a monolayer for 10 keV helium scattered from the silver film.

It should be noted that the TOF technique shows a poor energy resolution for surface analysis compared to ISS; but one can use the
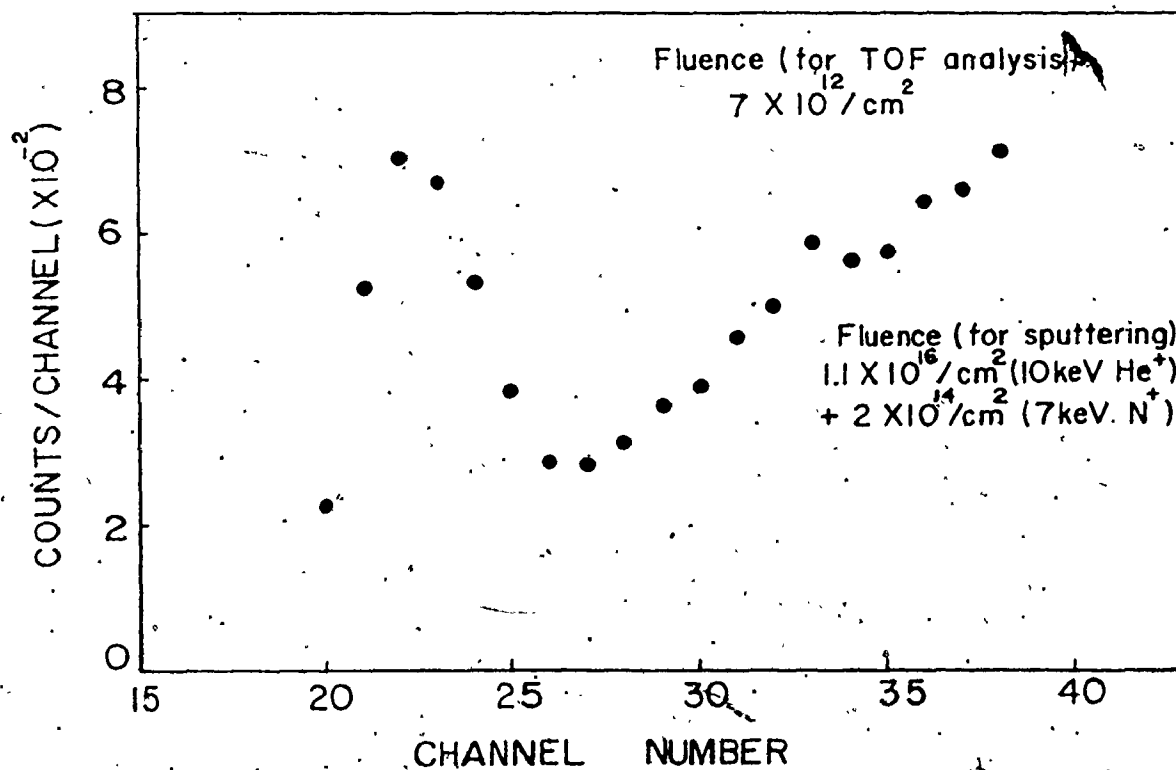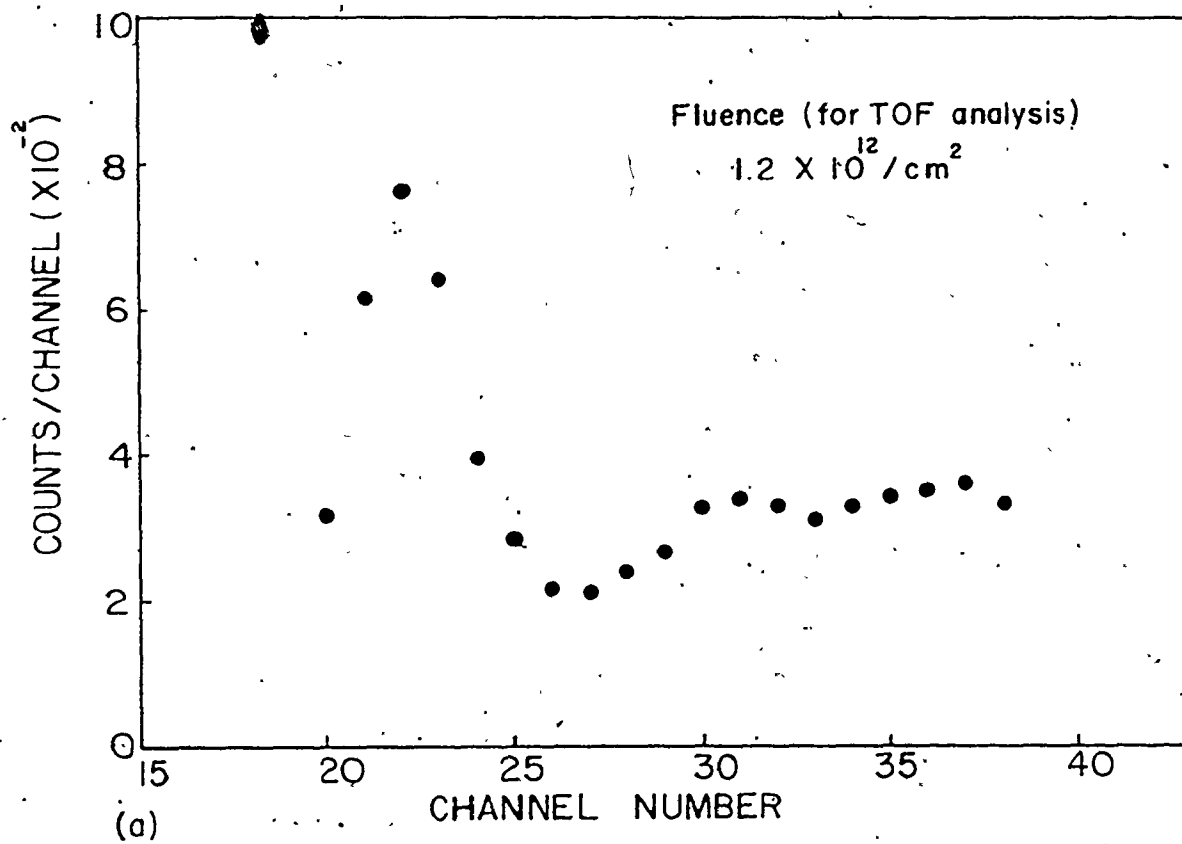
Fig. 5.6: TOF spectra for 10 keV He$^+$/(Aa/Si)
(a) target as received, (b) after sputtering with He$^+$ and N$^+$.

TOF spectra itself, since it shows very sharp peaks, to analyze surfaces. In this case it is not necessary to obtain the energy spectra from the recorded TOF spectra.

CHAPTER 6

TIME-OF-FLIGHT AND ENERGY SPECTRA

6.1 Introduction

As was indicated in Chapter 1, the energy distribution, angular distribution and charge state of backscattered light ions from solid surfaces are of importance for the evaluation of the interaction of a hot plasma with the surrounding walls. The energy range up to 20 keV is of special interest since this corresponds to the temperature in a D-T fusion reactor. The energy distribution is also important for surface anlaysis as was seen in the previous chapter.

Most of the work that has been done in this energy range uses the electrostatic analyzers (ESA). With the problems involved with the use of ESA, concerning the neutralization of backscattered particles, a technique had to be developed to measure both neutrals and ions simultaneously. Chicherov (6) recorded neutral spectra for argon ($E_0 = 16$ keV) scattered from polycrystalline gold by "stripping" or re-ionizing the scattered argon neutrals in helium or hydrogen gas and then analyzing the resulting argon ions using an electrostatic analyzer. Behrisch et. al. (60), Meischner and Verbeek (61), Eckstein et. al. (62) and Verbeek (35) used the stripping technique to study the scattering of hydrogen from different targets in the energy range 3-15 keV. They used nitrogen gas at a pressure of 2×10^{-3} Torr in the stripping cell to re-ionize the backscattered particles. The

accuracy of this stripping technique depends mainly on the calibration of the stripping cell. Extrapolation of higher energy neutralization data to lower energies is not accurate. The relative errors are greatest at low energies, which make the largest contribution to the backscattering intensity (35).

The second technique used to detect both neutrals and ions in the low energy range is the time-of-flight technique (TOF). Time-of-flight methods have been previously used for sputtered particles (63). Buck et. al. (5,58,64) used this technique to study the scattering of noble gases (He, Ne and Ar) from solids.

In this work, the time-of-flight technique (described in Chapter 4) was applied to study the scattering of hydrogen and helium ions in the energy range 5-15 keV from silicon. The TOF and energy spectra are discussed in the following sections. In the next chapter the application of the time-of-flight technique to the measurements of the charge fractions of the backscattered particles will be considered.

6.2 Target Characterization

Silicon targets were prepared from polished wafers (p-type) the surface of which was a (111) plane. The target was first cleaned with acetone, etched with hydrofluoric acid and rinsed in distilled water. Inside the target chamber, it was cleaned further by bombardment with a 5 keV neon beam (dose $\sim 10^{16}/cm^2$) before each day's experiment.

A similar target was analyzed using the "Auger Electron Spectroscopy" (AES) technique. The Auger spectra of this target are
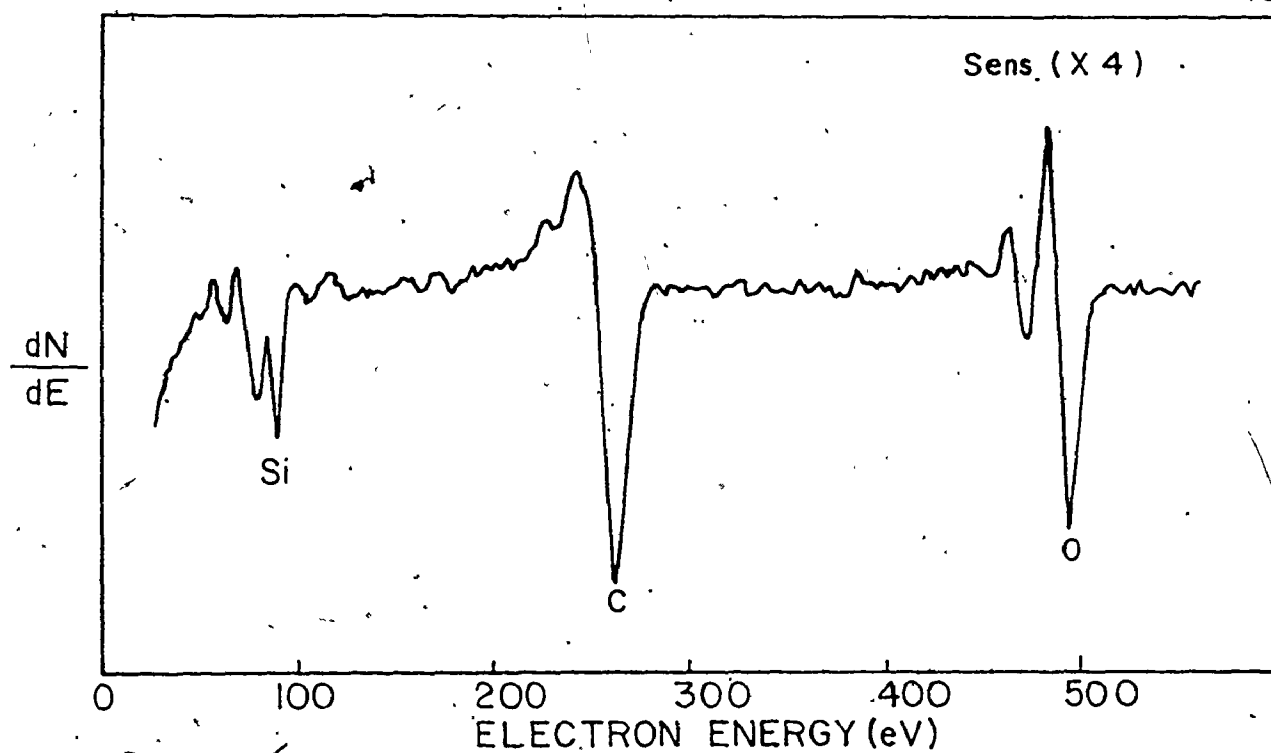
Fig. 6.1: Auger spectrum for Si target (as received).
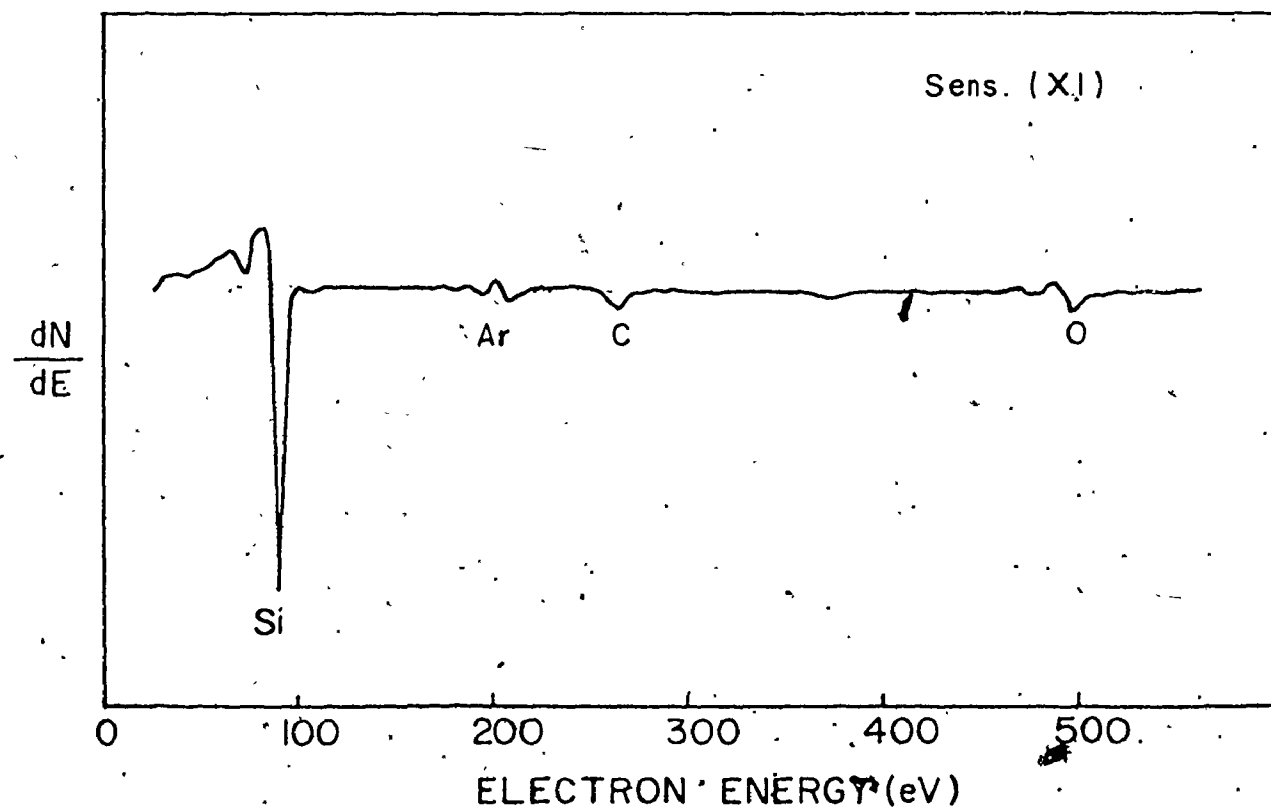
Fig. 6.2: Same target after $5 \times 10^{15}/cm^2$ Ar$^+$ sputtering.

Sens.(X1)

$\frac{dN}{dE}$

Ar

C

O

Si

ELECTRON ENERGY (eV)
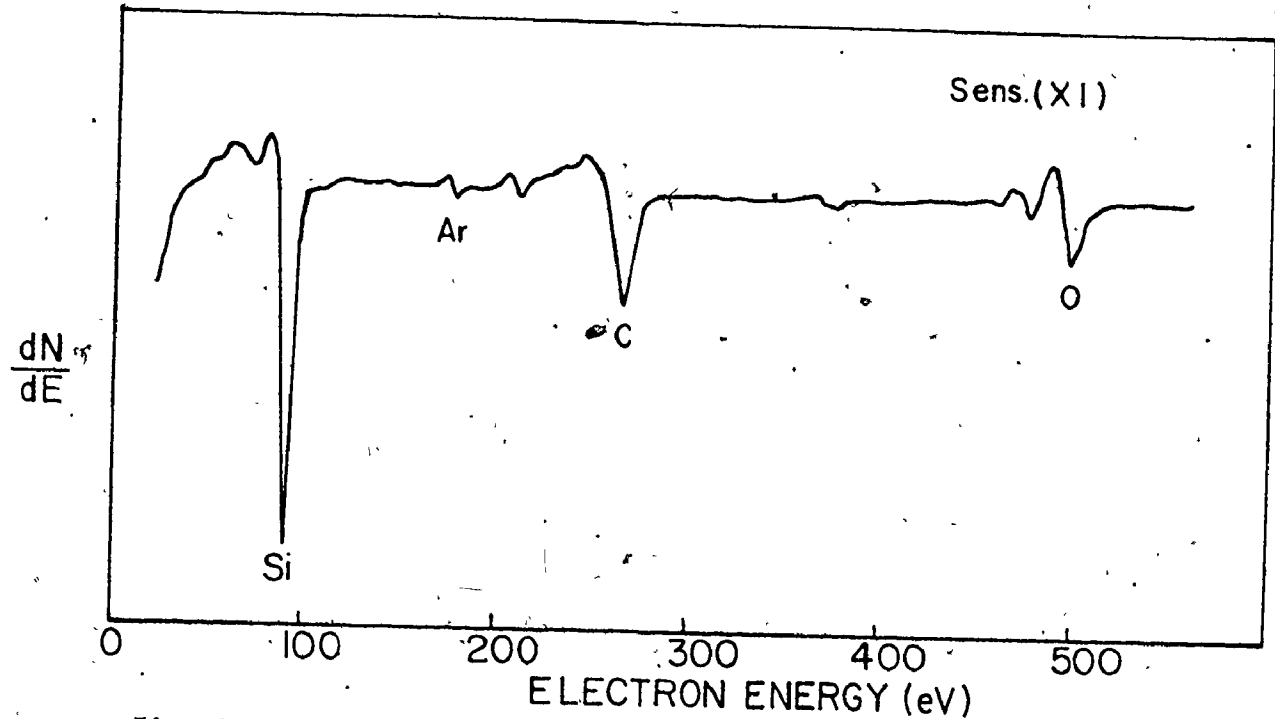
Fig. 6.3: Same target after 18 hrs - pressure 2 x 10^{-8} Torr

Sens. (X1)

$\frac{dN}{dE}$

Ar

C

O

Si

ELECTRON ENERGY (eV)

Fig. 6.4: Sam
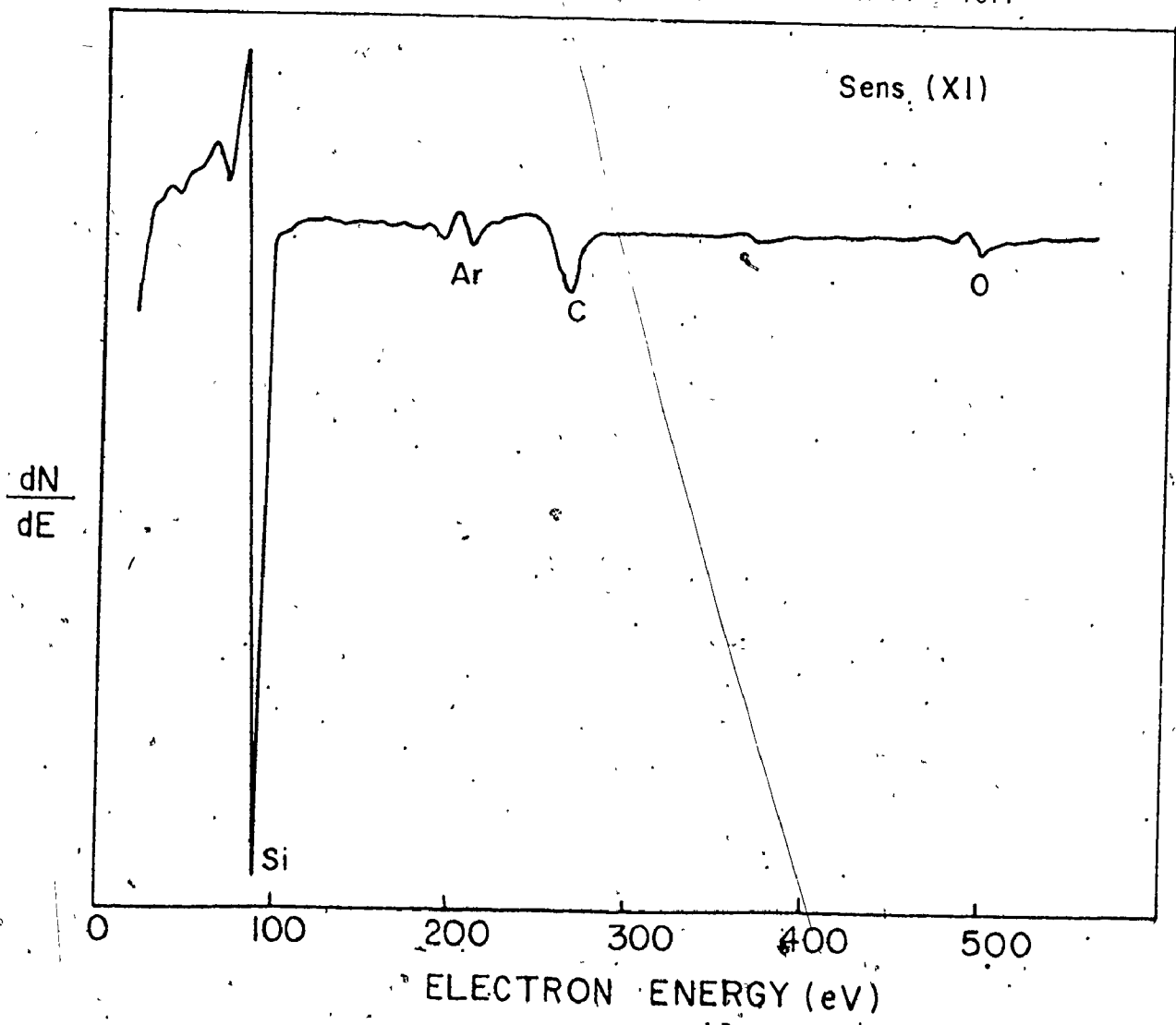
shown in figures 6.1 to 6.4. Figure 6.1 shows the spectrum for the chemically cleaned target; as can be seen the major contaminants are carbon and oxygen covering the silicon surface. A 5 keV argon sputter ion gun was then used to clean the surface (fluence $\sim 5 \times 10^{15}/cm^2$) and the sputter clean surface is shown in figure 6.2. It could be easily noticed that carbon and oxygen are reduced to a great extent and the silicon signal has increased. Figure 6.3 shows the Auger spectrum for the same target after being left in the system for 18 hours; the pressure was 2×10^{-8} Torr. As can be seen from this spectrum, the carbon and oxygen signals started to appear again indicating the deposition of these contaminants on the surface. The surface was cleaned again with argon (fluence $\sim 10^{15}/cm^2$) and the new spectrum is shown in figure 6.4. These carbon and oxygen layers do not affect the backscattered spectra appreciably, but they drastically affect the charge states of the backscattered particles as will be seen later.

6.3 Time-of-Flight Spectra

All the TOF measurements were performed for normal incidence and fixed scattering angle of 135°. The beam chopping pulse width was chosen at 30 nanosecond, and pulse amplitude of approximately 65 volts. The pulse repetition frequency was 25 kHz, therefore the actual beam hitting the target was approximately 0.8×10^{-3} of the full beam from the ion source. Typically, the pulsed ion beams used ranged from 0.05 to 0.15 nA. The TOF resolution using 30 nanosecond pulses is about 7% and 4% for 15 keV hydrogen and helium ions respectively.

5 keV Hydrogen on Silicon
(Time/ch. = 62.5 n sec.)
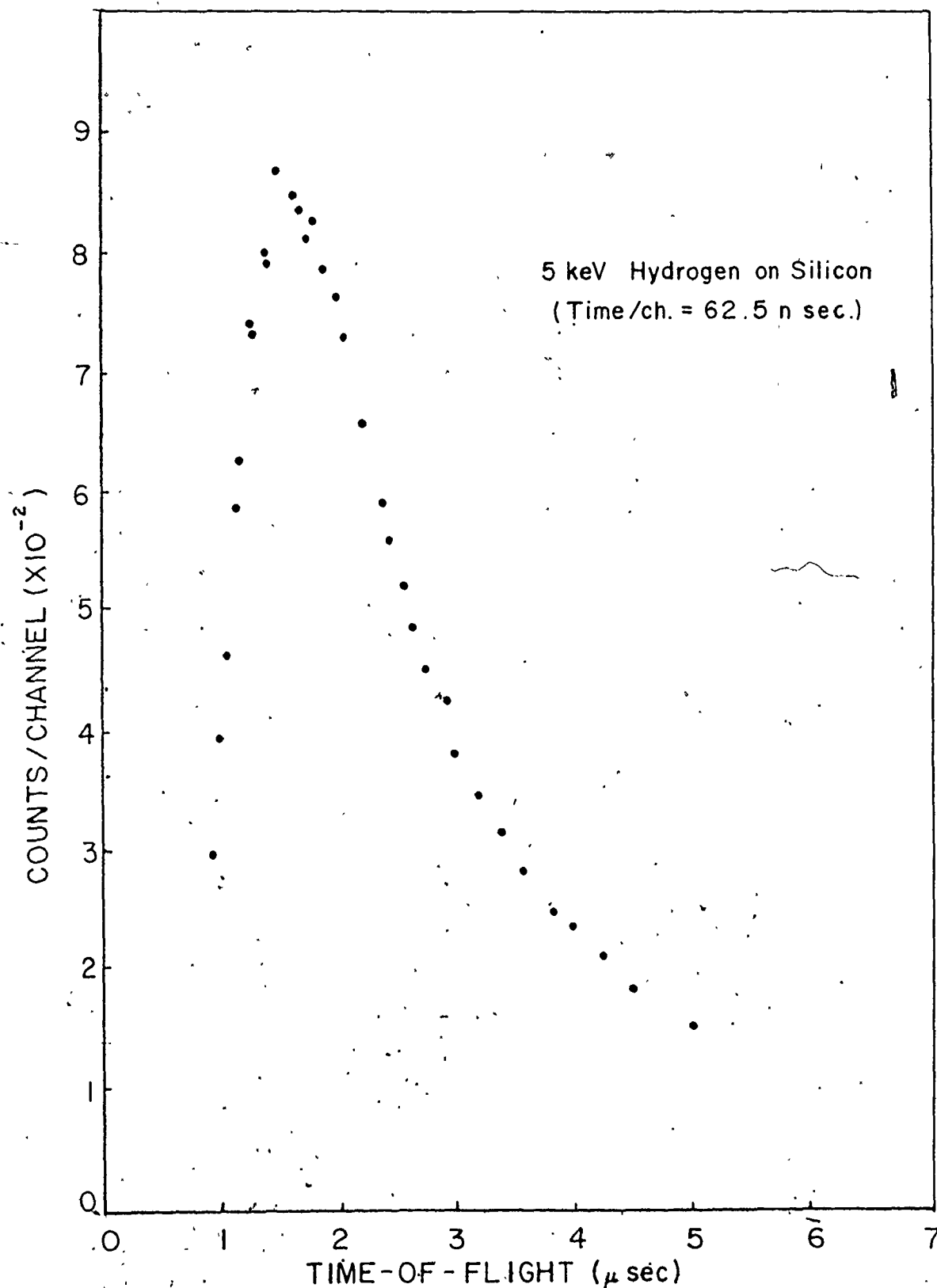
Fig. 6.5: Time-of-flight spectrum for 5 keV H$^+$ backscattered from silicon.

A typical TOF spectrum is shown in figure 6.5. This is for
5 keV hydrogen ions incident on the silicon target. The target was
aligned near the <111> direction but no channeling effects were noticed
in the analysis; this was verified experimentally as will be shown in
a later section. In these measurements, the time per channel was 62.5
nanoseconds.

The zero-time channel was determined using the single scattering
peak from the silver/silicon targets (spectra shown in Chapter 5), i.e.
the time corresponding to peak channel is known from the collision
kinetics and using the 62.5 nanosecond per channel, the zero-time channel
was determined.

For all cases studied, there were some backscattered particles
which took shorter times than those corresponding to single scattering
events at the surface. The lower the energy and the heavier the ion,
the larger is the number of such high energy particles. These particles
had encountered double or triple scatterings at the surface leading
to a total combined deflection equivalent to 135° scattering. Kine-
matically, they should have higher energies than those which encounter
a single 135° scattering. This is the reason that they took shorter
times to reach the detector.

In all these measurements, the ratio between the peak count
and the random background was better than 100:1, and the background
was subtracted from the TOF spectra before transforming them to
energy spectra.

In case of heavier ions, such as neon, one would expect to
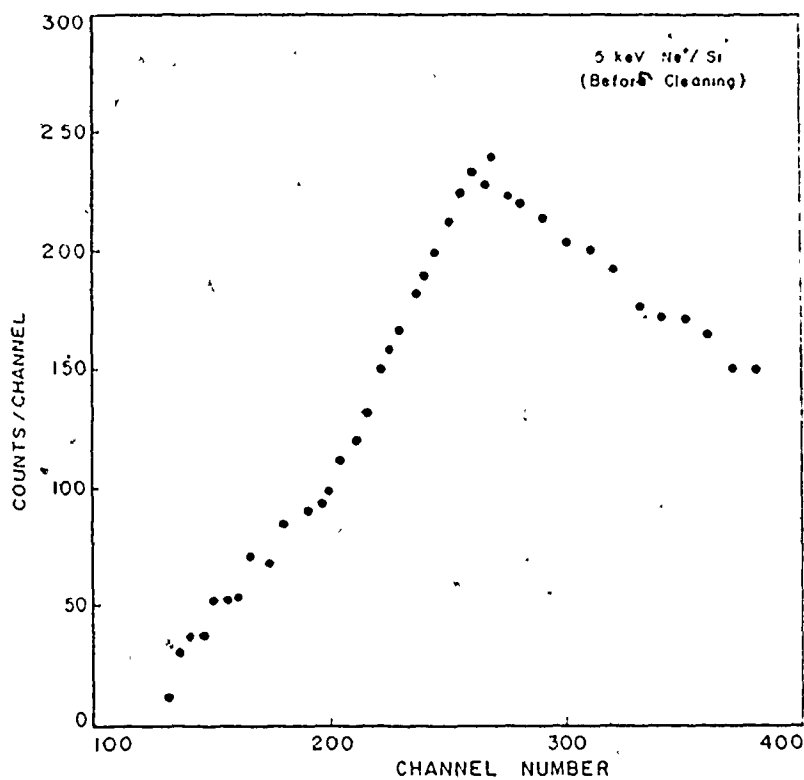
Fig. 6.6: Time-of-flight spectrum for 5 keV Ne$^+$/Si (target as received).
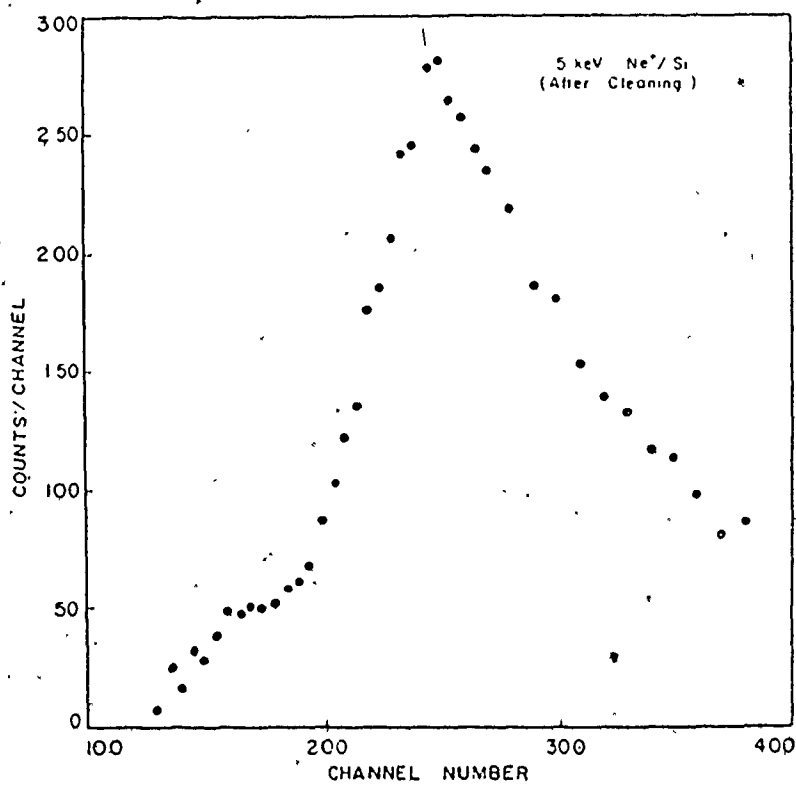
Fig. 6.7: Time-of-flight spectrum for 5 keV Ne$^+$/Si (After Ne$^+$ Cleaning).

have more scattering from the surface due to the higher scattering
cross sections.. This effect was not observed experimentally. TOF
spectra for 5 keV neon ions were recorded using 170 nanosecond pulses
(because of the transit time limitation across the pulsing plates)
at a repetition rate of only 7 kHz. Figures 6.6 and 6.7 show the TOF
spectra for a practical and cleaned target respectively. By examining
these spectra, the following factors could account for the shape
observed: a large number of sputtered particles and multiple scattering.
The fast sputtering is indicated by the hump at the left of each
spectrum. These particles are believed to be mainly carbon and oxygen
as can be seen by comparing the two spectra. For the practical target,
the contribution is much larger than the case of a clean target. This
indicates that cleaning the target (by neon bombardment) removes the
carbon and oxygen (not completely in this case) and improves the TOF
spectra obtained. Also, since the incident ion will lose about 96% E_0
for neon in a single scattering with a silicon atom at a scattering
angle 135°, a 5 keV particle which has experienced a single scattering
event will reach the detector with an energy of only 200 eV. Hence
high energy neon must be multiply scattered.

6.4 Energy Spectra.

The energy distributions for the backscattered particles (neutrals and ions) are calculated from the TOF spectra by transforming the time scale into energy scale and the counts per time interval into counts per energy interval. This is done as follows:

The relation between time and energy is given by

$$E = \frac{1}{2} M_1 L^2/t^2$$

where M_1 is the projectile mass, L is the length of the time-of-flight path and t is the time of flight. In the present experiment; L = 128 cm and $M_1 = 1.66 \times 10^{-24}$ g for hydrogen and $4(1.66 \times 10^{-24})$ g for helium. Using this equation, the average energy corresponding to each channel is calculated and consequently ΔE per channel is determined $(\Delta E_i = E_{i+1} - E_i)$.

The counts per time interval is transformed into counts per keV using the following relation

$$N_{E_i} = N_t \, \Delta t/\Delta E_i \qquad \text{counts/keV}$$

where N_t is the counts per time interval Δt(62.5 μsec), ΔE_i is the energy interval in keV.

Applying the above relations to the time and counts in each channel in the TOF spectra gives the required energy spectra (65).

The channeltron efficiency for detecting backscattered particles is very low at low energies. Therefore, the energy spectra deduced from the recorded TOF spectra should be corrected to account for the detector efficiency. Using the channeltron efficiency curves mentioned
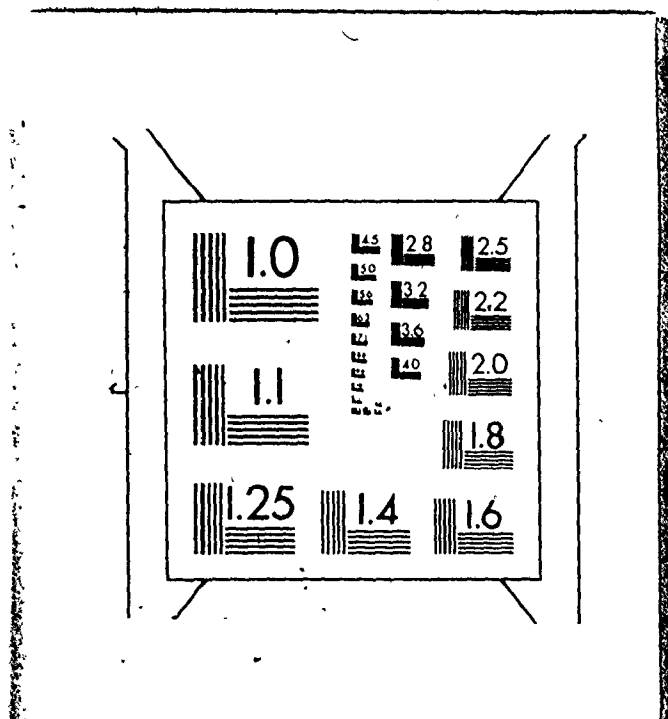
in Chapter 4, the corrected spectra were determined using a special computer program (Appendix D). The channeltron efficiency curves include some uncertainty for energies lower than 500 eV. That is the reason the energy spectra were terminated at 500 eV. In these corrections, it was assumed that the detection efficiencies were the same for both charged and neutral particles for energies over 500 eV (kinetic ejection regime).

The energy spectra for the backscattered particles, deduced from the recorded TOF spectra, are shown in figures 6.8 to 6.10 for 5, 10 and 15 keV hydrogen and the helium spectra are shown in figures 6.11 to 6.13 for the same energies respectively. All these spectra include the correction for the channeltron efficiency. To compare the experimental energy spectra with the computer simulation spectra quantitatively, the latter were normalized to the same number of incident particles determined from the TOF experiments. Assuming the energy spectra at 135° to be the same as the total spectra, i.e. for all scattering angles, which are determined by the Monte-Carlo code; and considering the solid angle the detector makes ($\sim4.3 \times 10^{-6}$ sr.). The computer simulation results are shown on the same energy spectra deduced from the TOF measurements. As can be seen from this comparison, good quantitative agreement was found. In the case for 5 keV hydrogen the experimental values were lower than the Monte-Carlo calculations. This is believed to be due to the uncertainty in the theoretical values of the elastic cross section. As can be seen from these energy spectra, no surface peaks were found. It was found that
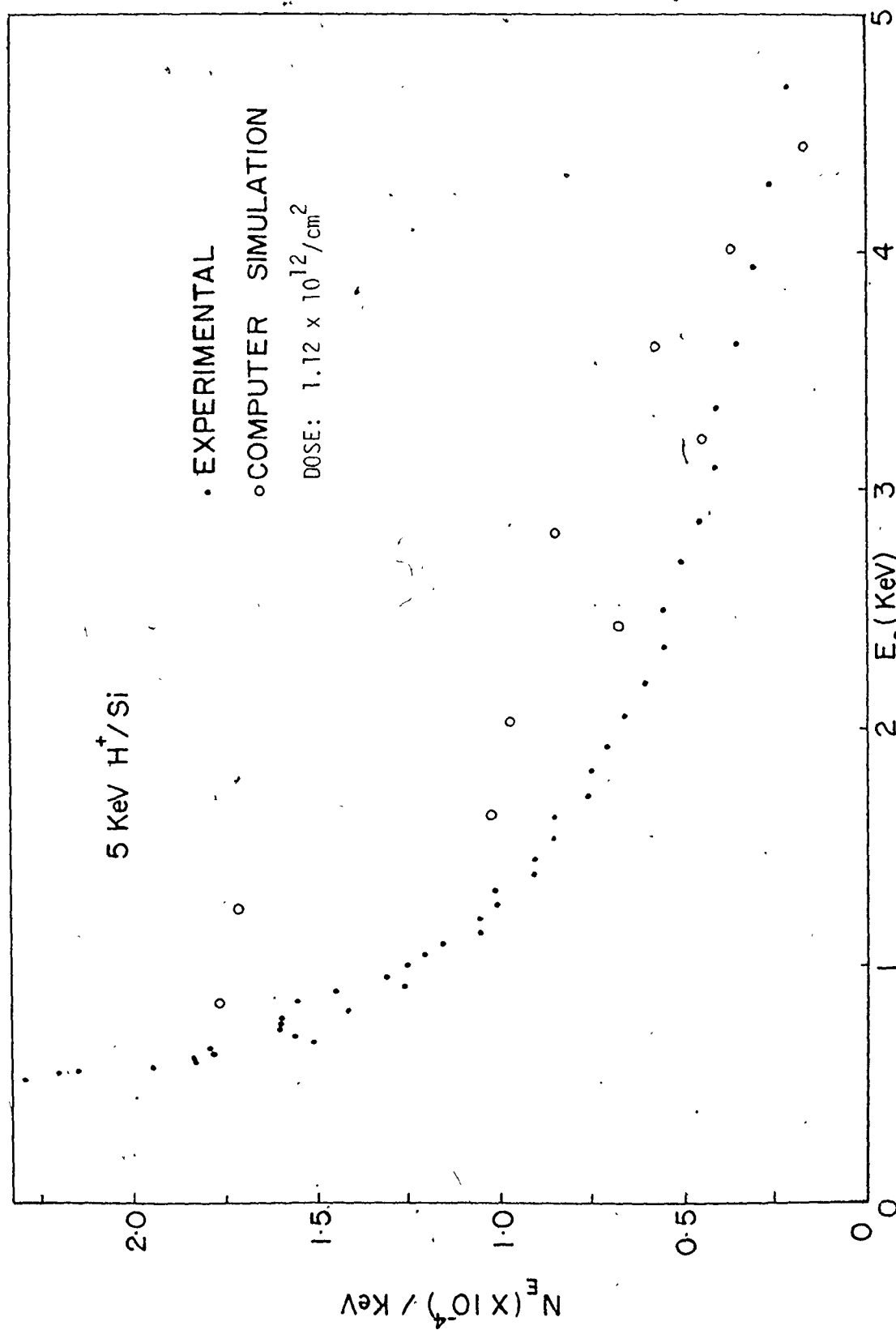
Fig. 6.8: Energy distribution of backscattered particles for 5 keV H⁺/Si.

Fig. 6.9: Energy distribution of backscattered particles for 10 keV H⁺/Si.

The plot shows:
- Title: 10 KeV H^+/Si
- Legend: • EXPERIMENTAL, o COMPUTER SIMULATION
- DOSE: $3.35 \times 10^{12}/cm^2$
- Y-axis: $N_E(\times 10^4) / KeV$
- X-axis: E_s (KeV)
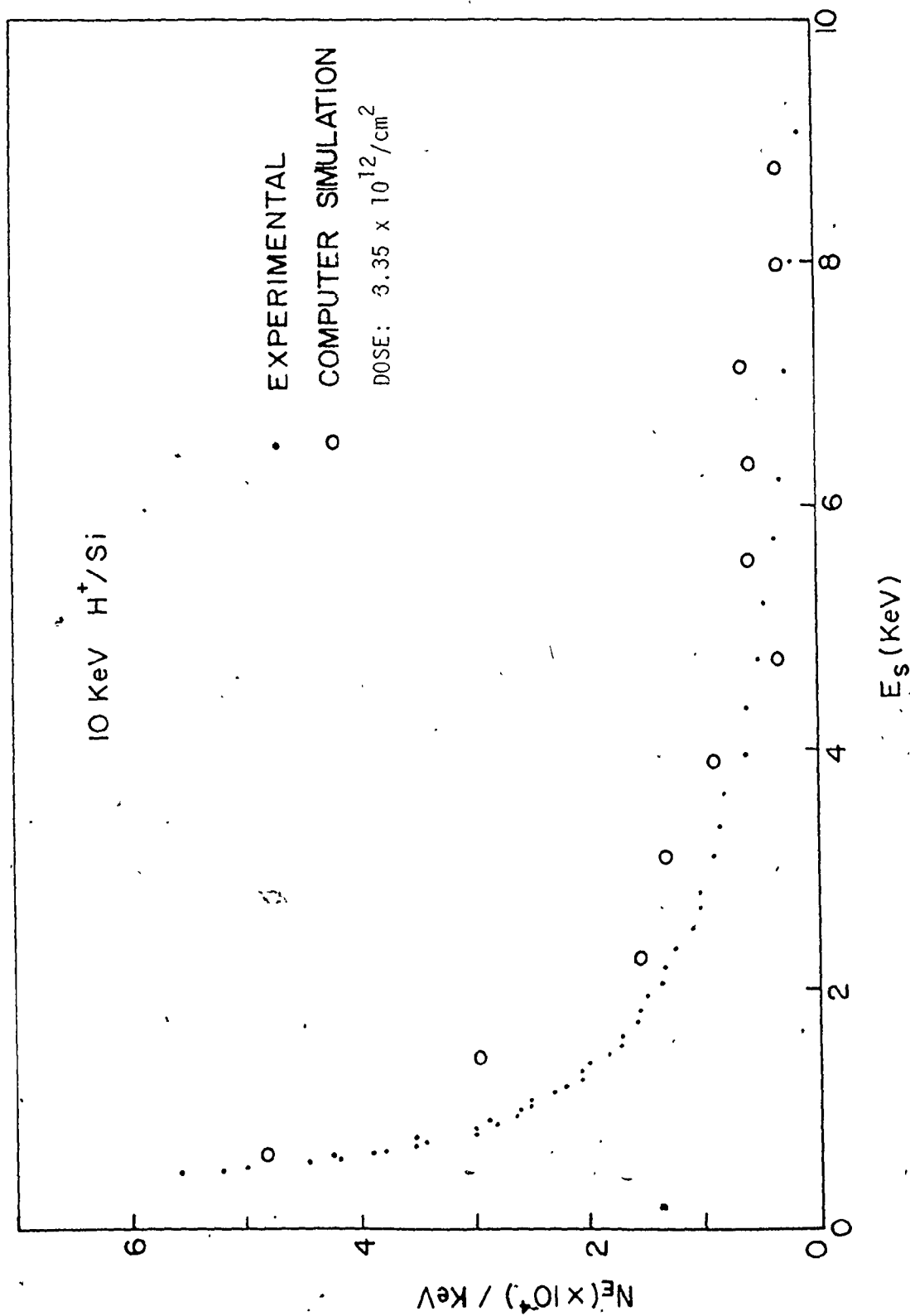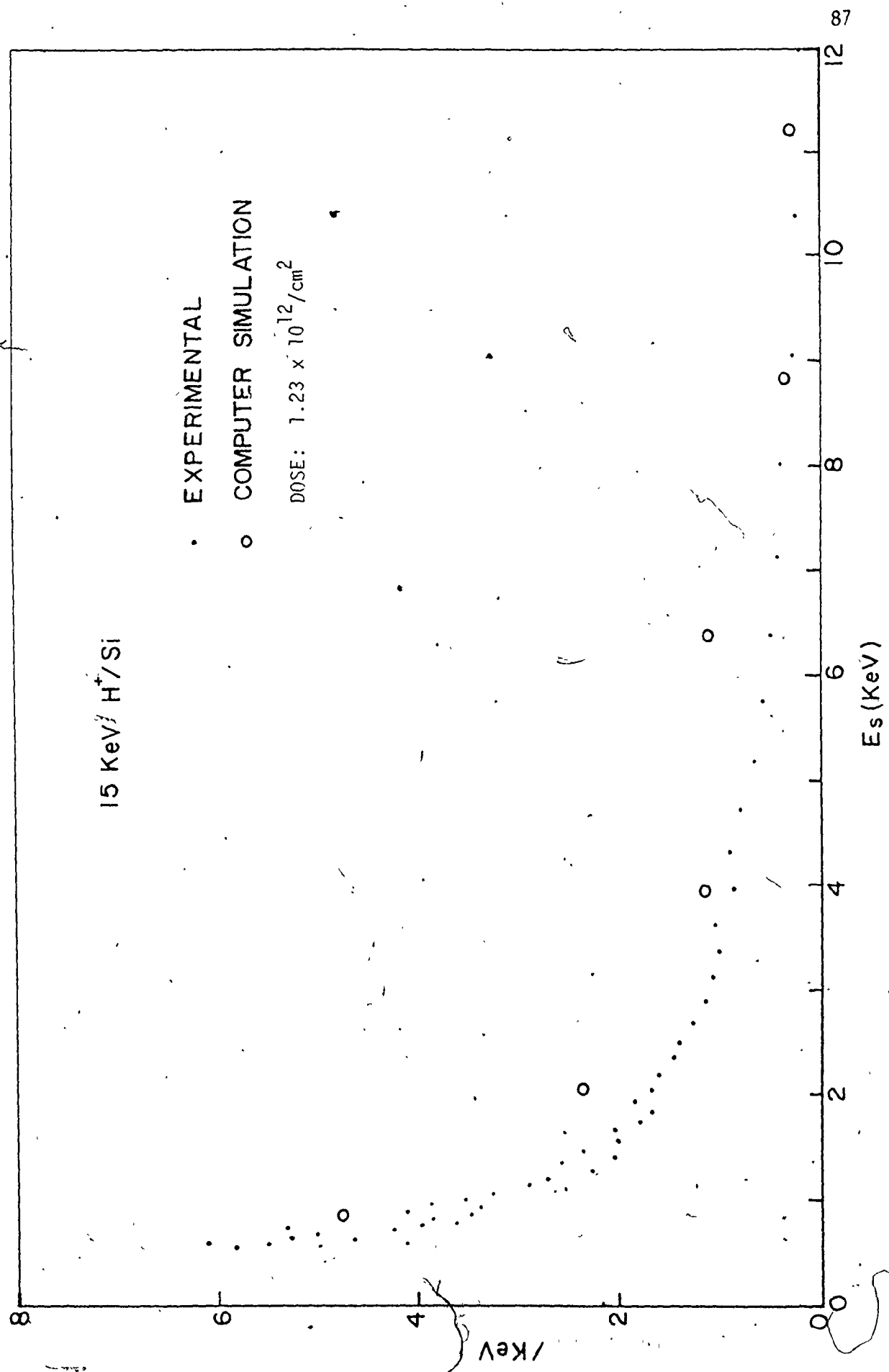
Fig. 6.10: Energy distribution of backscattered particles for 15 keV H$^+$/Si.
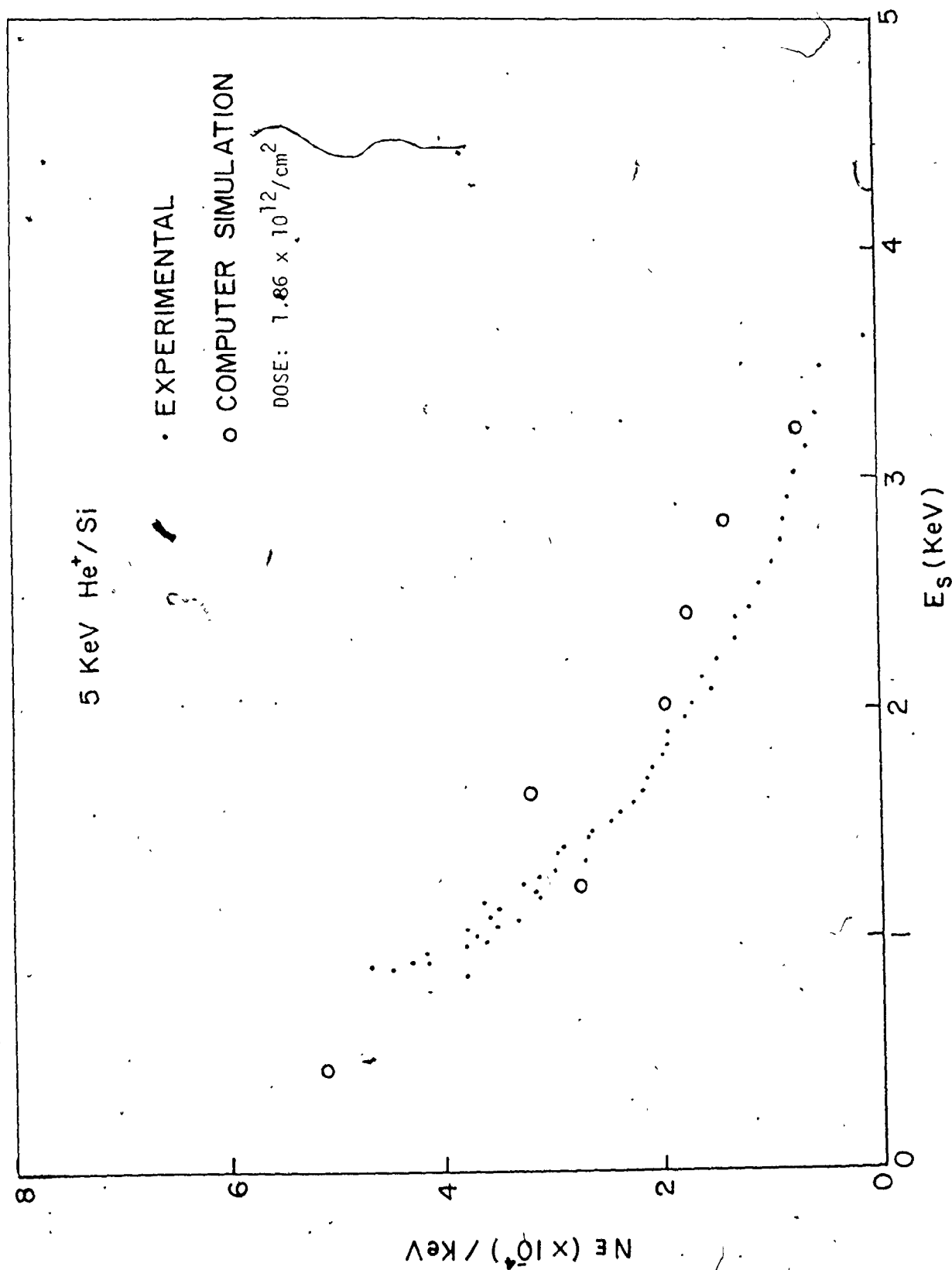
Fig. 6.11: Energy distribution of backscattered particles for 5 keV He$^+$/Si.
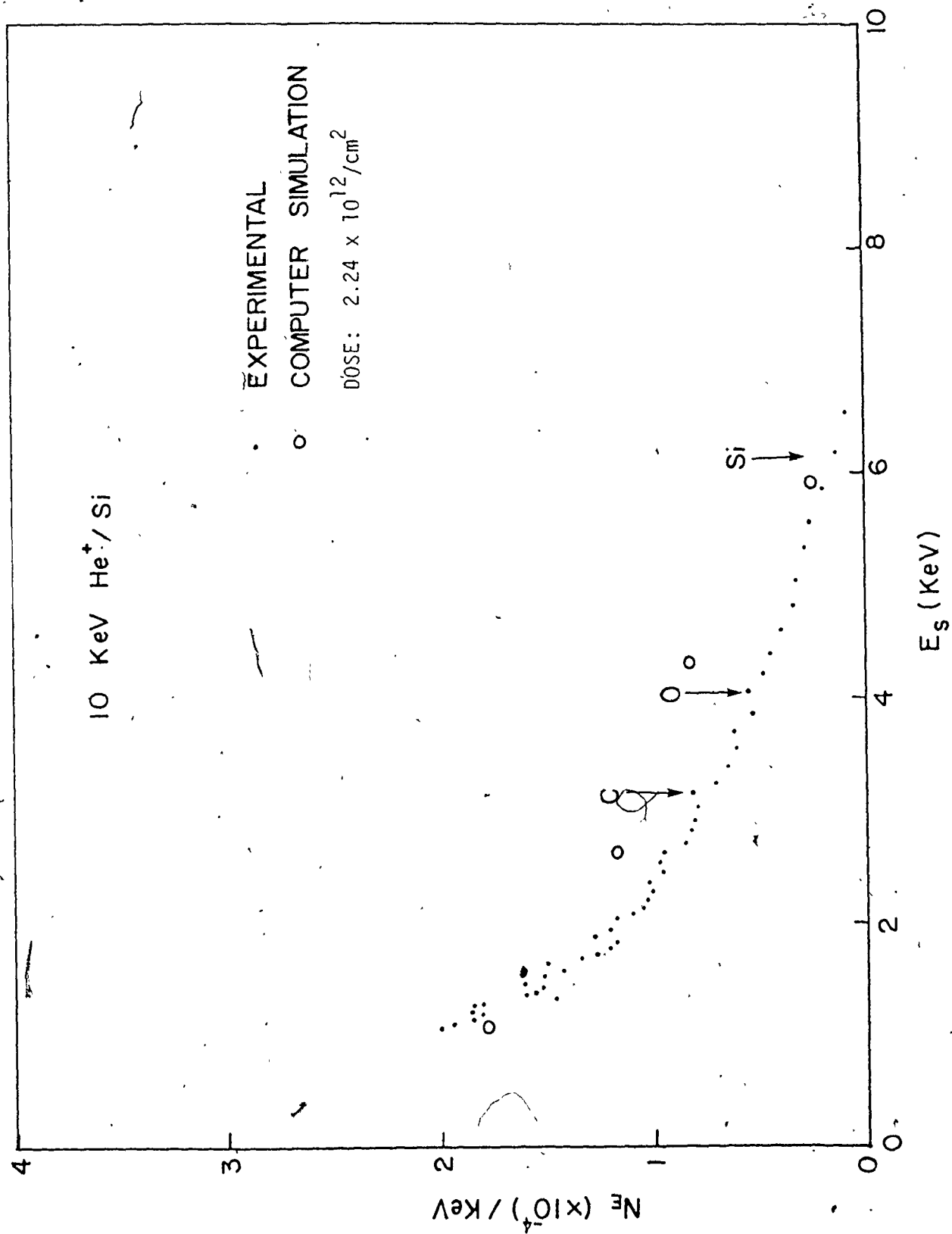
Fig. 6.12: Energy distribution of backscattered particles for 10 keV He$^+$/Si.
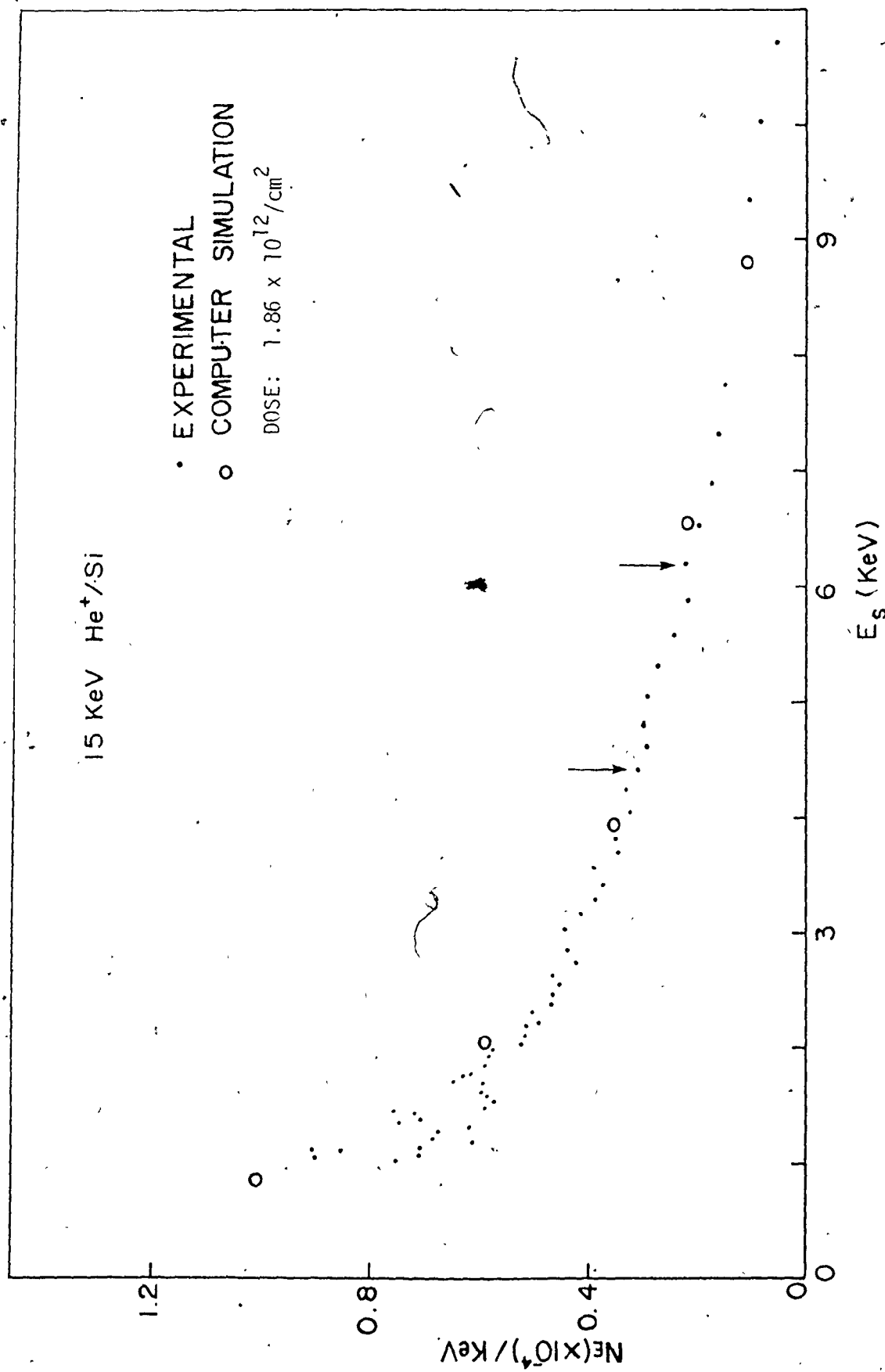
Fig. 6.13: Energy distribution of backscattered particles for 15 keV He$^+$/Si.

although the scattering cross section for this energy range is high, most of the backscattered particles come from atomic layers inside the target through multiple scattering events. The helium sensitivity for surface analysis could be seen from these spectra. The regions marked by arrows (in the 10 and 15 keV helium spectra) correspond to scattering from oxygen and carbon atoms on the surface. This is not pronounced in the 5 keV helium case (as should be expected) because the energy is low enough that the scattering from deeper layers will obscure the oxygen and carbon signals. This effect is not found in the hydrogen spectra.

In all cases studied, the energy spectra show particles with energies higher than the single scattering events; these correspond to multiple scattering from the surface. This effect has been shown in the computer simulation in Chapter 3.

To check the reproducibility of the TOF results, the same experiments were repeated. Figure 6.14 shows the energy spectra for two such runs for 10 keV helium ions. As can be seen from this figure the experiment is fairly reproducible to better than 10%.

To check the effect of the incidence angle on the backscattered energy distribution, the target was tilted at 30° and -15° between the incident beam and the surface normal. The TOF spectra for 5 keV hydrogen were recorded and transformed to energy spectra which are shown in figure 6.15. Two major effects could be concluded from this experiment: the high energy portion for the three positions are almost the same while the low energy side differs markedly for the 30°
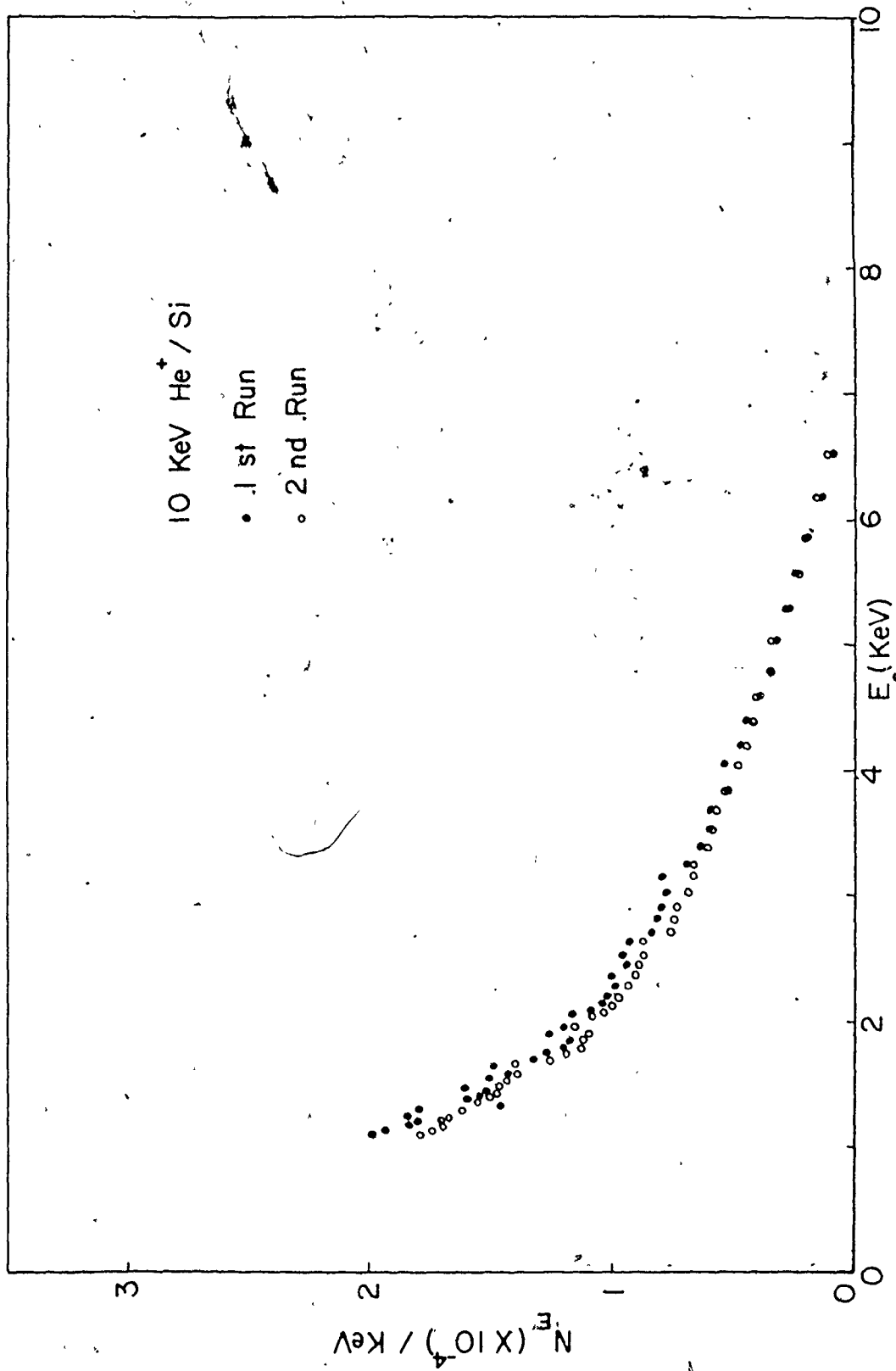
Fig. 6.14: Energy distribution of backscattered particles for 10 keV He⁺/Si (reproducibility check).

The plot is labeled "10 KeV He⁺ / Si" with legend "• 1 st Run" and "○ 2 nd Run". The horizontal axis is labeled E_s (KeV) ranging from 0 to 10. The vertical axis is labeled $N_E (\times 10^{-4}) / KeV$ ranging from 0 to 3.
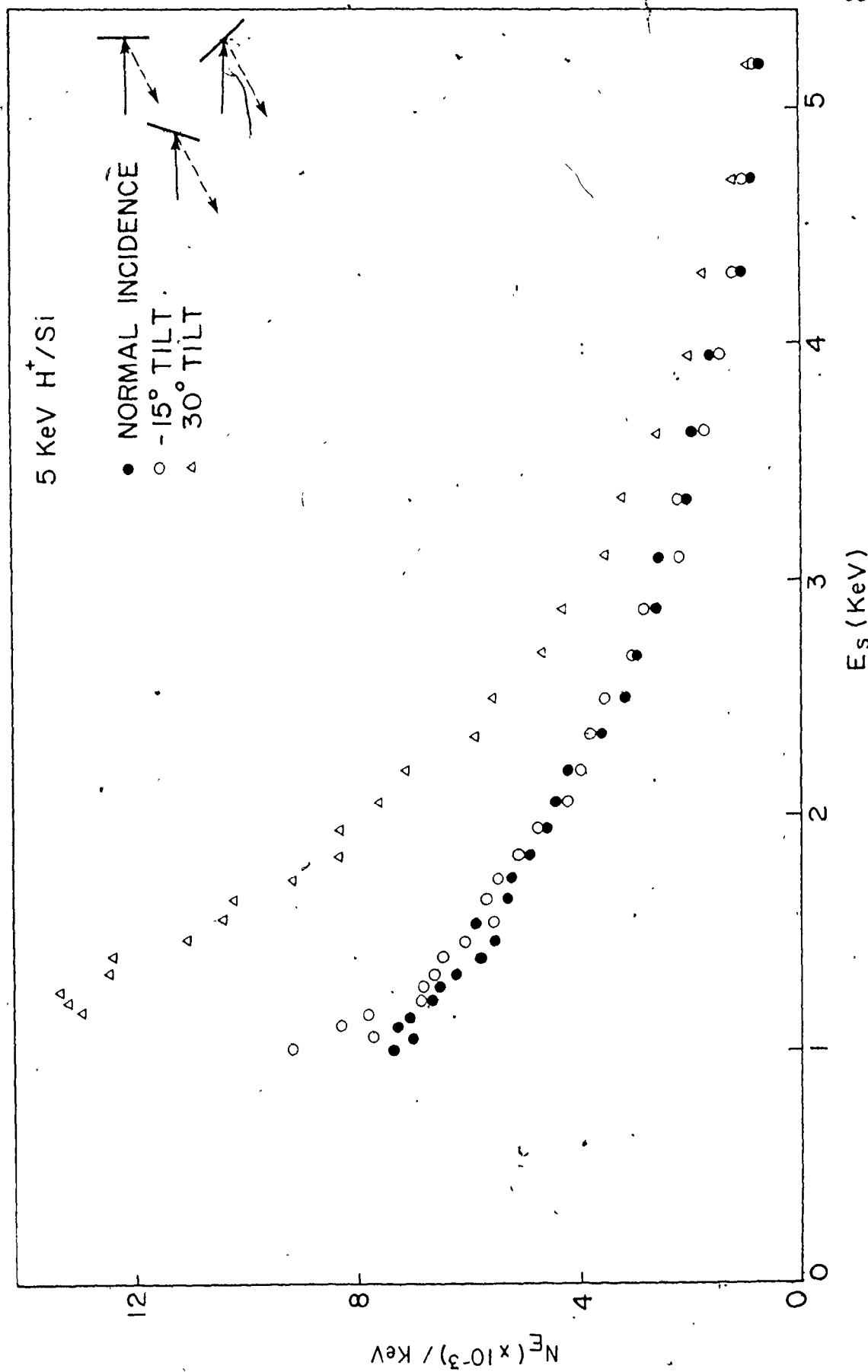
Fig. 6.15: Effect of angle of incidence on the energy spectra.

tilt indicating more contribution from the multiply scattered particles to the backscattered yield. Therefore it could be concluded that the single collision model could explain the high energy portion of the spectra while a multiple collision model should be used to interpret the low energy side of the energy spectra. Also, comparing the high energy backscattered particles for the three tilt angles, it could be seen that there was no effect of particle channeling along the <111> direction in the original experiments, i.e. the incident beam did not penetrate the target along a channeling direction.

6.5 Conclusions

To avoid the problems involved with the use of the electro-static analyzers or solid state detectors, the time-of-flight technique was used to measure the energy distribution of the total backscattered particles (neutrals and ions) for hydrogen and helium ions incident on a silicon target in the energy range of 5-15 keV.

The 30 nanosecond pulses used for beam chopping give a reasonably good time resolution (7% and 4% for 15 keV hydrogen and helium ions respectively). For lower energies the resolution will be much better since it is proportional to $\Delta t/t$, where Δt is the pulse width and t is the flight time.

The shape of the TOF can be explained using the multiple scattering model. A backscattered particle with a certain energy (i.e. certain flight time) will originate from different depths, or generally after a certain length of the total range, inside the material depending

on the incident energy. If the incident particle has higher energy, the total range of the scattered particles will be longer and consequently this particle will have a greater probability of being scattered away from the direction of the detector. This explains why the TOF spectrum is broader for lower incident energy or heavier incident ion or generally for smaller value of the reduced energy ε.

The energy spectra calculated from the recorded time-of-flight spectra, after correcting for the channeltron efficiency, aré in good quantitative agreement with the corresponding spectra calculated using the computer simulation technique.

The energy spectra recorded in this work do not show any maxima at low energies. This same trend was also observed in the measurements of Sidenius and Lenskjaer (65). Eckstein et. al. (61), on the other hand, recorded maxima in the energy distributions of the backscattered particles between 1 and 3 keV, the positions of these maxima depending on the incident energy. This discrepancy could be due to some uncertainties in the calibration of the gas stripping cell, especially for lower backscattered energies.

The main problem with using the time-of-flight technique is the interference of the sputtered particles with the detected signal. Generally the long time (or low energy) tail of the TOF spectra is due to sputtered particles. For heavier ions, sputtering contributes to the high energy side of the spectrum as well. To reduce this effect, low repetition rate for beam chopping should be used; but this will be at the expense of the magnitude of the incident beam and consequently of the data acquisition time.

CHAPTER 7

CHARGE FRACTIONS MEASUREMENTS

7.1 Introduction

For the energy range of interest in this thesis (below 20 keV), the available quantitative data on the charge fractions of backscattered particles are rare. Theoretical investigations are even more scarce.

Behrisch et al. (67) have performed measurements on charge fractions of hydrogen backscattered from solid targets of Be, V, Cu, Nb, Mo and Ta in the energy range of 5-150 keV. Buck et al. (68,69) measured charge states for 25-190 keV hydrogen and helium backscattered from Cu, Si (69) and Au (68). They also investigated the effect of surface cleaning by measuring charge fractions for particles back-scattered from practical and cleaned surfaces (68).

Measurements of charge fractions for ion bombardment of thin foils have been done at energies as low as 3 keV. Phillips (70) reported charge equilibrium ratios for hydrogen after transmission through different foils. His experiment was performed under fairly poor vacuum conditions ($>5 \times 10^{-6}$ Torr), and the results showed that the freshly coated foils (Al, Be, Ca, Ag, Au, SiO) exhibits a different behavior than those for which some time had elapsed after deposition.

Recently Buck et al. (5) measured the charge fractions for 6-32 keV argon backscattered from a gold target using the time-of-flight technique. Charge fractions for 1-5 keV hydrogen backscattered from

gold targets were reported by Eckstein and Matschke (71) using the stripping technique. Using the same stripping technique, charge fractions of helium and neon backscattered from nickel in the energy range of 1.5-15 keV were measured by Eckstein et. al (72).

At present there is no theory which explains the medium and low energy neutralization behavior in detail. One important feature of several theoretical treatments (73-75) is that neutralization occurs outside the surface as the ion leaves. The theories assume that Debye-type screening by the electron gas prevents bound states while the ion is inside. As the ion leaves the surface, neutralization occurs either by recombination (73) with electron in the surface distribution or by tunneling (74) from the solid. Another neutralization mechanism occurs by an Auger process (76). Figures 7.1 and 7.2 show schematic diagram for tunneling and Auger neutralization processes.

Very recently Erickson and Smith (77) developed a new model for neutralization at low energies. They observed oscillations in the ISS yield as a function of the primary energy for helium scattered from Ga, Ge, In, Sn, Sb, Pb and Bi. These oscillations were not found in the case of Al, Si, Ag, Cd, Cu and As. This phenomena is explained qualitatively as follows: the incident ion and the surface atom are considered to form a quasimolecular state while in close proximity. At sufficiently high velocity the interaction time is very short ($\sim 10^{-16}$ sec), so that an electron from the solid has just time to jump to the ion and neutralize it. At lower energies several transfers between the two atoms can occur leading to maxima and minima in the neutralization probability.
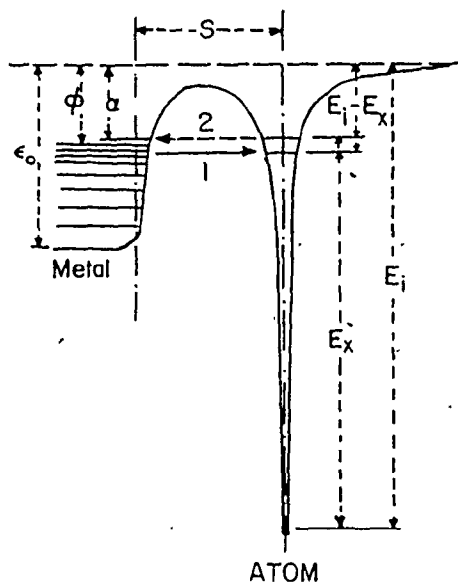
Transition 1 can occur only
at energy levels which are
filled inside the metal.
Transition 2 at levels which
are empty.

Fig. 7.1: Schematic diagram illustrating
tunneling mechanism.
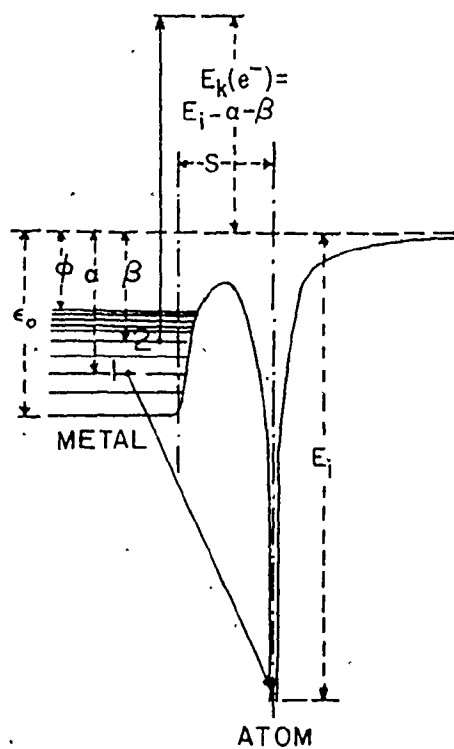
If the excited electron escapes,
$E_k(e^-)$ is its kinetic energy
observed outside the metal.

Fig. 7.2: Schematic diagram illustration
Auger neutralization.

Generally, no single theoretical model is capable of explaining the neutralization process. Therefore combination of these models, or together with other unknown mechanisms, could explain what actually happens as the incident ion penetrates the solid and then scatters back.

7.2 Experimental Results

All charge fraction measurements were performed for normal incidence and a fixed scattering angle of 135°. The time-of-flight technique was used to measure spectra for neutrals only and neutrals plus ions backscattered from a silicon target. First a zero bias was applied to the deflecting plates in the TOF tube. In this case all backscattered particles (neutrals and ions) could reach the detector and a TOF spectrum for the total yield could be recorded. Applying a bias to the deflecting plates, the ion portion of the backscattered particles will be deflected away from the detector and therefore a TOF spectrum for the neutral yield only could be recorded. Comparing these two spectra, the charge fractions of the backscattered particles were determined as a function of the backscattered energy.

The silicon target was cleaned in the same way described in the previous chapter. Before running the TOF experiment, the target was further cleaned by bombarding with 5 keV neon at a dose of approximately $10^{16}/cm^2$ under high vacuum conditions.

Figure 7.3 shows the TOF spectra for the total and neutrals for 10 keV hydrogen backscattered from the silicon target. The two

spectra start to coincide at lower energies (higher channel number or time-of-flight).

The charged fraction, C.F., is defined as follows:

$$C.F. = \frac{N_t - N_n}{N_t}$$

where N_t and N_n are the number of counts per time interval (62 nano-seconds) for the total and neutral spectra respectively.

Transforming the time scale to energy scale, the charge fractions are plotted as a function of the backscattered energy as shown in figure 7.4. In this figure charge fractions for incident energy of 5 keV H^+ and 5 keV H_2^+ are recorded as well. It can be seen that for hydrogen backscattered from silicon there is no surface peak for the charge fractions even at lower incident energies.

A similar experiment was done using helium ions as incident particles. The TOF spectra for 10 keV helium is shown in figure 7.5. From these spectra it is noticed that complete neutralization of the backscattered particles occurs at a much smaller depth (i.e. higher energy) as compared to the hydrogen case.

Again, the charge fractions were calculated as a function of the backscattered energy and this is shown in figure 7.6. As shown in this figure, the charge fractions have a pronounced surface peak in contrast with hydrogen; this indicates a completely different neutralization mechanism. In the same figure the charge fractions for 6 keV helium is shown and again a sharp surface peak was found.
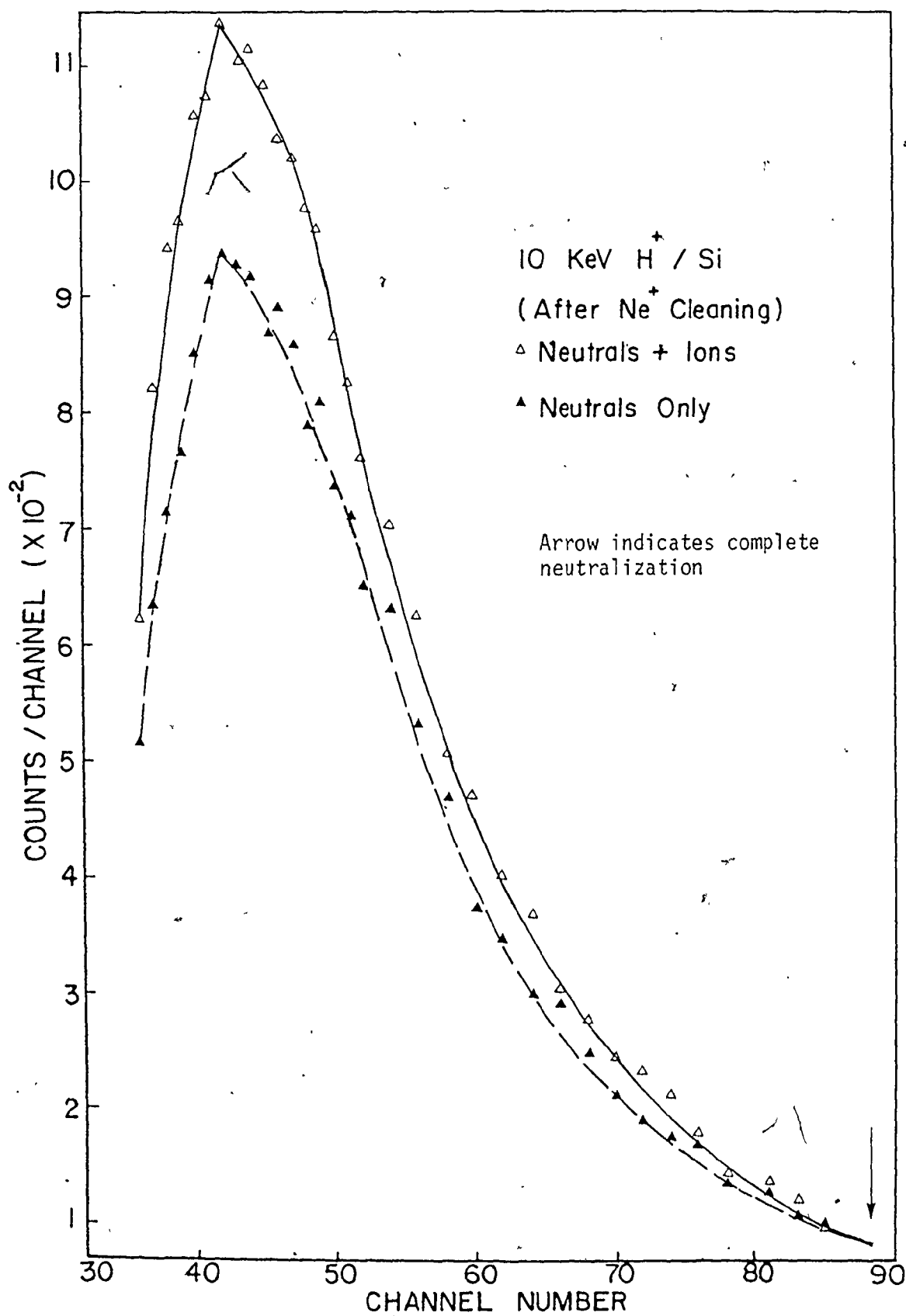
Fig. 7.3: Time-of-flight spectra for total and neutral particles for 10 keV H^+/Si.
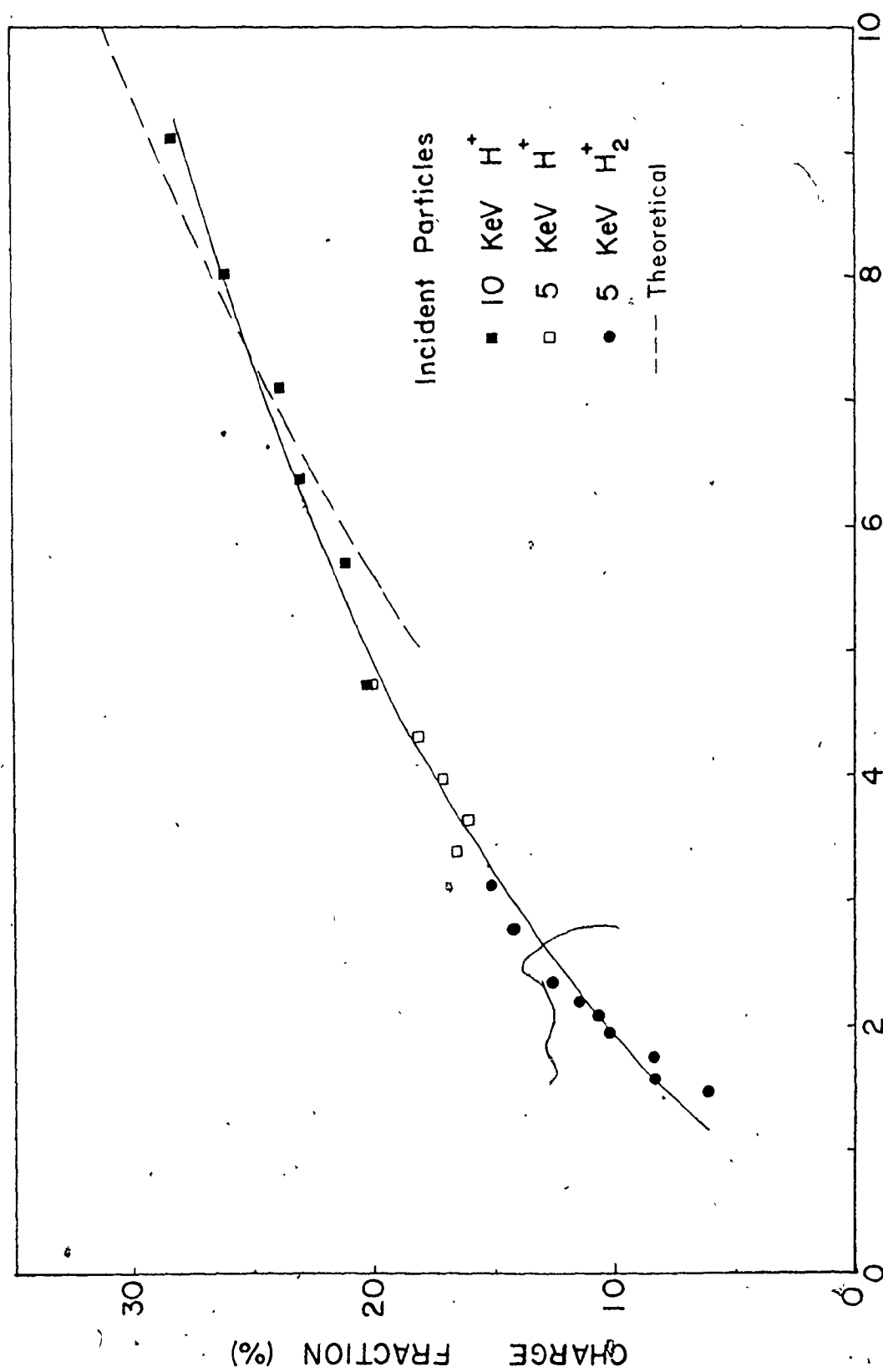
Fig. 7.4: Charge fractions of backscattered particles for H^+/Si.
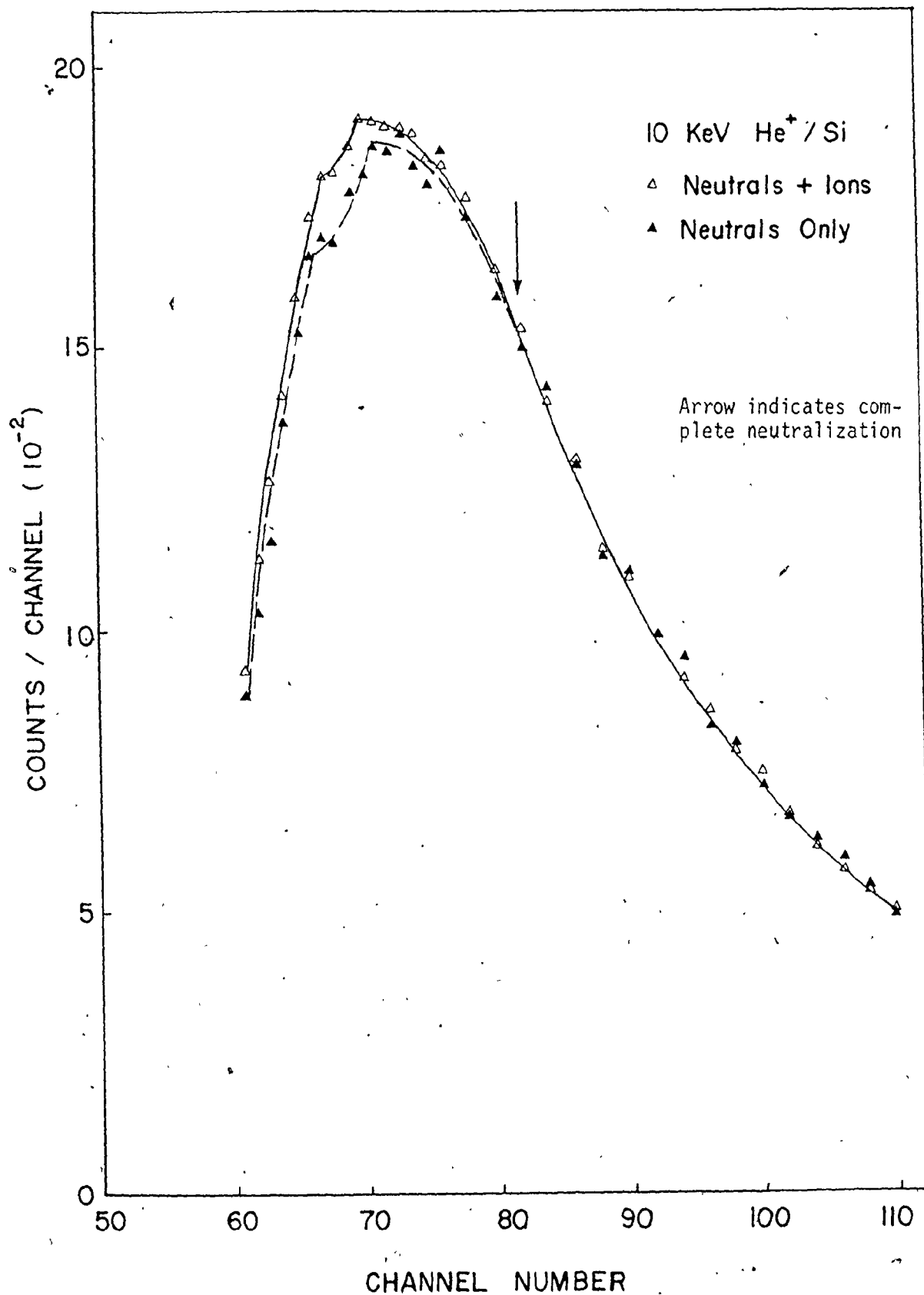
Fig. 7.5: Time-of-flight spectra for total and neutral particles for 10 keV He$^+$/Si.
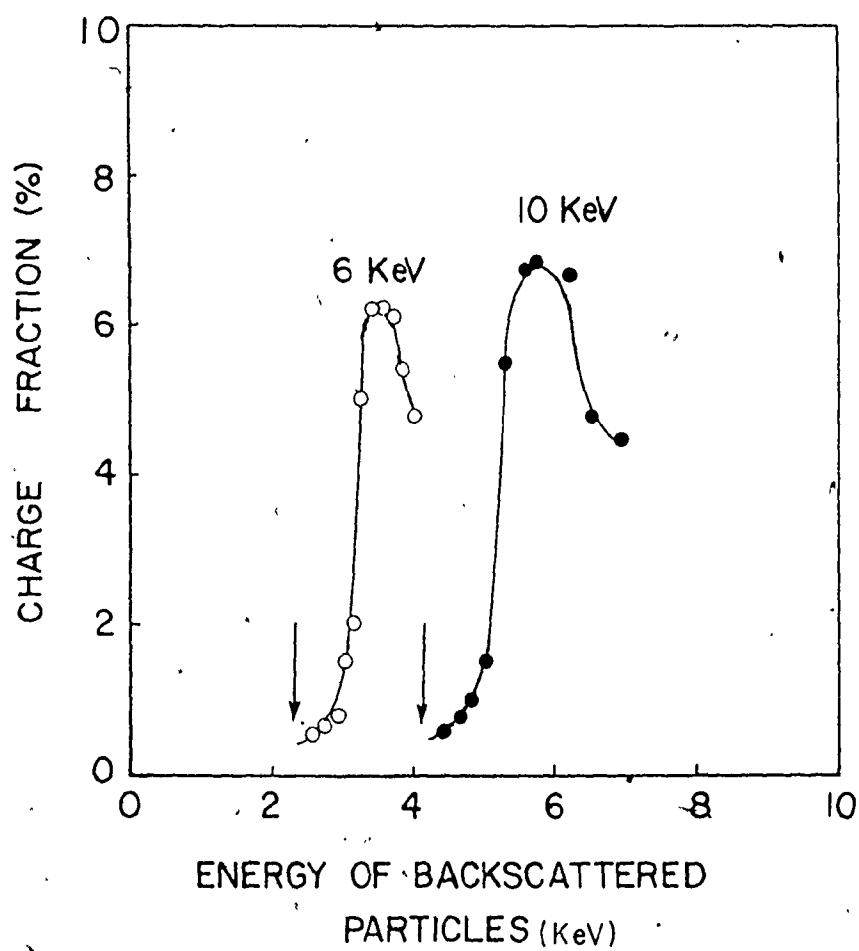
Fig. 7.6: Charge fractions of backscattered particles for He^+/Si.

* Arrows indicate complete neutralization

7.3 Effect of Surface Cleaning

Since the charge state is determined mainly by the outermost few monolayers of the surface (74), therefore the surface condition should be of prime importance in determining the charge fractions.

To examine the effect of surface cleanliness, the TOF technique was used again to measure the charge fractions of 10 keV hydrogen backscattered from a practical and a clean silicon target.

The spectra from a practical target were obtained by scattering from a chemically cleaned silicon target; these are shown in figure 7.7a. Using 5 keV neon bombardment, adsorbed gases and hydrocarbon contaminants were removed from the surface and the clean scattering experiments were done quickly after bombardment. The clean spectra are shown in figure 7.7b. Comparing the practical and clean spectra, it could be seen that an improvement of a factor of ~ 2 in the charge fraction was achieved by cleaning the silicon surface.

The target was then left in the scattering chamber for two days at a pressure of approximately 2×10^{-8} Torr, and the same experiments were repeated. Figures 7.8a and 7.8b show the spectra without further cleaning and after 5 keV neon cleaning respectively. As seen from these sepctra, the surface conditions returned to the practical case within two days in the target chamber. Neon cleaning gave the same trend obtained before with a fresh clean target.

7.4 Discussion and Conclusions

The charge fractions data obtained in these experiments show
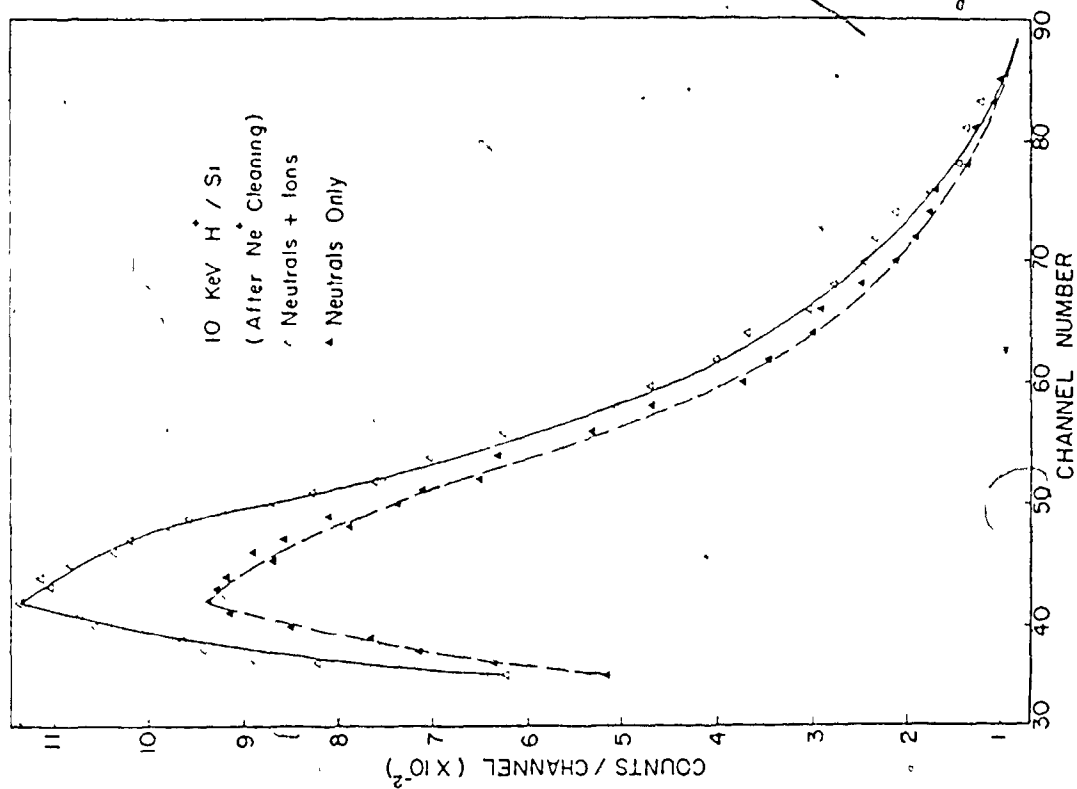
Fig. 7.7b: Same target after 5 keV Ne$^+$ sputter cleaning.
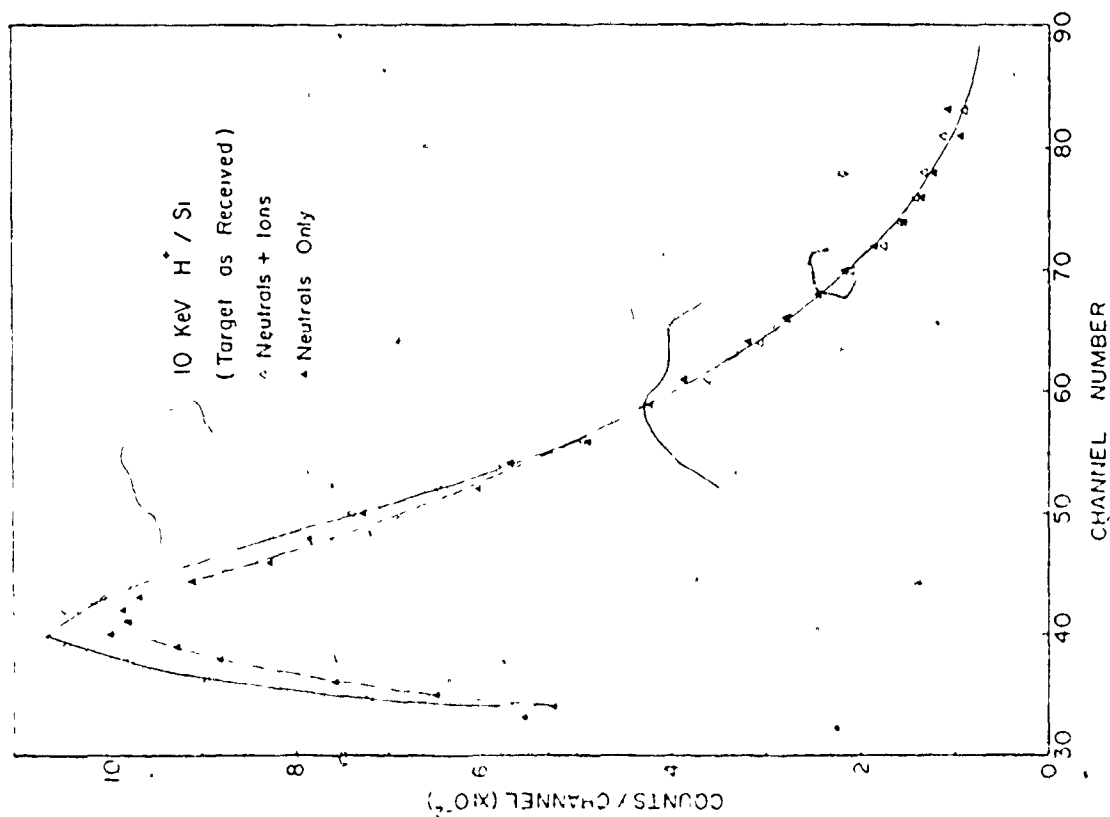
Fig. 7.7a: Time-of-flight spectrum for 10 keV H$^+$/Si (target as received).

Fig. 7.8b: Same target after 5 keV Ne+ sputter cleaning.

10 KeV H+ / Si
(After Ne+ Cleaning)
△ Neutrals + Ions
▲ Neutrals Only

COUNTS / CHANNEL (X 10²)
CHANNEL NUMBER
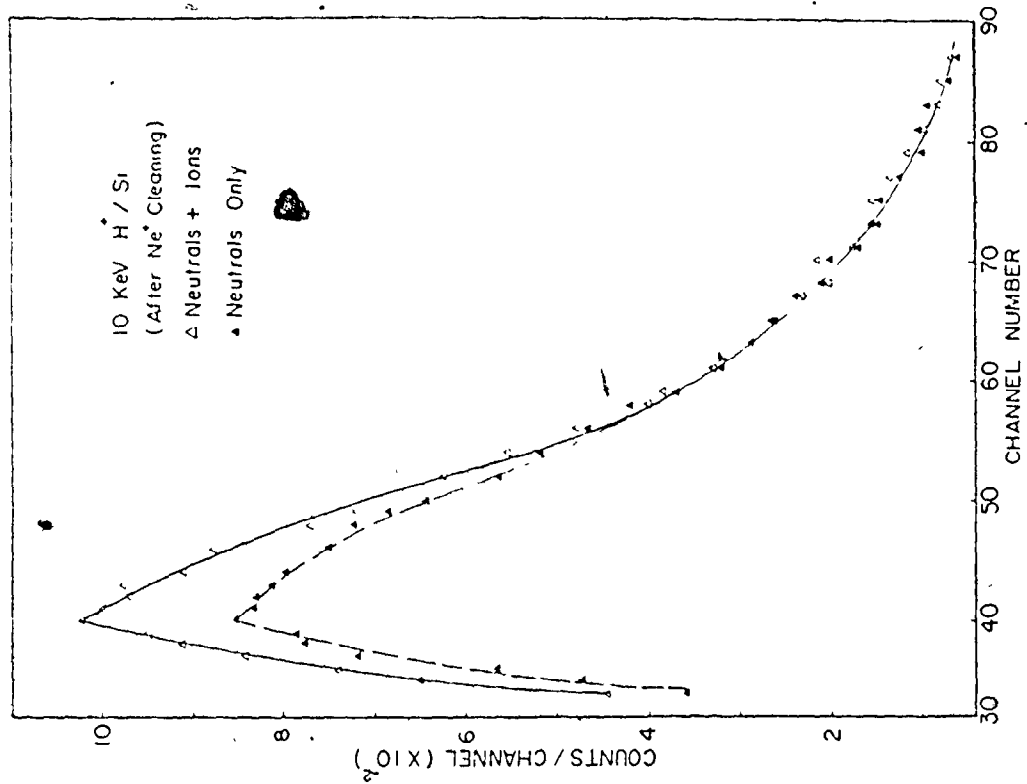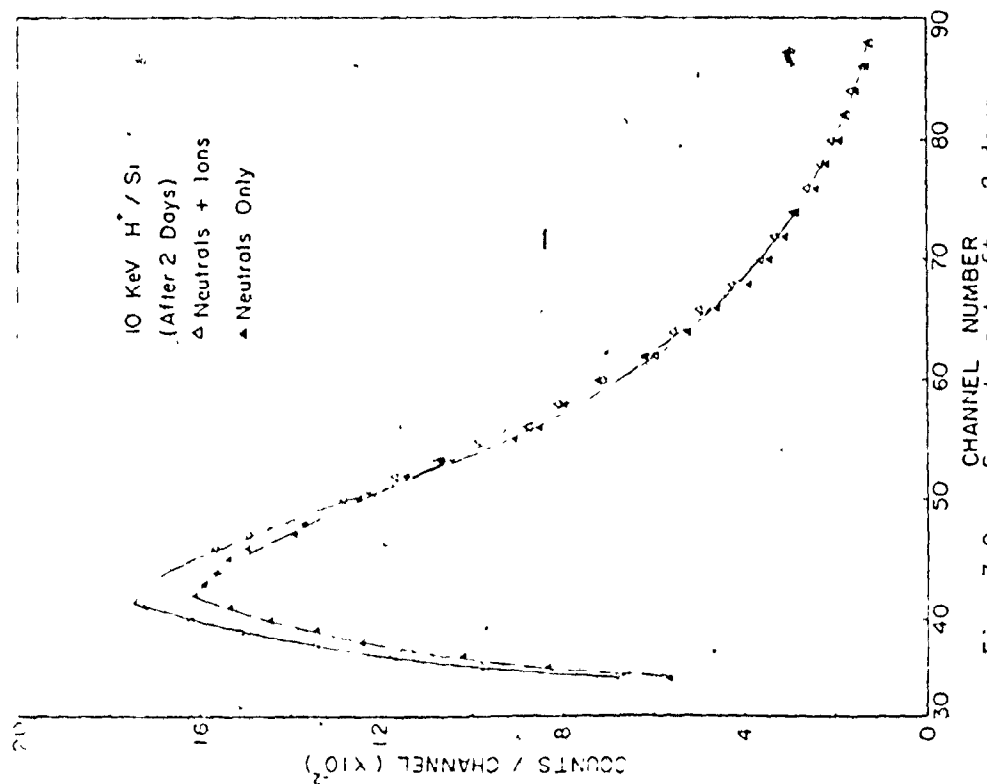
Fig. 7.8a: Same target after 2 days.

10 KeV H+ / Si
(After 2 Days)
△ Neutrals + Ions
▲ Neutrals Only

COUNTS / CHANNEL (X 10²)
CHANNEL NUMBER

different mechanisms of ion neutralization for hydrogen and helium. The following is concluded from the experimental data.

1. For the case of hydrogen scattering there is no evidence of penetration dependence. The fact the charge fractions of 10 keV hydrogen and 5 keV molecular hydrogen lie on the same curve, figure 7.4, show that the neutralization occurs outside the surface. This supports the theoretical models given by Yavlinskii et. al. (73) and by Brandt and Sizmann (75). In the same figure extrapolation of charge fractions data given by Brandt and Sizmann is shown; this is taken from reference number (69). The agreement is relatively good.

2. For helium scattering, on the other hand, the previous model of neutralization outside the surface is not sufficient to describe the data obtained. As can be seen from figure 7.6, complete neutralization of ions penetrating the surface takes place. Also doubly scattered particles are neutralized more efficiently than singly scattered ones. This results in surface peaks for charge fractions. This trend was observed by Buck et. al. (5) for argon scattered from gold and by Eckstein et. al. (72) for neon and helium scattered from nickel. The charge state dependence on penetration depth could be explained by the fact that the electron capture cross section σ_c is much higher than the electron loss cross section σ_ℓ for helium. Once a helium ion is neutralized it is very unlikely to lose its electron again and therefore bound states are created inside the target, opposite to the Brandt and Sizmann model for hydrogen. The neutral fractions inside the target could be found from the relation (78)

$$\frac{N_n}{N_t} = \left(1 + \frac{\sigma_\ell}{\sigma_c}\right)^{-1} \quad \text{which is very large}$$

3. Neon bombardment cleaning of the silicon target increases the charge fractions of hydrogen by a factor of 2 as shown in figures 7.7(a,b) and 7.8(a,b). The experiment shown in figure 7.7a was done on a target similar to that characterized by Auger Electron Spectroscopy (AES) in figure 6.1. The carbon and oxygen contaminants on the surface cause the reduction in the charge fractions. After neon cleaning (doses of approximately $10^{16}/cm^2$), the surface will be similar to that in figure 6.2 and the charge fractions increase. If the neutralization process for hydrogen occurs outside the surface by a tunneling mechanism (73), therefore an oxide layer will inhibit this process and increase the charge fractions. Contrary to this effect, when the target was left under vacuum (2×10^{-8} Torr) for two days the charged fractions decreased again to approximately the same values as for the practical target. The AES was used again to analyze the sample in similar circumstances, the spectra being shown in figures 6.3 and 6.4. From this it could be easily seen that the carbon increases more than the oxygen (by comparing figures 6.2 and 6.3). The carbon layer masks the surface and the decrease in the charge fractions could be mainly due to this carbon layer. Neon sputtering will remove this layer and the charge fractions increase again as shown in figures 7.8b. This surface cleaning effect emphasizes the idea that neutralization occurs outside the surface and is mainly affected by the last few monolayers.

* under similar vacuum conditions as the experiment.

CHAPTER 8

SUMMARY

This thesis presents a theoretical and an experimental study of the interaction of low and medium energy hydrogen and helium ions with solids. In the energy range studied in this work (below 20 keV), the interaction process is complicated by two factors, namely, the interatomic potential governing the collision events is not precisely known; and the neutralization effects of the backscattered particles which goes as high as 95%. In the following summary, the main results obtained in this work are reviewed.

1. In this study a Monte-Carlo technique was applied to determine the energy distribution of backscattered particles. A Thomas-Fermi interatomic potential was used and consequently scattering cross sections developed by Lindhard et. al. (7) were applied. Both electronic (inelastic) and nuclear (elastic) energy losses were considered. To determine the interaction parameters, three random numbers were used and the histories of 5,000 to 10,000 particles were followed. From the energy spectra obtained it was noticed that there is a depletion in surface scattering, i.e. most backscattered particles undergo more than one nuclear collision. No peaks in the energy spectra were found and some of the backscattered particles have energies higher than those corresponding to single surface collision which indicate double scattering from the surface. This was also found

110

experimentally. The same program determined the angular distribution of the backscattered particles which could be approximated by a cosine distribution.

2. An experimental analysis system was developed using the time-of-flight technique. Both neutral and charged backscattered particles were analyzed. The analysis system and technique was first applied to surface analysis where very thin films of silver (20-40 Å) were deposited on silicon substrates. Hydrogen and helium ions were used to analyze these targets. The sensitivity of the technique was found to be better than 1/20 of a monolayer of silver on silicon; and the resolution was in agreement with the TOF resolution and electronic energy loss broadening. In the TOF experiments precautions were made to improve the signal to noise ratio; ratios of 100:1 were achieved in these measurements. Another alternative for surface analysis was found by using the TOF spectra only instead of the ordinarily used energy spectra. The TOF spectra have much sharper peaks that could be used directly to identify the surface constituents easily.

3. The TOF technique was used to measure the backscattered energy spectra for hydrogen and helium scattered from a silicon target. The spectra were corrected for the channeltron efficiency and therefore a cut-off energy (500 eV) was used because of the detector calibration. The energy spectra deduced from the TOF spectra are in good qualitative and quantitative agreement with those determined from the computer simulation technique.

4. The charged fractions experiments indicate that neutralization

is mainly affected by the outermost atomic layers of the solid.
For hydrogen the neutralization takes place outside the surface; no
penetration effects take place. This is in agreement with the mechanism
which assumes that hydrogen moves as ions inside the solid (75).
On the other hand, helium ions experience preferential neutralization
inside the solid which gives surface peaks in the charged fraction.
These peaks were not observed in the case of hydrogen.

Surface cleaning has an important effect on the charged
fractions. Removing the carbon layer from the silicon surface by
neon bombardment improves the charged fraction by a factor of two.
If the target is left in the scattering chamber (18 hours at 2×10^{-8}
Torr) the surface regains the practical target conditions and further
cleaning is required to remove the carbon contamination.

TOTAL SCATTERING CROSS SECTION AS A FUNCTION OF THE REDUCED
ENERGY

$$\sigma = 0.6545 \, \pi \, a^2 \, Y$$

APPENDIX B

MONTE-CARLO COMPUTER CODE FOR ION-SCATTERING STUDIES

```
      PROGRAM TST (INPUT,OUTPUT,TAPE5=INPUT,TAPE6=OUTPUT)
C     ATOMIC SCATTERING AND TRANSPORT CODE
C     USING THOMAS-FERMI INTERACTION POTENTIAL
C     CONSIDERING BOTH ELECTRONIC AND NUCLEAR SCATTERING
C     GLOSSARY
C
C
C     AT        THOMAS-FERMI SCREENING RADIUS
C     AD IS ATOMIC DENSITY OF TARGET MATERIAL
C     AV        AVOGADRO#S NUMBER
C     THE MASS AND ATOMIC NOS. OF THE TARGET MATERIAL AND THE
C     INCIDENT IONS ARE DENOTED BY A2,A1,Z2,AND Z1.
C     RHO IS THE DENSITY OF THE TARGET MATERIAL.
C     AV IS AVOGADROS NUMBER
C     EPSI SCATTERING ANGLE IN LAB SYSTEM  IN RADS
C     (DE/DX) FOR ELECTRONIC ENERGY LOSS=EK*E**0.5
C     THET IS THE SCATTERING ANGLE IN THE C.O.M. SYSTEM AND
C     SR IS THE SCREENING RADIUS
C     EIII IS THE INCIDENT ION ENERGY
C     TOTNP IS THE NUMBER OF INCIDENT PARTICLES
C     ETOTA=AVERAGE DAMAGE ENERGY
C     ECOLA=AVERAGE DAMAGE ENERGY ABOVE THIN
C
C
      DIMENSION ENDIST(200)
      DIMENSION F(100),E(100),EPSI(2),D(2),
     1THET(86,15),F(86),EPSAPR(15),EER(100),RRR(100)
      DIMENSION A11(8),Z11(8),SF(8),EII(3)
C     INPUT CONSISTS OF EPSAAP ,THE REDUCED ENERGY
      DATA(EPSARP(I),I=1,15)/.01,.0185,.0342,.0633,.1171,.2167,.4009,
     *.7417,1.372,2.538,4.696,8.687,16.07,29.73,55.0/
      READ(5,3022) (F(I),I=1,86)
      READ(5,3023) ((THET(I,J),J=1,15),I=1,86)
      READ(5,4) (RRR(I),I=1,100), (EER(I),I=1,100)
C     ***************************************************************
C     INPUT PARAMETERS
      EIII=10.0
      A1=4.
      Z1=2.
      STOPF=1.55
      TOTNP=400.
      Z2=14.
      A2=28.
      RHO=2.33
      ECUT=0.25
C     ***************************************************************
360   PI=3.14159265
      DENCM=(Z1**(2./3.)+Z2**(2./3.))**(1./2.)
      SR=0.8853*.529*.1E-07/DENOM
      C=A2/(A1+A2)*SR/(Z1*Z2*(4.8*.1E-09)**2)
      CON22=1.6021*.1E-08
      CONEQ3=C*CON22
      CON124=2.*(CON22)**.5
      AV=6.02252*.1E+25
      AD=RHO*AV/A2
      A=A2/A1
      ALPHA=((A-1.)/(A+1.))**2
      EK=3.*PI*AD*(4.8*.1E-09)**2*.529*.1E-07/(25.*1.6021*.1E-08)**0.5*
     1Z1**(7./6.)*Z2/(DENOM)**3
     1/(A1**.5)*STOPF
```

```
      C2=((Z1**(2./3.)+Z2**(2./3.))**.75)/((Z1**(2./3.))*(Z2**.5))
     1*(A1**.5)*((A1+A2)**.5)/(A2**.5)*3.152/STOPF*.6545
      C2=C2*.75
      DO 100 I=1,100
      E(I)=EER(I)/CON603
      R(I)=RRR(I)/1.+C2.
100   CONTINUE
343   EEN=EIII
      EPS=CON603*EIII
C
      DO 398  III=1,200
      ENDIST(III)=0.
398   CONTINUE
      ANGT=0.
      EPKT=0.
      MM=0
      M=0
      EMIN=EIII
      EMAX=0.
      WRITE(6,301)
      WRITE(6,3)
      WRITE (6,1) A1,A2,Z1,Z2,RHO
      WRITE(6,3)
      WRITE(6,2)   EIII
      WRITE(6,3)
      WRITE(6,22) EPS
      WRITE(6,3)
      WRITE(6,3012) STOPF
      WRITE(6,3)
      WRITE(6,3911) ECUT
      WRITE(6,301)
      WRITE(6,3)
      WRITE(6,703)
      WRITE(6,3)
      NNNN=TOTNP
      DO 400 N=1,NNNN
      NN=0
      EI=EEN
      K=1
      EPSI(1)=0.
      EPSI(2)=0.
      PHI=0.
      PR1=0.
C     PHI AZIMUTHAL ANGLE
C     PR PROJECTED RANGE
500   IF(EI-E(12)) 705,705,706
706   IF(EI-E(24)) 707,707,708
708   IF(EI-E(36)) 709,709,710
710   IF(EI-E(48)) 711,711,712
712   IF(EI-E(60)) 713,713,714
714   IF(EI-E(72)) 715,715,716
716   IF(EI-E(84)) 717,717,718
705   NA=1
      NB=12
      GO TO 750
707   NA=12
      NB=24
      GO TO 750
709   NA=24
      NB=36
```

```
          GC TO 750
711       NA=36
          NB=48
          GO TO 750
713       NA=48
           NB=60
          GC TO 750
715       .NA=60
          NB=72
          GO TO 750
717       NA=72
          NB=84
          GO TO 750
718       NA=84
          NB=100
750       DO 800 I=NA,NB
          IF(EI-E(I))  802,801,800
  800 CONTINUE
  801 EI=E(I)
          RO=R(I)
          GO TO 803
  802 RO=R(I-1)+(R(I)-R(I-1))/(E(I)-E(I-1))*(EI-E(I-1))
803       CALL FRANEN (RN1,1,1)
          IF(RN1.EQ.1.)  GO TO 400
          DELR=ALOG(1.-RN1)
          R1=RO+DELR
          IF (R1.LT.R(1)) GO TO 400
          IF(R1-R(12)) 605,605,606
606       IF(R1-R(24)) 607,607,608
608       IF(R1-R(36)) 609,609,610
610       IF(R1-R(48)) 611,611,650
650       IF(R1-R(60)) 651,651,652
652       IF(R1-R(72)) 653,653,654
654       IF(R1-R(84)) 655,655,656
605       NA=1
          NB=12
          GC TO 911
607       NA=12
          NB=24
          GO TO 911
609       NA=24
          NB=36
          GO TO 911
611       NA=36
          NB=48
          GO TO 911
651       NA=48
          NB=60
          GO TO 911
653       NA=60
          NB=72
          GO TO 911
655       NA=72
          NB=84
          GO TO 911
656       NA=84
          NB=100
911       DO 600 I=NA,NB
          IF(R1-R(I))  602,601,600
  600 CONTINUE
```

```
  601 R1=R(I)
      EB=E(I)
      GO TO 603
  602 EB=E(I-1)+(E(I)-E(I-1))/(R(I)-R(I-1))*(R1-R(I-1))
  603 EPS=CON603*EB
  124 D(K)=CON124/EK*(SQRT(EI)-SQRT(EB))
      IF(D(K).LT.5.E-08) D(K)=2.5E-08
C     D(K) IS ACTUAL DISTANCE TRAVERSED BY ION
      CC1=COS(EPSI(1))
      CC2=COS(EPSI(2))
      SI1=SIN(EPSI(1))
      SI2=SIN(EPSI(2))
      CO3=COS(PHI)
C     Q1=COS(EPSI(1))
      Q1=CO1*CO2+SI1*SI2*CO3
      Q2=SI1*CO2+SI2*CO1*CO3
      PR2=PR1+D(K)*Q1
      PRP=PR2   *.1E+07
      L=PRP
      L=L+1
      EPSI(1)=ACOS(Q1)
      IF(Q1.GT.0.)  GO TO 18
      IF(Q2)   38,37,37
   37 BA=FI-EPSI(1)
      GO TO 18
   38 EPSI(1)=2.*PI-EPSI(1)
      BA=EPSI(1)-PI
   18  IF(PR2) 325,325,23
  325    M=M+1
C     BACK-SCATTERING ANGLE IS EPSI(1)
      DS=-PR1    /COS(EPSI(1))
      DS=ABS(DS)
C     DS IS THE DISTANCE TO THE SURFACE
      EBK=(SQRT(EI*CON22)-.5*EK*DS)**2/CON22
      EBKT=EBKT+EBK
C'    EBK BACK-SCATTERING ENERGY
      IF(Q1.GT.0.)    BA=EPSI(1)
      BA=BA*180./PI
      ANGT=ANGT+BA
C.    BA IS THE BACK-SCATTERING ANGLE IN DEGREES
      WRITE(6,701)   M,EBK,BA
      L10=IFIX((EBK-ECUT)/(EEN-ECUT)*24.)+1.
      ENDIST(L10)=ENDIST(L10)+1.
      GO TO 400
   23 IF(EB.GT.ECUT) GO TO 180
      GO TO 400
  180 CALL FRANCM (PN2,1,J)
C     CALCULATION OF SCATTERING ANGLE IN C.M. SYSTEM
      IF(EPS-.01) 88,88,777
   88 K1=1
      GO TO 19
  777 K1=1
      DO 44 NNEP=1,14
      K1=K1+1
      K4=K1-1
      IF((EPS-EPSAFR(K1)).LE.0.) GO TO 19
   44 CONTINUE
   19 IF(PN2-.05) 89,89,90
   89 THETA=(1.15+(PN2/.05)*.09)*(PI/180.)
      GO TO 915
```

```
90      IF(RN2.GT..9995) GO TO 501
        IF(RN2.GT..995) GO TO 502
        IF(RN2.GT..98) GC TO 503
        IF(RN2.GT..90) GO TO 504
         IF(RN2.GT..80) GO TC 505
        GO TO 506
501     RAT=(RN2-.9995)/.00032
        K2=RAT
        K2=K2+61
         GO TO 550
502     RAT=(RN2-.995)/.0005
        K2=RAT
        K2=K2+52
         GC TO 550
503     RAT=(RN2-.98)/.001
        K2=RAT
        K2=K2+37
         GO TO 550
504     RAT=(RN2-.9)/.005
        K2=RAT
        K2=K2+21
         GO TO 550
505     RAT=(RN2-.8)/.02
        K2=RAT
         K2=K2+16
         GC TO 550
506     RAT=RN2/.05
         K2=RAT
         GO TO 550
550     K3=K2+1
        THETA1=THET(K2,K1)
        THETA2=THET(K3,K1)
         THETA3=THET(K2,K4)
        THETA=(THETA1+(RN2-F(K2))*(THETA2-THETA1)/(F(K3)-F(K2)))*PI/180.
       1-(EPS-EPSARR(K1))*(THETA3-THETA1)/(EPSARR(K1)-EPSARR(K4))*PI/180.
916     FT=(SIN(THETA/2.))**2.
        TVAR1=A*COS(THETA)
58      Q=(TVAR1      +1.)/(A**2+2.*TVAR1.      +1.)**.5
        EPSI(K)=ACOS(Q)
        TVAR2=1.-ALPHA
83      EI=EB*(1.-       TVAR2*FT)
C       EI PARTICLE ENERGY AFTER NUCLEAR COLLISION
        Y=2.*(EI*1.6021*1.E-09)**.5/EK
172     NN=NN+1
        IF(EI.GT.ECUT) GO TO 170
        GO TO  400
170     CALL FRANCN (RN3,1,J)
        AK=K
        PHI=2.*PI*RN3*(AK-1.)
        PP1=PP2
        K=2
        GO TO 500
400     CONTINUE
        BSN=M
        REFLC=BSN/TOTMP
         WRITE(6,7) REFLC
        WRITE(6,3)
        IF(BSN.LE.0.5) GO TO  905
        AEBK=(EBKT/BSN)/EIII
        WRITE(6,14) AEBK
```

```
      WRITE(6,3)
      GAMMA=REFLC*AEBK
      WRITE(6,3010) GAMMA
       WRITE(6,3)
      AANG=ANGT/BSN
      WRITE(6,15) AANG
905   X=0.
      DO 900 I=1,24
      X=X+(1./24.)
      XX=ENDIST(I)
      CALL PLOTPT(X,XX,4)
900   CONTINUE
      CALL OUTPLT
      WRITE(6,3020)
      WRITE(6,3)
      WRITE(6,1003)
      WRITE (6,3)
      DO 960 KKK=1,24
      WRITE(6,8) ENDIST(KKK)
960    CONTINUE
      WRITE(6,3)
C      FORMAT STATEMENTS
1     FORMAT(2F10.6,2F4.1,F6.3)
   2  FORMAT(5X,*INITIAL ENERGY(KEV)=*,F8.4)
   3  FORMAT(//)
   4  FORMAT(E12.5)
7     FORMAT(5X,*TOTAL REFLECTION COEFFICIENT=*,F12.6)
   8  FORMAT(6E12.6)
14     FORMAT(5X,*AVERAGE SCATTERED ENERGY=*,E12.6)
15     FORMAT(5X,*AVERAGE SCATTERED ANGLE=*,F8.4)
22    FORMAT(5X,*EPSILON=*,F8.4)
1003  FORMAT (5X,*NO. OF PARTICLES PER ENERGY INCREMENT*)
3010  FORMAT(5X,*GAMMA(SCATTERED ENERGY FRACTION)=*,F10.7)
3011  FORMAT(5X,*SPECTRUM CUTOFF-KEV*,F10.7)
3012   FORMAT(5X,*STOPPING COEFFICIENT*,F10.7)
3020  FORMAT(5X,*SCATTERED ENERGY DISTRIBUTION/24 UNITS*)
3022   FORMAT(5X,5F10.6)
3023    FORMAT(10F7.2)
  701 FORMAT(10X,I5,11X,E12.6,8X,E12.6)
  703 FORMAT(5X,*PARTICLE NUMBER*,5X,*PARTICLE ENERGY*,5X,*SCATTERING AN
     1GLE*)
  301 FORMAT(1H1)
      STOP
      END
```

COTOT   344

PULSER CIRCUIT
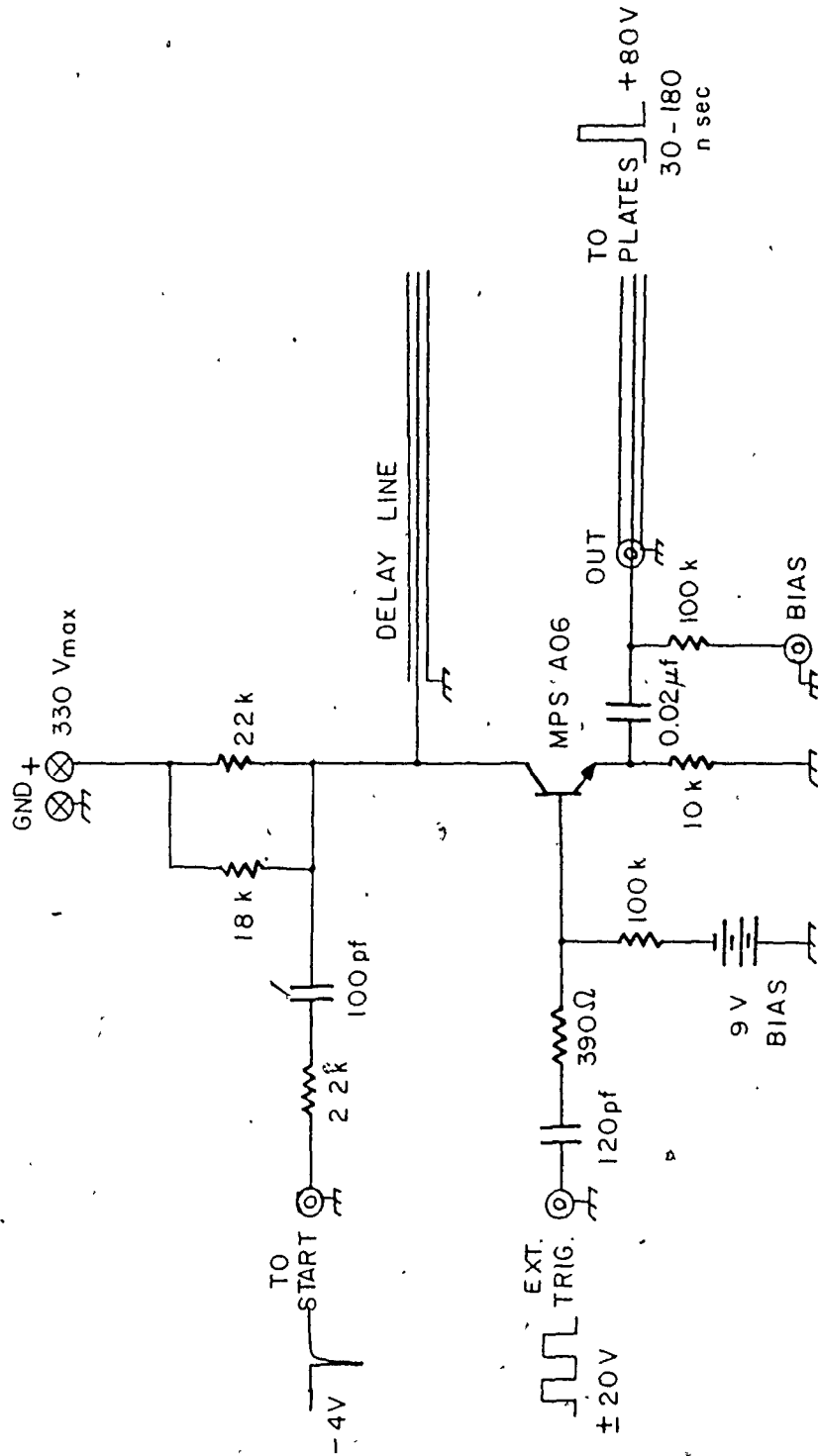
PULSE CHARACTERISTICS:

Amplitude	+ 80 V
Duration	30-180 nanoseconds
Rise time	1-3 nanoseconds

APPENDIX D

COMPUTER PROGRAM FOR THE ANALYSIS OF THE EXPERIMENTAL RESULTS

```
      PROGRAM TST (INPUT,OUTPUT,TAPE5=INPUT,TAPE6=OUTPUT)
C     TIME-OF-FLIGHT,ENERGY SPECTRA AND CHARGED FRACTION MEASUREMENTS
C     CORRECTED FOR CHANNELTRON EFFICIENCY
      DIMENSION CN(512),TN(512),T(512),E(512),EN(512),EE(30),EFF(30)
      DIMENSION CE(512),ES(512),ESN(512),ERN(512),EST(512),ENT(512),CF(5
     112),ER(512)
      FL=129.0
      PM=1.66E-24
      PP=4.0
      PM=PM*PP
      TM=29.0
      A=TM/PP
      CT=1.0625
      EC=15.0
      NO=22
      BGD=0.
      NNS=256
      READ (5,22)   (EE(K),EFF(K),K=1,17)
      WRITE(6,19)
      DO 89  I=1,17
      XX=EE(I)
      YY=EFF(I)
   89 CALL FLCTFT(XX,YY,4)
      CALL OUTFLT
      WRITE(6,19)
      WRITE(6,2)
      DO 1001  I=1,512
 1001 TN(I)=1.
      CN(1)=1.
      DO 10  I=2,512
   10 CN(I)=CN(I-1)+1.
      READ(5,1)   (TN(I),I=1,NNS)
      DO 20  I=2,NNS
   20 TN(I)=TN(I)-BGD
C     TN IS COUNTS PER TIME INTERVAL
      DO 73  I=1,NNS
   73 T(I)=0.0
      NO=NO+1
      DO 30  I=NO,NNS
   30 T(I)=T(I-1)+DT
   81 WRITE (6,18)
      WRITE (6,103)
      WRITE(6,11)   (CN(I),T(I),TN(I),I=NO,NNS)
      DO 81  MM=NO,NNS
      XX=T(MM)
      YY=TN(MM)
   81 CALL FLCTFT(XX,YY,4)
      CALL OUTFLT
      DO 14  KK=NO,NNS
      E(KK)=0.
      ES(KK)=0.
   14 EN(KK)=0.
      Y=0.5*PM*FL**2*1.5+21/1.602
      DO 40  K=NO,NNS
   40 E(K)=Y/T(K)**2
      NNS=NNS-1
      DO 41  I=NO,NO+
      CF(I)=E(I)-E(I+1)
      EN(I)=TN(I)/CF(I)
C     EN IS COUNTS PER KEV
```

```
      ES(I)=EF(I)-DE(I)/2.
C     ES IS ENERGY IN THE CENTRE CF INTERVAL
   41 CONTINUE
      WRITE (6,16)
      WRITE (6,17)
      WRITE (6,104)
      WRITE (6,21)    (ES(I),EN(I),I=N0,NNS)
      DO 1129   I=N0,NNS
 1128 EF(I)=FS(I)/EC
      DO 312   I=N0,NNS
      IF(ES(I)-0.5)   301,302,302
  301 ES(I)=0.
      EN(I)=0.
      MMM=I
      GO TO 303
  302 CONTINUE
  303 DO  91   NM=46,MMM
      XY=ES(NM)
      YX=EN(NM)
   91 CALL  FLCTFT(XY,YX,4)
      CALL  CUTFLT
      WRITE (6,16)
      WRITE (6,18)
      WRITE (6,105)
      DO 77   N=N0,MMM
      IF(ES(N)-9.0)     9,6,6
    6 CEFF=1.0
      GO TO 27
    9 IF(ES(N)-0.1)     25,26,26
   25 EN(N)=0.0
      GO TO 77
   26 DO 88   K=1,17
      IF(ES(N)-EE(K))     66,99,88
   88 CONTINUE
   99 CEFF=EFF(K)
      GO TO 77
   66 CEFF=EFF(K-1)+((EFF(K)-EFF(K-1))/(EE(K)-EE(K-1)))*(ES(N)-EE(K-1))
   27 EN(N)=EN(N)/CEFF
   77 CONTINUE
      WRITE(6,32)   (CN(I),T(I),TN(I),ES(I),ER(I),EN(I),I=N0,MMM)
      DO 101   MM=N0,MMM
      XX=T(MM)
      YY=TN(MM)
  101 CALL  FLCTFT(XX,YY,4)
      CALL  CUTFLT
      DO 102   NM=46,MMM
      XY=ES(NM)
      YX=EN(NM)
  102 CALL  FLCTFT(XY,YX,4)
      CALL  CUTFLT
    1 FORMAT  (1FF5.0)
    2 FORMAT(15X,*INCIDENT ENERGY=1F.1 KET HE/SI*///////)
   11 FORMAT ((10X,F5.0,2(13X,E12.F)//)).
   16 FORMAT(15X,*TIME-OF-FLIGHT SPECTRUM*//)
   17 FORMAT(15X,*ENERGY SPECTRUM*//)
   18 FORMAT(15X,*SPECTRA CORRECTED FOR CHANNELTRON EFFICIENCY*//)
   19 FORMAT(1H1)
   21 FORMAT(10X,E12.F,10X,E12.F/)
   22 FORMAT  (1FF5.3)
   32 FORMAT ((10X,FF.0,5(13X,E12.F)//))
```

```
 47 FORMAT(15X,*NEUTRALS PLUS IONS*///////)
 57 FORMAT(20X,*NEUTRALS ONLY*///////)
103 FORMAT(7X,*CHANNEL NO.*,14X,*TOF*,14X,*COUNTS/TIME INT.*//)
104 FORMAT(13X,*ENERGY*,10X,*COUNTS/ENERGY INT.*//)
105 FORMAT(7X,*CHANNEL NO.*,12X,*TOF*,13X,*COUNTS/TIME INT.*,12X,*ENER
   *GY*,12X,*REDUCED ENERGY*,5X,*COUNTS/ENERGY INT.*//)
107 FORMAT(10X,E12.6,10X,E12.6/)
    STOP
    END
```

CUTOT   129

REFERENCES

1. APS-Report: Report to the American Physical Society by the Study group on physics problems relating to energy technologies, Rev. Mod. Phys. 47, 529 (1975).

2. Hogan, J.T. and Clarke, J.F., J. Nucl. Mat. 53, 1 (1974).

3. Kane, P.F. and Larrabee, G.R., Characterization of Solid Surfaces, Plenum Press, New York (1974).

4. Smith, D.P., J. App. Phys. 38, 340 (1967).

5. Buck, T.M., Chen, Y.S. and Wheatley, G.H., Surface Science 47, 244 (1975).

6. Chicherov, V.M., Soviet Phys. -JETP Letters 16, 231 (1972).

7. Lindhard, J., Nielsen, V. and Scharff, M., Mat. Fys. Medd. Dan. Vid. Selsk. 36, No. 10 (1968).

8. Bohr, N., Mat. Fys. Medd. Dan. Vid. Selsk. 18, No. 8 (1948).

9. Carter, G. and Colligon, J.S., Ion Bombardment of Solids, American Elsevier Publishing Company, Inc. (1968).

10. Oen, O.S., Holmes, D.K. and Robinson, M.T., J. App. Phys. 34, No. 2 (1963).

11. Ball, D.J., Buck, T.M., McNair, D. and Wheatley, G.H., Surface Science 30, 69 (1972).

12. Lindhard, J. and Scharff, M., Phys. Rev. 124, No. 1 (1961).

13. McCracken, G.M. and Freeman, N.J., J. Phys. B 2, No. 2 (1969).

14. Born, M. and Mayer, J.E., Zeits. f. Physik 75, No. 1 (1932).

15. Gombas, P., Handbuch der Physik, Ed. XXXVI (1956).

16. Firsov, O.B., Soviet Phys. -JETP 5 1192 (1957).

17. Lindhard, J., Scharff, M. and Schiott, H.E., Mat. Fys. Dan. Vid. Selsk. 33, No. 14 (1963).

18. Schiott, H.E., Mat. Fys. Dan. Vid. Selsk. 35, No. 9 (1966).

19. Winterbon, K.B., Sigmund, P. and Sanders, J.B., Mat. Fys. Medd. Dan. Vid. Selsk. 87, No. 14 (1970).

20. Vukanic, J. and Sigmund, P., App. Phys. 11, 265 (1976).

21. Weissmann, R. and Sigmund P., Rad. Effects 19, No. 7 (1973).

22. Sigmund, P., Matthies, M.T. and Phillips, D.L., Rad. Effects 11, No. 39 (1971).

23. Sanders, J.B., Can. J. Phys. 46, 455 (1968).

24. Baroody, E.M., J. App. Phys. 36, 3565 (1965).

25. Bottiger, J. and Winterbon, K.B., Rad. Effects 20, No. 65 (1973).

26. Robinson, M.T. and Oen, O.S., App. Phys. Letters 2,30 (1963). Phys. Rev. 132, 2385 (1963).

27. Oen, O.S., Robinson, M.T., J. App. Phys. 35, 2515 (1964).

28. Beeler, J.R. and Besco, D.G., J. App. Phys. 34, 2873 (1963). Phys. Rev. A 134, 530 (1964).

29. Ishinati, T., Shimizu, R. and Murata, K., Jap. J. App. Phys. 11, No. 2, 125 (1972).

30. Robinson, J.E. and Agamy, S., Atomic Collisions in Solids, ed. by S. Datz, B.R. Appleton and C.D. Moak (Plenum Press, New York), 215 (1975).

31. Robinson, J.E., Rad. Effects 23, 29 (1974).

32. Ormrod, J.H. and Duckworth, H.E., Can. J. Phys. 41, 1424 (1963).

33. Thompson, D., Robinson, J.E. and Walker R., Rad. Effects 32, 169 (1977).

34. Winterbon, K.B., AECL Report #3194 (1968).

35. Verbeek, H., J. App. Phys., Vol. 46, No. 7 (1975).

36. El-Kareh, A.B. and El-Kareh, J.C.J., Electron Beams, Lenses, and Optics, Vol. I, Academic Press, New York (1970).

37. Adams, J. and Manley, B.W., Philips Technical Review, Vol. 28, Nos. 5/6/7, 156 (1967).

38. Burrous, C.N., Lieber, A.J. and Zaviantseff, V.T., Rev. Sci. Instr., Vol. 38, No. 10, 1477 (1967).

39. Cranall, D.H., Ray, J.A. and Cisneros, C., Rev. Sci. Instr. 46, 562 (1975).

40. Herzog, R.F. and Viehböck, F., Phys. Rev. 76, 855 (1949).

41. Benninghoven, A., Surface Science 35, 427 (1973).

42. Rettinghans, G. and Huber, W.K., App. Phys. 1, 301 (1973).

43. Gray, T.J., Lear, R., Dexter, R.J. Schwettmann, F.N. and Wiemer, K.C., Thin Solid Silms 19, 103 (1973).

44. Buck, T.M. and Poate, J.M., J. Vac. Sci. Technol. 11, No. 1, 289 (1974).

45. Meek, R.L., Buck, T.M. and Gibbon C.F., J. Electrochem. Soc. 120, 1241 (1973).

46. Buck, T.M. and Wheatley, G.H., Surface Science 33, 35 (1972).

47. Seidel, T.E. and Meek, R.L., Ion Implantation in Semiconductors and Other Materials, ed. by B.L. Crowder (Plenum Press, New York), 305 (1973).

48. Mitchell, I.V., Kamoshida, M. and Mayer, J.W., J. App. Phys. 42, 4378 (1971).

49. Feldman, L.C. and Rodgers, J.W., J. App. Phys. 41, 3776 (1970).

50. Heiland, W. and Taglauer, E., Rad. Effects 19, No. 1 (1973).

51. Begemann, S.H.A. and Boers, A.L., Surface Science 30, 134 (1972).

52. Heiland, W. and Taglauer, E., J. Vac. Sci. Technol. 7, 72 (1970).

53. Brongersma, H.H. and Mul, P.M., Surface Science 35, 393 (1973).

54. Behrisch, R. and Weissmann, R., Phys. Letters A 30, 506 (1969).

55. Mackintosh, D. and Davies, J.A., Analytical Chemistry, 41, No. 4, 26A (1969).

56. Mayer, J.W., Erikson, L. and Davies, J.A., Ion Implantations in Semiconductors, Academic Press, New York (1970).

57. Agamy, S.A. and Robinson, J.E., Nucl. Instr. Methods (in press).

58. Chen, Y.S., Miller, G.L., Robinson, D.A.H., Wheatley, G.H. and Buck, T.M., Surface Science, 62, 133 (1977).

59. Assuming a stopping power value of 10-15 eV/cm^2/10^{15} atoms for He-Ag based on similar data in: Ormrod, J.H., MacDonald, J.R. and Duckworth, H.E., Can. J. Phys. 43, 275 (1964).

60. Behrisch, R., Eckstein, W., Meischner, P., Scherzer, B.M.U. and Verbeek, H., in: Atomic Collisions in Solids, Vol. I, ed. by S. Datz, B.R. Appleton and C.D. Moak (Plenum, New York), 315 (1975).

61. Meischner, P. and Verbeek, H., J. Nucl. Materials 53, 276 (1974).

62. Eckstein, W., Matschke, F.E.P. and Verbeek, H., J. Nucl. Materials 63, 199 (1976).

63. Thompson, M.W., Farmery, B.W. and Newson, P.A., Phil. Mag. 18, 361 (1968).

64. Buck, T.M., Wheatley, G.H., Miller, G.L., Robinson, D.H.H. and Chen, Y.S., Nucl. Instr. Methods (in press).

65. Robinson, J.E. and Agamy S.A., Proc. 7th Intern. Vac. Cong. and 3rd Intern. Conf. Solid Surfaces (Vienna 1977).

66. Sidenius, G. and Leuskjaer, T., Nucl. Instr. Methods 132, 673 (1976).

67. Behrisch, R., Eckstein, W., Meischner, P., Scherzer, B.M.U. and Verbeek, H., Atomic Collisions in Solids, ed. by S. Datz, B.R. Appleton and C.D. Moak (Plenum Press, New York), (1975).

68. Buck, T.M., Feldman, L.C. and Wheatley, G.H., Atomic Collision in Solids, ed. by S. Datz, B.R. Appleton and C.D. Moak (Plenum Press, New York), (1975).

69. Buck, T.M., Wheatley, G.H., and Feldman, L.C., Surface Science 35, 345 (1973).

70. Phillips, J.A., Phys. Rev. 97, 494 (1955).

71. Eckstein, W. and Matschke, F.E.P., Phys. Rev. B 14, No. 8, 3231 (1976).

72. Eckstein, W., Molchanov, V.A. and Verbeek, H., Nucl. Instr. Methods (in press).

73. Yavlinskii, Yu. N., Trubnikov, B.A. and Elesin, V.F., Bull. Acad. Sci. USSR Phys. Sou. <u>30</u>, 1996 (1968).

74. Trubnikov, B.A. and Yavlinskii, Yu. N., Soviet Physics JETP <u>25</u>, 1089 (1967).

75. Brandt, W. and Sizmann, R., Phys. Letters <u>37A</u>, 115 (1971).

76. Hagstrum, H.D., Phys. Rev. <u>96</u>, 336 (1954).

77. Erickson, R.L. and Smith, D.P., Phys. Rev. Letters <u>34</u>, No. 6, 297 (1975).

78. Betz, H.D., Rev. Mod. Phys. <u>44</u>, 465 (1972).